CARDIFF UNIVERSITY

The Characterisation of InSb Quantum Well Heterostructures by Electrical Measurement

by

George St J. V. Smith

A thesis submitted in fulfilment for the
degree of Doctor of Philosophy (PhD)

in the
Condensed Matter and Photonics Group
Cardiff School of Physics & Astronomy

February 2019

Declaration of Authorship

I, George Smith, declare that this thesis titled, 'The Characterisation of InSb Quantum Well Heterostructures by Electrical Measurement' and the work presented in it are my own. I confirm that:

- This work has not been submitted in substance for any other degree or award at this or any other university or place of learning, nor is being submitted concurrently in candidature for any degree or other award.

Signed: George Smith

Date: 28/9/18

- This thesis is being submitted in partial fulfillment of the requirements for the degree of Doctor of Philosophy (PhD).

Signed: George Smith

Date: 28/9/18

- This thesis is the result of my own independent work/investigation, except where otherwise stated, and the thesis has not been edited by a third party beyond what is permitted by Cardiff Universitys Policy on the Use of Third Party Editors by Research Degree Students. Other sources are acknowledged by explicit references. The views expressed are my own.

Signed: George Smith

Date: 28/9/18

- I hereby give consent for my thesis, if accepted, to be available online in the Universitys Open Access repository and for inter-library loan, and for the title and summary to be made available to outside organisations.

Signed: George Smith

Date: 28/9/18

- I hereby give consent for my thesis, if accepted, to be available online in the Universitys Open Access repository and for inter-library loans after expiry of a bar on access previously approved by the Academic Standards & Quality Committee.

Signed: George Smith

Date: 28/9/18

“An education was a bit like a communicable sexual disease. It made you unsuitable for a lot of jobs and then you had the urge to pass it on.”

- Terry Pratchett

CARDIFF UNIVERSITY

Abstract

Condensed Matter and Photonics Group
Cardiff School of Physics & Astronomy

Doctor of Philosophy (PhD)

This thesis describes both experimental and theoretical work on the electronic transport properties of 30 nm InSb/AlInSb quantum well 2DEG heterostructures. Advances in the epitaxial growth of large lattice constant III-V materials using mismatched substrates like GaAs or Si has generated renewed interest in developing high mobility devices. Similarly, narrow gap semiconductors are promising candidates for the advancement of spintronic devices taking advantage of their extreme material parameters, such as the small effective mass and large effective Landé g-factor. An investigation of the low temperature Hall effect and Shubnikov-de Haas oscillations of asymmetrically doped InSb quantum well heterostructures has been made to determine the scattering mechanisms present for carriers in the 2D system. Modelling these oscillations by calculation of the density of states at the Fermi energy as a function of magnetic field was performed to analyse the effects of parameter variation on the observed oscillation. Application of a dielectric layer and gate electrode to the material surface has allowed for a carrier density dependent investigation of the transport properties to be performed. These investigations have provided a detailed understanding of the transport limiting scattering mechanisms over a range of carrier densities and temperatures.

A novel study of the current-voltage characteristics of high resistance contacts has been performed to investigate the energetic distribution of electron states in the quantum well under the application of large magnetic fields. Clear Landau level quantisation of the 2D density of states for the first subband of the quantum well has been observed. Analysis of the high field asymmetry of the fundamental Landau level has revealed the presence of significant spin dependent broadening within the heterostructure, which has previously been suggested to exist from an asymmetry of the Fourier transform of Shubnikov-de Haas oscillation.

Dedicated to my Grandmother, whose inexorable faith and support has got me where I am today.

Acknowledgements

This work would not have been possible without the technical, emotional and occasionally physical support from a multitude of people. To comprehensively address each person who deserves my gratitude would require far too much time and space though I shall try to briefly convey my thanks.

Firstly, I wish to thank my supervisor, Dr. Phil Buckle, whose guidance, cheerful enthusiasm and support over the past four years has been invaluable. Though occasionally hard to find, once cornered your willingness to share your knowledge and experience was indispensable. A large portion of this work would not have been possible without the technical assistance of Dr. Steve Clowes, whose valuable discussions helped steer the direction of the work presented here. I would also like to thank Dr. Georgina Klemencic and Dr. Sean Giblin for providing assistance with the dilution refrigeration system. A special mention must be made for Dr. Dan Read who helped me perform dielectric depositions from the other side of the planet.

There have been a number of technical challenges that I have had to overcome during this work. I extend my thanks for the time and effort of the Universities technical staff, in particular I would like to thank Andrew Harrison whose expertise and patience has been particularly useful. Additionally I am grateful to the staff in the cleanroom for providing assistance when called upon. I extend my sincerest gratitude to Dr Craig Allford, our lunchtime discussions have frequently proved enlightening. I would also like to thank other members of the Quantum Devices group, past and present, Dr. Dave Hayes, Chris McIndo, Fadwa Alshaeer and Shawkat Jubair.

Ultimately none of this would have been possible without my Mother, Sister and Grandmother. Their love, support, patience and encouragement throughout my life have moulded me into the man I am today, and this work is in no small part due to you. Archie, whose unconditional love and energy have provided me with distraction and joy over the last three years. I would not be able to acknowledge anybody without giving special attention to the enormous effort provided by my girlfriend Rosie. Your unwavering faith, emotional support, love, and attention has helped me get through the past 4 years. I love you and I thank you.

Finally I would like to acknowledge the Engineering and Physical Research Council (EPSRC) for the studentship which has funded my studies and this work.

Contents

Declaration of Authorship iii

Abstract v

Acknowledgements vii

List of Figures xiii

List of Tables xxi

Abbreviations xxiii

1 Introduction 1
- 1.1 Motivation for using Indium Antimonide in semiconductor research 1
- 1.2 InSb for spintronic applications 3
- 1.3 Outline of this Thesis 4
- 1.4 Publications list 6
- 1.5 Conference Presentations and Posters 7

2 InSb Crystals and Semiconductor Heterostructures 9
- 2.1 Crystal Structure 9
- 2.2 Band Structure of InSb 10
  - 2.2.1 Parabolic band approximation 13
  - 2.2.2 Band non-parabolicity and the Kane model 14
- 2.3 Heterostructures and Band Structure Engineering 17
  - 2.3.1 Heterojunctions 17
  - 2.3.2 Alloying 19
  - 2.3.3 Quantum Wells 20

3 Samples, Fabrication and Measurement 25
- 3.1 Growth of heterostructures 25
  - 3.1.1 Epitaxy 25
  - 3.1.2 Studied Materials 26
- 3.2 Device Fabrication 27
  - 3.2.1 Contact Photolithography 28

- 3.2.2 Hall bar devices . . . 30
  - 3.2.2.1 Ohmic contacts . . . 31
  - 3.2.2.2 Gate contacts . . . 31
- 3.3 Measurement Systems . . . 32
  - 3.3.1 Low field measurement system . . . 32
  - 3.3.2 High field measurement system . . . 33
- 3.4 Magnetotransport Measurements . . . 36
  - 3.4.1 Hall effect measurements . . . 36
  - 3.4.2 Three terminal IV measurements . . . 37
- 3.5 Sample summary . . . 39

4 Magnetotransport measurements on 30nm InSb/AlInSb quantum well heterostructures 41

- 4.1 Classical electron transport . . . 42
  - 4.1.1 Fundamental transport equations . . . 42
  - 4.1.2 The Hall effect . . . 44
  - 4.1.3 Carrier analysis . . . 46
  - 4.1.4 Temperature dependence of the transport properties . . . 48
- 4.2 Electron transport in the high field regime . . . 52
  - 4.2.1 Quantum lifetime extraction . . . 56
    - 4.2.1.1 Thermal dependence of the quantum lifetime . . . 58
    - 4.2.1.2 Carrier density dependence of the quantum lifetime . . . 61
  - 4.2.2 Estimation of the Landau level broadening . . . 63
- 4.3 Summary . . . 66

5 Density of states modelling 69

- 5.1 Introduction . . . 69
- 5.2 Modelling Shubnikov-de Haas oscillations by conductivity . . . 70
  - 5.2.1 Modelling of high field magnetoresistance oscillations . . . 72
- 5.3 The effects of inversion asymmetry on density of states oscillations . . . 79
- 5.4 Comparison between model and measured data . . . 87
- 5.5 Summary . . . 91

6 Three terminal differential conductance measurements 93

- 6.1 Introduction . . . 93
- 6.2 A metal-semiconductor interface on AlInSb . . . 94
  - 6.2.1 Schottky Barriers . . . 94
  - 6.2.2 Surface Pinning . . . 95
  - 6.2.3 Tunnelling current through a surface barrier . . . 97
- 6.3 Differential Conductance Measurements . . . 99
  - 6.3.1 Three terminal measurement . . . 101
- 6.4 Measurements on a high mobility InSb 2DEG . . . 105
- 6.5 Magnetic field evolution of peak width and line shape . . . 111
- 6.6 Evidence for g-factor enhancement . . . 114
- 6.7 Summary . . . 115

7 Conclusions and further work 119

- 7.1 Conclusions . . . 120

7.2 Further work 124

A The 2D density of states **127**

Bibliography **131**

List of Figures

2.1 a) A diagram showing the primitive unit cell of the zincblende structure. b) A schematic of the first Brillouin zone for a zincblende crystal, highlighting points and lines corresponding to real space crystal symmetries. . 11
2.2 Illustration of the simplification of the Bloch function, though the actual wavefunction varies rapidly due to the periodic potential the electron wavefunction can be described sufficiently by a more slowly varying plane wave solution indicated by the dashed line. This envelope function shown is created by the confinement of carriers in a structure such as a quantum well. 12
2.3 The band structure for InSb calculated using density functional theory by Kim, Hummer and Kresse, 2009[28] 13
2.4 Conduction band (red) and light-hole valence band (blue) profiles for first 10% of the FBZ for InSb, calculated using the two-band model (solid line) and four-band model (dotted line). Also plotted is the parabolic band approximation (black dashed lines) of the electron and light hole states to highlight the rapid deviation away from the zone center. 16
2.5 The three types of possible band alignment for a heterojunction. 18
2.6 A comparison of the band alignments for a selection of materials, taken from [31]. The variation in energy of the valence band edge and size of the band gap hint at the variety of heterostructures that can be created. . 18
2.7 The conduction-valence band separation E_g as a function of lattice constant for the common III-V semiconductors and their alloys at room temperature. The small band gap of InSb is accompanied by one of the largest lattice constants of any semiconductor material. 20
2.8 Schematic of the first two solutions for the confined states in both an infinite and a finite square well structure. The wavefunction solutions are drawn to highlight the penetration of the wavefunction into the barrier material in the case of the finite barrier height. 21
2.9 a) A comparison between the 2D density of states using the parabolic approximation and the non-parabolic density of states calculated using the two band model. The non-parabolic density of states rapidly increases lowering the Fermi energy of such materials. b) The effective mass of electrons extracted from the curvature of the conduction band for the 2 and 4-band Kane models. The band edge effective mass of $m^* = 0.013$ is shown to emphasise how significantly non-parabolicity can affect the properties of carriers in the conduction band. 24

3.1 A self-consistent Schrödinger-Poisson solution for the typical layer structure of this material. The δ-dopant plane is heavily doped with Te and consequently contributes significantly to the carrier density of the quantum well. In this instance sufficient charge has been contributed for occupation of the second subband to occur, corresponding to a sheet carrier density of $n_{2D} \approx 3 \times 10^{15}\,\mathrm{m}^{-2}$. The inset is a schematic representation of the layer structure. 27
3.2 The complete processing sequence in the creation of both gated and ungated devices. Ungated devices are created by completion of the processing steps outside of the dashed area. 29
3.3 Scanning electron microscope images of a large ungated Hall bar and small gated Hall bar structure, both structures have a 5:1 ratio of length to width between the voltage probes. The gate is positioned such that the voltage probes measure the potential of the 2DEG underneath the gate. 30
3.4 A simplified schematic of the closed cycle, cryogen free, pulse tube refrigeration system. 33
3.5 Image of the LS-250 dilution refrigerator interior, the impressively low temperatures are achieved by sequential staging of pulse tube and dilution refrigeration technology. The polished Au coating on the low temperature stages is to minimise thermal emissivity and limit absorption of any incident thermal radiation. 35
3.6 A typical schematic for a gated magnetoresistance measurement. The differential inputs V_{xx} and V_{xy} represent the longitudinal and Hall voltages respectively. Non-gated structures are measured in the same manner excluding the gate connection. 37
3.7 (a) A schematic of the three terminal I(V) measurement set-up and (b) its equivalent circuit. The common contact for the voltage measurement and the current drain was chosen to be the most resistive contact on the device to maximise the voltage drop across the contact. 38

4.1 A schematic representation of the forces present on charges moving through a magnetic field to produce the Hall effect. 45
4.2 Carrier mobility against sheet carrier density extracted from single carrier fitting for all InSb/AlInSb quantum well samples. The dashed lines are a guide to the eye to highlight the fall off in mobility at low and high carrier densities. The red data are ungated samples while green and blue were fabricated with a CrAu gate electrode on top of amorphous MgO and Si_3N_4 dielectrics respectively. Square or triangular markers indicate structures made using the same material. 47
4.3 A comparison between single and two carrier fitting to magnetoresistance data at 130 K for sample SF1054. The single carrier model is most valid when the cyclotron radius (ℓ_c) is larger than the mean free path (ℓ). The single carrier model extracts a carrier density and mobility of $3.9 \times 10^{15}\,\mathrm{m}^{-2}$ and $22.7\,\mathrm{m}^2\mathrm{V}^{-1}\mathrm{s}^{-1}$ respectively, while the two carrier model extracts a high mobility carrier with density $3.5 \times 10^{15}\,\mathrm{m}^{-2}$ and mobility $25.0\,\mathrm{m}^2\mathrm{V}^{-1}\mathrm{s}^{-1}$. 49
4.4 The carrier mobility and sheet carrier density extracted from single carrier fitting as a function of temperature. The reduction in carrier density is consistent with the freeze out of intrinsic carriers at low temperature. . . 52

4.5 The Shubnikov-de Haas (red) and IQH (blue) effects measured at 12 mK for sample SF0968. 54

4.6 A Gaussian broadened Landau level model of the evolution of the 2D density of states for a single subband in InSb with increasing magnetic field. The 2D oscillations become significant when $\Gamma \leq \hbar\omega$. Spin split oscillations can be observed when the Zeeman contribution is larger than the broadening. 55

4.7 Typical low field resistivity trace of sample SF1055. The obvious Shubnikov-de Haas oscillations at 3 K are noticeably diminshed by 7 K. 57

4.8 Thermal damping factor χ_T for InSb (solid) and GaAs (dashed) at 1 K (blue) and 5 K (red) calculated using the band edge effective masses of 0.014 m* and 0.043 m* respectively. Clearly the damping factor for InSb at 5 K is similar to that of GaAs at 1 K highlighting why the quantum lifetime in InSb can be discerned at higher temperatures. 57

4.9 The thermal damping term as a function of temperature for ungated sample SF1055. The data are extracted from a field value of $B = 0.75$ T, the dashed line is fit using a least squares minimisation. 58

4.10 Dingle plot for sample SF1055 at various temperatures. The dashed lines are linear fits forced to an intercept of 1 to highlight the data quality. Elevated temperatures have been offset by integer values for clarity. . . . 59

4.11 The extracted quantum lifetime and corresponding quantum mobility as a function of temperature for sample SF1055. The dashed line is a guide showing the mean value while the cross-hatched region highlights a standard deviation around the mean. 60

4.12 The extracted quantum lifetime and corresponding quantum mobility as a function of carrier density for samples SF1055 (triangles) & SF1056 (squares) at $3\,K$. The dashed fit line is a guide to indicate the upward trend in the data. Hollow markers indicate data taken from gated samples over a range of carrier densities while solid markers are measurements of ungated devices. The red dotted line is the predicted quantum lifetime from a relaxation time approximation model including the effects of remote ionised impurities, background impurities and non-parabolicity. . . . 62

4.13 The transport and quantum lifetime ratio dependence on carrier density. The ungated samples (solid markers) have a distinctly higher ratio than the gated sample (hollow markers). The dotted line is the lifetime ratio predicted from the transport model with a single impurity with a density of $n_{2D} = 1 \times 10^{16}\, m^{-2}$ in the δ-plane. The dashed line shows the predicted lifetime ratio when a 2^{nd} plane of charged impurities with a density of $\sim 10^{17}\,\mathrm{m}^{-2}$ is included at the samples surface. 64

4.14 The low field longitudinal resistance of ungated sample SF1055 and the corresponding second differential. The onset of Shubnikov-de Haas oscillation are highlighted, this correspond to the point were oscillations are no longer periodic in $1/B$. The second differential highlights shows an apparent beat pattern with a non-zero beat amplitude, this phenomenon will be addressed in chapter 5. 65

4.15 The broadening parameter Γ as a function of carrier density determined from the onset of SdH oscillations and calculated from the quantum lifetime. 66

5.1 Magnetic field evolution of the Fermi energy (red) and DOS at the Fermi energy (black) for both Lorentzian (solid) and Gaussian (dashed) broadened lineshapes, the lower plot is zoomed in at lower fields. The energies of the first ten spin split Landau levels are plotted to highlight that a peak in the DOS occurs when a Landau level crosses the Fermi energy. A carrier density of $n_{2D} = 2.5 \times 10^{15}\,\mathrm{m}^{-2}$, effective mass $m^* = 0.013m_0$, a LL broadening of $\Gamma = 2.5\,\mathrm{meV}$ and effective g-factor $g^* = 30$ were used in the calculation. 74

5.2 Comparison between both Lorentzian and Gaussian broadening types in both the parabolic (black) and non-parabolic (red) approximations for the Landau level energies. (Top) The DOS at the Fermi energy (Bottom) as a function of field. A carrier density of $n_{2D} = 2.5 \times 10^{15}\,\mathrm{m}^{-2}$, effective g-factor of $g^* = 30$ and broadening of $\Gamma = 2.5\,\mathrm{meV}$ were used in the simulation. 75

5.3 (Bottom) A calculation of the DOS at the Fermi energy as a function of magnetic field at different carrier densities. The periodicity of the DOS oscillations are highly carrier density dependent as shown by the Fourier transform plot above. (Top) The corresponding Fourier transform of each oscillation, the amplitude of the FT peak typically increases with carrier density due to a greater number of oscillations being sampled within a given field region. 76

5.4 Investigation of the effects of variation in broadening parameter Γ as a function of magnetic field. Smaller broadening results in larger DOS oscillations and spin split peaks being resolved at lower magnetic fields. The broadening has no obvious effect on the FT peak position, though clearly affects the amplitude. 77

5.5 (Bottom) A plot comparing the effects of different g-factors on the observed DOS at the Fermi energy. (Middle) A plot of the peak number against peak field for the calculated DOS (triangles), compared to actual data (squares) from sample SF0968 with similar carrier density. The field at which the gradient turnover occurs is dependent upon the g-factor of the material and the broadening of the Landau levels. (Top) The calculated FT of the different oscillations. 78

5.6 The 1D parabolic dispersion relation for electrons in the conduction band including the effects of the Rashba interaction. The inset shows the linear energy separation of the two spin states for the parabolic approximation. A Rashba parameter of $\alpha = 2\,\mathrm{eV\AA}$was used for the calculation. 82

5.7 The spin splitting due to the Rashba interaction of the first two Landau levels as a function of magnetic field. At very low fields the energies are highly non-linear and degenerate at $B = 0\,\mathrm{T}$. The vertical dashed line shows the point of a Landau level crossing, a distinct feature of zero-field spin splitting. 84

5.8 Investigation of the effects of variation of the Rashba coupling strength α as a function of magnetic field. The frequency of the beat oscillations is determined by the magnitude of the spin-orbit coupling parameter. An large Rashba parameter is associated with significant separation between the peak frequencies in the Fourier transform. 86

5.9 A comparison between the density of states at the Fermi energy created by Landau levels with both equivalent and unequal broadening. While peak positions remain unchanged the peaks corresponding to the spin state with larger broadening have a smaller amplitude. The presence of unequal broadening also causes the oscillation amplitude at a beat node to increase significantly. A carrier density of $n_{2D} = 6.0 \times 10^{15}\,\mathrm{m}^{-2}$ was used in the simulation to increase the number of oscillations between nodes to emphasise the non-zero amplitude. 88

5.10 The measured Shubnikov-de Haas oscillations for ungated sample SF0968. Though no beating effects are obvious from the raw data, inspection of the second differential shows a clear beat node. The Fourier transform of the second differential is shown and the spin split nodes are highlighted. . 89

5.11 The extracted spin splitting from Fourier transform data for samples SF0963, SF0968, SF1056 and SF1055. The samples SF0963, SF0968, SF1056 intentionally have significantly lower doping than sample SF1055. The dashed line shows the expected strength of spin splitting predicted by equation 5.10 using the parameter for α_0 quoted in [93]. The strength of the electric field in the heterostructure was determined by Schrödinger-Poisson modelling. 90

5.12 A comparison between the second differential of the resistivity data for SF0968 (black) and the predicted oscillation in the density of states using both the parabolic (blue) and non-parabolic (red) simulations. The value for α used in the simulation was $0.124\,\mathrm{eV\AA}$ with a carrier density of $2.39 \times 10^{15}\,\mathrm{m}^{-2}$. The density of states oscillations have been offset to improve the clarity of the comparison. 91

6.1 A schematic of the band structure of a heavily doped semiconductor with a Schottky barrier at the surface. The different transport mechanisms, (a) Thermionic emission of carriers over the top of the barrier, (b) Thermionic field emission of carriers above the Fermi energy tunnelling through the barrier, and (c) Field emission, carriers at the Fermi energy tunnelling through the barrier. 96

6.2 A schematic showing the density of states at the surface of a heavily doped semiconductor and the associated band structure created due to the pinning of the Fermi energy to the mid-gap states at the surface. . . . 97

6.3 A schematic of the intersection between the 2D Fermi circle and 3D Fermi sphere. A carrier can only tunnel from a 3D to a 2D system by satisfying the conservation of momentum represented by the ring at the edge of intersection between the Fermi surfaces between the two systems. 99

6.4 The excitation voltage applied to the device to measure the differential conductance as a function of DC bias. The differential conductance is extracted by software lock-in techniques of the AC signal. 100

6.5 (a) A schematic of a typical three terminal I(V) measurement and (b) the three terminal circuit used during these measurements. Typical measurements exclude measuring the voltage drop across the 2DEG such that the only contribution to the voltage drop is from the contact resistance. The circuit configuration in these experiments necessarily measures the voltage drop across the 2DEG and the contact. As such the common contact for the voltage measurement and the current drain was chosen to be the most resistive contact on the device to maximise the voltage drop across the contact. 102

6.6 The Schrödinger-Poisson solution for the heterostructures studied in this thesis. Considering the δ-dopant as a 2 nm thick plane located 25 nm from the edge of the quantum well, a dopant density of $1.98 \times 10^{24}\mathrm{m}^{-3}$ is required for a state in the dopant plane to exist below the Fermi energy. Corresponding to a quantum well carrier density of $n_{2D} \simeq 4.2 \times 10^{15}\mathrm{m}^{-2}$. A low density n-type background of $4.0 \times 10^{20}\mathrm{m}^{-3}$ was used in the calculation. 104

6.7 A 3D schematic of a likely transport mechanism. (Left) The equilibrium condition under zero bias. (Right) When bias is applied to the structure the quasi-Fermi energy of the 2DEG increases, the number of electrons in the quantum well with an energy greater than the Fermi energy of the metal is proportional to the applied bias. 104

6.8 A 2D schematic of the band structure of the system at a finite magnetic field and the corresponding differential conductance. Left to right images show the effects of increasing the linear bias across the device. When the Fermi energy of the metal is coincident with a Landau level in the quantum well a peak in the differential conductance is observed due to the large variation in current over a small bias region. 105

6.9 The 4 K I-V characteristic and differential conductance data for sample SF1055 at multiple fields. Under reverse bias the low field I-V shows an almost constant gradient before a plateau at high bias. The data at higher fields shows more complicated structure. Turning points in the I-V curve manifest as peaks in the differential conductance. 107

6.10 (Top) The amplitude of the differential conductance peak from the $n = 0$ Landau level as a function of magnetic field. (Bottom) Normalisation of the differential conductance data to the area underneath the curve yields two distinct linear regions. 108

6.11 (a) A 2D plot of the differential conductance measured across a high resistance contact as a function of bias measured across the contact and magnetic field. In region 2 high intensity regions evolve in very good agreement with the predicted evolution of a Landau fan calculated using the band edge effective mass of InSb, while in region 1 the high intensity peaks show significant deviation from the prediction. (b) Scaling the data in region 1 by a constant value of $0.7V_{DC}$ brings the high intensity regions back into good agreement with the energies predicted by the Landau fan. This data predicts the Fermi energy of the quantum well underneath the contact to be ~ 100 meV above the subband energy at zero field. 110

6.12 An example of the quality of fit achieved by fitting a two Lorentzian model to the 4 K differential conductance data on sample SF1055 at 5 T. Good agreement between the fit and the data is achieved here with Lorentzian widths $\Gamma_+ = 4 \pm 1$ meV and $\Gamma_- = 10 \pm 1$ meV. 112

6.13 A comparison between the quality of fit extracted using Gaussian or Lorentzian broadening profiles for data at 7.23 T. Though both profiles reasonably approximate the trend of the differential conductance peak, the off-peak fit of the Lorentzian broadening is clearly superior to that of the Gaussian profile. 113

6.14 The broadening parameters for the high and low energy spin states Γ_+ and Γ_- extracted from a double Lorentzian fitting to 4 K data for sample SF1055. Two distinct broadening parameters are extracted from the data. The black dashed lines are $\eta\sqrt{B}$ fits to the data. The broadening of the low energy spin state shows strong agreement with the fit. 114

6.15 Values for the magnitude of the effective g-factor estimated from the separation between two Lorentzian peaks fit to the 4 K differential conductance data for sample SF1055. At high field a distinct increase in the separation is observed, suggesting an increase in $|g^*|$. 116

A.1 A schematic representation of the array of allowed states in k-space. A given k-vector describes a circle enclosing a particular number of states. . 128

List of Tables

1.1 Fundamental material properties of popular semiconductor materials. The direct band-gap E_g, electron effective mass m*, static dielectric contact ϵ_R and electron g-factor at T = 300 K are shown for bulk Si, Ge, GaAs, InAs and InSb. Data was taken from [13–16]. 3

2.1 Comparison between the effective masses of the electron and hole states in common III-V semiconductors. In most systems the electron and light hole effective masses are similar though the heavy holes are far more massive. All values are in units of electron mass. 14

3.1 A Table summarising the nominal high and low temperature classical transport properties for some of the heterostructures studied in this thesis. The values quoted for the gated samples were calculated from data measured with the gate electrode connected to ground. 39

4.1 Summary table of the classical and quantum transport properties for two samples investigated. The range of lifetimes reveal an almost constant ratio between transport lifetimes. 63

5.1 The default parameters used for modelling the DOS at the Fermi energy. 72

Abbreviations

FBZ	**F**irst **B**rillouin **Z**one
LL	**L**andau **L**evel
DOS	**D**ensity **O**f **S**tates
E_F	**F**ermi **E**nergy
QW	**Q**uantum **W**ell
2DEG	2 **D**imensional **E**lectron **G**as
CMOS	**C**omplementary **M**etal **O**xide **S**emiconductor
I(V)	**C**urrent **V**oltage
MBE	**M**olecular **B**eam **E**pitaxy
SEM	**S**canning **E**lectron **M**icroscopy
TEM	**T**unnelling **E**lectron **M**icroscopy
SP	**S**chrödinger **P**oisson
NP	**N**on-**P**arabolicity

Chapter 1

Introduction

1.1 Motivation for using Indium Antimonide in semiconductor research

In 1947 Physicists Shockley, Bardeen, and Brattain at Bell labs first demonstrated an observable power gain in a semiconductor point contact transistor using a slab of Germanium (Ge) with gold contacts to amplify electrical signals from a microphone [1]. Though first demonstrated using Germanium, Silicon quickly became the material of choice for commercialisation of these properties as its native oxide made for simple application of low leakage-current gate electrodes. This layed the foundation for complementary metal-oxide semiconductor (CMOS) technology which is the basis for low power consumption digital logic, eventually resulting in the Si integrated circuit revolution which underpins the modern communications age.

Gordon Moore noticed a trend in the 1960's that the size of Si transistor devices halved approximately every 18 months[2]. This drive for component miniaturisation is as a result of the desire to increase the processing abilities of modern computers. The beginning of the 21$^{\mathrm{st}}$ century gave commercial sub-100 nm transistor gate lengths with 5 nm gate technology predicted to be on the market by 2020, pushing Moore's Law to the limit of what may be physically possible for standard transistor architectures and fabrication techniques. At these scales quantum transport phenomena significantly degrade the performance of established technology. Thermal power dissipation and gate leakage due to quantum tunnelling, which were insignificant processes in larger structures with thicker oxides, are now limiting factors requiring novel physics and engineering to meet the demand for ever increasing processing power.

Novel physics and device engineering technologies have long been used as tools to compensate for the slowing down of Moore's law, mainly due to decreasing node size and increasing architecture complexity. The low dimensionality of current architectures has encouraged research into the prospect of single atom transistors and their incorporation into existing Si technologies [3]. The incorporation of III-V semiconductors into existing high-volume, low-cost Si manufacturing technologies is also an area of vigorous research. Advances in epitaxy technologies have allowed the growth of III-V materials directly on Si and the creation of high frequency electronics, which take advantage of the high mobility conducting channels which can be created in III-V materials like GaAs and InGaAs [4, 5]. The small effective mass of carriers exhibited by III-V materials at room temperature gives significant improvements over Si where the high mobilities allow for low power consumption devices to be realised. Integrating these materials onto Si has significant challenges. Lattice mismatch makes the growth of low defect density structures a challenge and the lack of a native oxide for III-V materials makes for more complex processing.

A comparison between fundamental properties for some of the III-V compound materials and intrinsic semiconductors Si and Ge is shown in table 1.1. InSb has the smallest effective mass of all of the III-V semiconductor materials, consequently it has the largest room temperature mobility of all of the bulk semiconductors making it extremely attractive for high frequency technologies such as high electron mobility transistors (HEMTs) [6]. In spite of the high temperature transport qualities of bulk InSb, traditionally material research and development has favoured GaAs especially in the field of heterostructure devices. This is due to it being almost perfectly lattice matched to the AlGaAs alloys, easing the development of low defect density heterostructures. Indeed throughout the 1980's the state of the art low temperature electron mobility for modulation doped GaAs/AlGaAs heterostructures increased by three orders of magnitude, a rate of development that has not since been matched for any other material system.

The large lattice constant of InSb has posed a significant engineering challenge for further material development using low cost existing processing techniques. Growth of InSb crystals on existing Si or GaAs wafers introduces significant strain into the crystal,

TABLE 1.1: Fundamental material properties of popular semiconductor materials. The direct band-gap E_g, electron effective mass m*, static dielectric contact ϵ_R and electron g-factor at T = 300 K are shown for bulk Si, Ge, GaAs, InAs and InSb. Data was taken from [13–16].

	$E_g(\Gamma)$ (eV)	m* (m_0)	ϵ_R (ϵ_0)	g*
Si	3.21	0.190	11.9	1.9
Ge	0.80	0.081	16.2	1.6
GaAs	1.42	0.064	12.9	-0.4
InAs	0.35	0.023	15.2	-15.6
InSb	0.18	0.014	16.8	-50.6

and the inevitable large dislocation densities adversely impacting the mobility of the material. Significant effort is being made to decrease the defect densities of large lattice constant III-V materials on cheaper lattice mismatched wafers. The incorporation of complex supperlattice structures, stepped buffer layers and dislocation filtering are being used to improve material mobility while minimising the depth of the buffer layer which minimises the complexity of processing, driving drown cost [7–12]. These technological improvements are making InSb an economical choice for the exploitation of high mobility dependent devices, such as high sensitivity magnetic field sensors and high frequency electronics, while using standard Si or GaAs production techniques.

1.2 InSb for spintronic applications

The potential for the exploitation of the spin degree of freedom for information transfer has been an area of investigation since the 1970's when Tedrow and Meservey observed a spin dependent tunnelling current into a magnetic contact [17]. Studies of multi-layered magnetic materials gave rise to the discovery of giant magnetoresistance in 1988 by Grünberg and Fert independently [18]. This phenomenon is now used extensively for magnetic field sensing such as in hard disk drives, which has helped drive the increasing storage densities over the past few decades. Exploitation of the spin of an electron instead of traditional charge transfer electronics has been suggested to hold the key for lower power consumption computational hardware with similar performance [19].

Semiconductor spintronics has many potential advantages over metallic spin devices. The large spin lifetimes and long spin coherence lengths [20] results in the possibility of larger structures or the ability to perform more operations on a particle while maintaining coherence. The ability to engineer the bandstructure of semiconductors gives exceptional control of the energetic separation between the spin states within the heterostructure. Exploitation of the Rashba effect (discussed in chapter 4) in two dimensional electron gasses (2DEGs) has been demonstrated to give control of the energetic separation of spin states by the application of a gate bias to the surface of a heterostructure [21]. This emphasises the possibility of controlling an electron's spin electrically in lieu of the usual approach of using external magnetic fields.

The large spin orbit interaction of narrow gap semiconductors, in conjunction with the increasing incorporation of III-V materials into traditional Si based architectures, highlights the possibility that the future of computing technologies may be a union between traditional low cost charge based devices with high frequency spin based devices based on III-Vs. The large g-factors of InSb and InAs make them attractive materials for research into spin based devices due to the low energies required for observation of spin dependent phenomena. The ability to generate and observe a spin polarised current in semiconductors is of fundamental importance to the development of semiconductor spintronics. The use of in-plane gates to generate a polarised spin current via the Rashba interaction has similarly been reported for InGaAs [22] and InSb [23] based heterostructures. The extreme material properties of InSb make it a promising candidate for the creation of an entirely self contained spin device, theoretically being able to be used to generate a spin polarised current, manipulate those spins and, selectively read out the particle spin states simply through electrical manipulation.

1.3 Outline of this Thesis

The work presented in this thesis was undertaken as part of the EPSRC funded project "*Spin manipulation in narrow band semiconductors*". This work was performed at Cardiff University, with the intention to study the transport properties of InSb quantum well two-dimensional electron gasses grown at the EPSRC National Epitaxy Facility, III-V growth facilities at Sheffield University. The structure of the thesis is organised as follows.

Chapter 2 introduces the relevant physical concepts behind the classification of semiconductors, the notion of an electronic band structure and valuable approximations which allow for the estimation of band parameters such as the electron effective mass and Fermi energy to be calculated. Due to the narrow band gap of InSb particular emphasis is placed on the incorporation of the effects of non-parabolicity and how they affect the extracted values when compared to a parabolic model. A brief summary of the concepts behind the creation of semiconductor heterostructures and their use in creating quantum wells for electron confinement and two-dimensional transport is made.

Chapter 3 addresses the growth of such heterostructures using MBE technology and the subsequent processing steps which occur to create devices which have the desired geometry to be mounted and measured. The measurement facilities used to characterise the devices are discussed and the equipment involved in creating low temperature environments. The hardware used to perform these measurements is introduced along with the wiring schematic required to perform the measurements. Lastly, a summary of all the heterostructures studied in this thesis is given.

Chapter 4 introduces the first group of results obtained by investigation of the low temperature magnetoresistance of InSb Hall bars. The chapter begins with the introduction of relevant physics behind transport behaviour in the presence of electric and magnetic fields and how these measurements may be used to extract information about the properties of the system being measured. Analysis of the magnetoresistance behaviour for a number of different heterostructures is made and, by modelling such behaviour, estimates for the carrier density and carrier mobilities in both gated and ungated Hall bar devices are presented. Observation of the temperature dependence is then compared with scattering models to identify dominant scattering mechanisms over a range of temperatures. The examination of oscillations in the magnetoresistance of such structures is used to extract information about the quantum lifetime of particles and compared with the predictions of a transport model [24]. The ratios between the classical and quantum transport lifetimes are presented over a range of carrier densities to determine the likely limiting scattering mechanism within these structures. The chapter is concluded by a determination of the lifetime broadening of carriers.

Chapter 5 details how estimating the density of states as a series of Lorentzian or Gaussian broadened distributions may be used to model the magnetoresistance oscillations shown in the previous chapter. The effects of variation of model parameters such as the carrier density, single particle broadening and electron g-factor are explicitly shown and where appropriate compared with measured data. A comparison of the incorporation of non-parabolic effects is made when calculating the distribution in the density of states and its effect on the modelled oscillation in the density of states. Zero-field spin splitting due to the inclusion of the Rashba effect into the model is introduced and the consequent emergence of a beat pattern in the oscillation is discussed. The concept of spin dependent broadening is introduced and the effects that such broadening has on the oscillating density of states are modelled. The chapter concludes with a comparison between the modelled density of states and the magnetoresistance oscillations of a typical InSb heterostructure in an effort to determine the magnitude of the Rashba interaction strength.

Chapter 6 presents measurements made across a high resistance contact to reveal the energetic distribution of states within the quantum well beneath the contact. The deposition of certain metals onto semiconductor surfaces is known to create Schottky contacts with asymmetric current-voltage characteristics due to the significant effect the metal has on the band structure of the material. The vertical transport of electrons through such a barrier is discussed and techniques for the measurement of the density of states is briefly covered. Differential conductance measurements of a high resistance Schottky contact are presented and the energetic distribution of states is examined. The chapter concludes with a discussion of how the data is fit with a model using state distributions and parameters estimated from previous chapters, values for the electron g-factor and the particle lifetimes are subsequently extracted.

Chapter 7 concludes the work presented in this thesis, summarising the results obtained in each chapter. A potential program of further work is presented with regard to each chapter.

1.4 Publications list

[1] Smith. G, Simmons. R, Hayes. D, Allford. C, Clarke. E, Zhang. S, Clowes. S, Buckle. P. “Explanation of apparent g-factor oscillation in Shubnikov de Haas measurement of III-V semiconductors”. In preparation (2018)

[2] Smith. G, Clowes. S, Clarke. E, Zhang. S, Buckle. P. “Landau level spectroscopy of an InSb quantum well underneath a high resistance contact”. In preparation (2018)

1.5 Conference Presentations and Posters

[1] Smith. G, Hayes. D, Allford. C, Clarke. E, Zhang. S, Buckle. P. “An apparent large oscillation of effective g-factor in an InSb quantum well 2DEG”. - Poster - EP2DS Penn State University, PA, USA. (2017)

[2] Smith. G, Clowes. S, Simmons. R, Clarke. E, Zhang. S, Buckle. P. “Electrical characterisation of InSb quantum well 2DEGs at low temperature”. - Invited talk - Cooling electrons below 1mK for novel physics workshop, Quantum Optics, Quantum Information and Quantum Control Group, Institute of Physics, Cardiff University. (2018)

Chapter 2

InSb Crystals and Semiconductor Heterostructures

2.1 Crystal Structure

Neglecting the III-Nitrides, the majority of III-V binaries crystallise into a zincblende structure comprised of two interpenetrating face-centered cubic (fcc) lattices each populated with atoms of a single group. InSb is no exception, each atom has four nearest neighbours arranged tetrahedrally around the lattice point and bonds covalently with atoms from the opposite group. Repeated translation of the unit cell of InSb (figure 2.1(a) by a lattice constant along each of the primitive lattice vectors constructs a crystal of increasing size with the fundamental periodicity of the unit cell.

Though the crystal is physically defined in real space it is informative to construct the *reciprocal lattice* and consider the crystal structure in momentum (k) space due to the wave-like properties of carriers in the crystal. Analogous to the unit cell of the real lattice; the reciprocal lattice has a unit cell known as the *first Brillouin zone* (FBZ), which contains all reciprocal lattice vectors closer to one reciprocal lattice point than to any other. It is possible to show that any k-vector that lies outside the FBZ at a specific reciprocal lattice point can be transformed by a reciprocal lattice vector such that it lies within the FBZ around another reciprocal lattice point. Using this formalism it is sufficient to describe the entirety of the crystal structure by merely considering the FBZ. This allows for the complete description of a crystal lattice in an idealised form, though any physically realised crystal differs from this simplification considerably due to the presence of defects in the crystal lattice, presence of localised strain and presence of boundaries to the single crystal size. The FBZ for a zincblende crystal takes the form of a truncated octahedron as shown in figure 2.1(b).

2.2 Band Structure of InSb

When considering fundamental electronic properties of materials it is necessary to have an understanding of the distribution of electronic states within the system. This dictates where electrons are likely to be within a structure, the kinetic energy they possess, and how massive they might appear. As such it is informative to discuss the physics behind the distribution of electronic states in InSb and how significantly they differ from other more common III-V compounds such as GaAs.

An electron considered in isolation may be described by a plane wave whose wavefunction has the form $\psi(\boldsymbol{r}) = e^{\boldsymbol{ik\cdot r}}$, this wavefunction satisfies the real-space time-independent Schrödinger equation,

$$\left[\frac{-\hbar^2}{2m_e}\nabla^2\right]\psi(\boldsymbol{r}) = E\psi(\boldsymbol{r}) \tag{2.1}$$

where $\hbar$ is the reduced Planck constant, m_e is the mass of the electron, ∇ is the differential operator, and E is the electron energy. This produces the familiar form for the energy of an electron $E = \hbar^2k^2/2m_e$ and is known as the *free-electron model.*

In contrast to the free-electron model, where electron energies are considered in an infinite, unchanging background potential; electrons in a crystal do not exist in such an ideal system and experience potential energy variations which oscillate with the periodicity of the crystal due to the presence of ionic nuclei as represented in figure 2.2. The full real-space Schrödinger equation includes a term to take account of the effect of any perturbing potentials ($V(\boldsymbol{r})$) to the free electron system such as the background potential or carrier-carrier interactions,

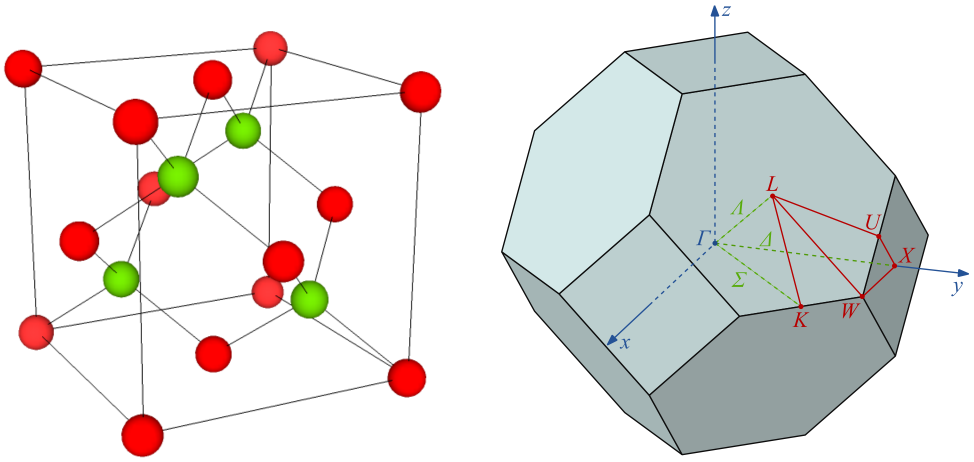

(a) (b)

FIGURE 2.1: a) A diagram showing the primitive unit cell of the zincblende structure. b) A schematic of the first Brillouin zone for a zincblende crystal, highlighting points and lines corresponding to real space crystal symmetries.

$$\left[\frac{-\hbar^2}{2m_e}\nabla^2 + V(\boldsymbol{r})\right]\psi(\boldsymbol{r}) = E\psi(\boldsymbol{r}). \tag{2.2}$$

Though at first glance this appears to present a headache for solving the Schrödinger equation to describe the quantum mechanical properties of electrons in a crystal, the problem can be simplified with the introduction of the *Bloch theorem*. Bloch showed that eigenfunctions of the Schrödinger equation for a periodic potential system are the product of a plane wave component and a function that has the same periodicity as the periodic potential, having the mathematical form

$$\psi_{\boldsymbol{k}}(\boldsymbol{r}) = u_{\boldsymbol{k}}(\boldsymbol{r})\exp\left(\boldsymbol{i}\boldsymbol{k}\cdot\boldsymbol{r}\right) \tag{2.3}$$

where ψ is the electron wavefunction, $\boldsymbol{r}$ is the spatial coordinate of the electron and $\boldsymbol{k}$ its wave vector. This elegant expression means that an electron's motion within a periodic potential can be described as if it were a free electron whose motion is described as a plane wave but modified due to the presence of the periodic potential, known as the *nearly free-electron model*. An important consequence of the Bloch equation is that there exist regions of energy with an absence of electron states corresponding to certain

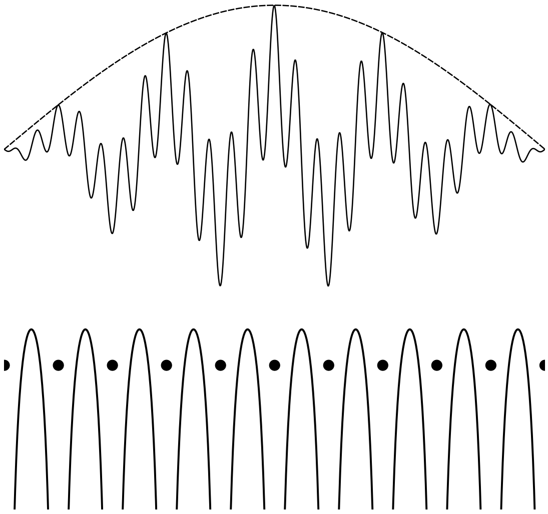

Figure 2.2: Illustration of the simplification of the Bloch function, though the actual wavefunction varies rapidly due to the periodic potential the electron wavefunction can be described sufficiently by a more slowly varying plane wave solution indicated by the dashed line. This envelope function shown is created by the confinement of carriers in a structure such as a quantum well.

wave vectors which are coincident with the boundaries of each BZ. The energy states which exist between these forbidden regions are classified as *energy bands* since they form bands of states which are available for electron occupation. Justification for these forbidden regions is treated exhaustively throughout the literature [25–27] and may be attributed to Bragg reflections at the zone boundaries.

Once the spatial variation and symmetries of the crystal are taken into account the band structure of the crystal becomes quite complex far away from the zone centre. Figure 2.3 shows the bandstructure of InSb, band structure calculations may be performed using ab initio methods such as density functional theory or from more empirical methods, which require fitting parameters such as the $\boldsymbol{k.p}$ method. Close to the zone centre the conduction and valence bands are quite symmetric and, to a first approximation, may be described by a parabolic potential model. Though for semiconductors with narrower band gaps the k-vector to which the parabolic approximation is valid reduces considerably.

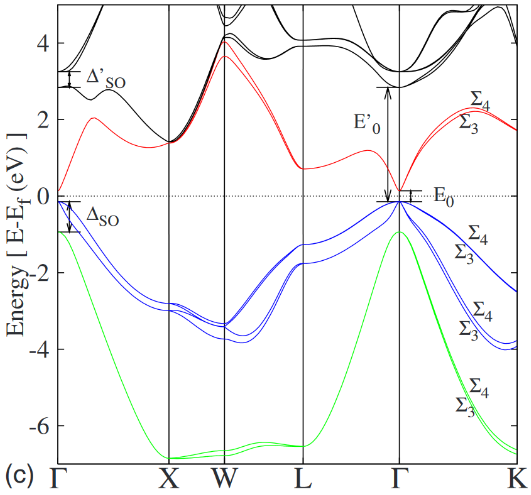

FIGURE 2.3: The band structure for InSb calculated using density functional theory by Kim, Hummer and Kresse, 2009[28]

2.2.1 Parabolic band approximation

In contrast to the free-electron model, carriers in a crystal have energy described by an *effective mass* instead of the mass of the bare electron, which arises due to electron interactions with the crystal. Thus the energy of an electron in the conduction band will have an energy described by,

$$E_c(\boldsymbol{k}) = E_g + \frac{\hbar^2 \boldsymbol{k}^2}{2m^*_{cb}} \tag{2.4}$$

where E_g is the band gap energy and m^*_{cb} is the effective mass of carriers that occupy the conduction band. The effective masses of carriers in the valence and conduction bands are typically very different. Carriers in the conduction band can be thought of as being delocalised from any particular atom, whereas valence band conduction occurs through electrons “hopping” between empty states around atoms, the more common perspective is to consider the empty states (referred to as *holes*) traversing through the crystal. A comparison between the conduction band and valence band effective masses for a few common semiconductor materials is given in table 2.1.

Material	m^*_{cb}	m^*_{lh}	m^*_{hh}
GaAs	0.067	0.082	0.51
GaSb	0.041	0.050	0.40
InAs	0.023	0.026	0.41
InSb	0.014	0.015	0.43

Table 2.1: Comparison between the effective masses of the electron and hole states in common III-V semiconductors. In most systems the electron and light hole effective masses are similar though the heavy holes are far more massive. All values are in units of electron mass.

The effective mass of the band is described by the amount of curvature the band has at a finite wave vector and is given by,

$$\frac{1}{m^*} = \frac{1}{\hbar^2}\left(\frac{d^2E}{dk^2}\right). \tag{2.5}$$

In the case of the parabolic approximation this curvature is constant regardless of wave vector resulting in an energy independent effective mass. At small wave vectors, this approximation describes the energy and mass of particles well; however, in the real world at increasing $\boldsymbol{k}$ the approximation deviates further from reality and the effects of any non-parabolicity must be considered.

2.2.2 Band non-parabolicity and the Kane model

The influence of band non-parabolicity in narrow-gap semiconductors can be estimated through the inclusion of band mixing between valence and conduction band states. This representation was first used by Kane [29] in a matrix formalisation and has been shown to accurately describe the conduction band profiles of narrow-gap materials. The interaction between the $\Gamma_{6c} - \Gamma_{7v}$ (conduction - spin split-off bands) and $\Gamma_{6c} - \Gamma_{8v}$ (conduction - valence bands) contribute most significantly to the non-parabolicity of a system. The effects of more remote bands must be taken into account for wider gap semiconductors (such as GaAs) to give an accurate approximation to the extent of non-parabolicity due to the less significant perturbation from the more remote states.

The Kane model has been extremely well studied and is most intuitively represented in its four-band form, which allows coupling between the conduction band and the three nearest valence band states but neglects the effects of spin on the system. The four-band

Kane Hamiltonian matrix can be presented as,

$$H(\boldsymbol{k}) = \begin{bmatrix} E_g + \epsilon(\boldsymbol{k}) & i\frac{\hbar P}{m_0}k_x & i\frac{\hbar P}{m_0}k_y & i\frac{\hbar P}{m_0}k_z \\ -i\frac{\hbar P}{m_0}k_x & \Delta - \epsilon(\boldsymbol{k}) & 0 & 0 \\ -i\frac{\hbar P}{m_0}k_y & 0 & -\epsilon(\boldsymbol{k}) & 0 \\ -i\frac{\hbar P}{m_0}k_z & 0 & 0 & -\epsilon(\boldsymbol{k}) \end{bmatrix} \tag{2.6}$$

where E_g is the band gap, Δ the spin split-off energy, $\epsilon(\boldsymbol{k})$ is the free particle energy $\frac{\hbar^2\boldsymbol{k}^2}{2m_0}$, $k_{x,y,z}$ represent the wavevector in the three Cartesian coordinates, and P is the Kane interband momentum matrix element and is approximately constant for all materials [15]. Since a 2D system only has the two degrees of freedom, we can alter the form to ignore the momentum (energy) outside of the 2D plane.

$$H_{2\mathrm{D}}(\boldsymbol{k}_\perp) = \begin{bmatrix} E_g + \epsilon(\boldsymbol{k}_{||}) & i\frac{\hbar P}{m_0}\boldsymbol{k}_{||} & i\frac{\hbar P}{m_0}\boldsymbol{k}_{||} & 0 \\ -i\frac{\hbar P}{m_0}\boldsymbol{k}_{||} & \Delta - \epsilon(\boldsymbol{k}_{||}) & 0 & 0 \\ -i\frac{\hbar P}{m_0}\boldsymbol{k}_{||} & 0 & -\epsilon(\boldsymbol{k}_{||}) & 0 \\ 0 & 0 & 0 & -\epsilon(\boldsymbol{k}_{||}) \end{bmatrix} \tag{2.7}$$

Here $\boldsymbol{k}_{||}$ no longer represents the full 3D wavevector but now represents the quadrature sum of the wavevectors parallel to the 2D plane, i.e. $\boldsymbol{k}_{||} = \sqrt{(k_x^2 + k_y^2)}$. For the sake of simplicity $\boldsymbol{k}_{||}$ shall be referred to as $\boldsymbol{k}$ from this point. Inspection of equation 2.7 shows three coupled bands (conduction, spin split-off and the light hole) and a single decoupled band (the heavy hole) with the energy of the free particle. Accurate application of this model can be cumbersome and the pertinent effects can be crystallised by further reduction to the two-band model, neglecting coupling from the remote split-off band and the (effectively) dispersionless heavy hole band equation 2.7 reduces to

$$H_{2\mathrm{D}}(\boldsymbol{k}) = \begin{bmatrix} E_g + \epsilon(\boldsymbol{k}) & i\frac{\hbar P}{m_0}\boldsymbol{k} \\ -i\frac{\hbar P}{m_0}\boldsymbol{k} & -\epsilon(\boldsymbol{k}) \end{bmatrix}. \tag{2.8}$$

This model has the benefit of being analytically solvable and accurately describes the particle energies close to the zone center in both the conduction and light-hole bands,

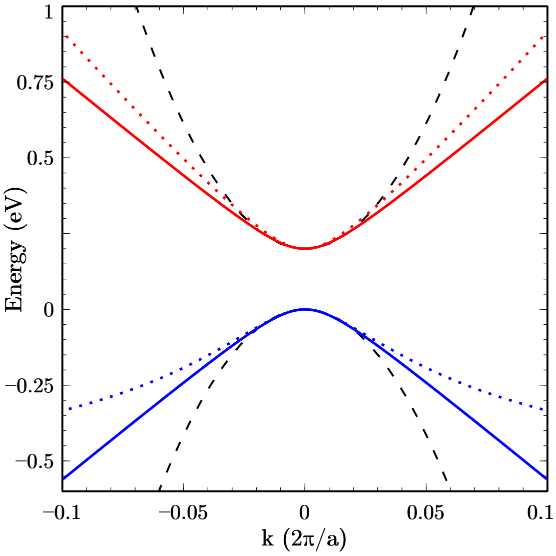

Figure 2.4: Conduction band (red) and light-hole valence band (blue) profiles for first 10% of the FBZ for InSb, calculated using the two-band model (solid line) and four-band model (dotted line). Also plotted is the parabolic band approximation (black dashed lines) of the electron and light hole states to highlight the rapid deviation away from the zone center.

with their dispersion relations described by

$$E_c(\boldsymbol{k}) = E_g + \sqrt{E_g^2 + \frac{\hbar^2 P^2 \boldsymbol{k}^2}{m_0^2}} + \epsilon(\boldsymbol{k}), \tag{2.9}$$

$$E_{lh}(\boldsymbol{k}) = -\sqrt{E_g^2 + \frac{\hbar^2 P^2 \boldsymbol{k}^2}{m_0^2}} - \epsilon(\boldsymbol{k}). \tag{2.10}$$

A comparison between this simple analytical expression and the results of a full four-band treatment is shown in figure 2.4 for the two bands. The two-band model clearly shows the deviation from the parabolic approximation at extremely small wavevectors ($\sim 2\,\%$ of the BZ) before tending to a linear relation with $\boldsymbol{k}$. The four-band model has more complex behaviour, no longer being linear at finite wave vector, though it maintains the significant deviation from the parabolic band. Consequently the analytical expressions of the two-band model can be used to determine other useful characteristics of narrow-gap materials without the headache of performing more cumbersome numerical calculations.

Combining equations 2.5 and 2.9 we can extract an expression for the effective mass of the material at the Γ point that purely depends upon the free electron mass and the coupling between the two states. Leaving the simple relation,

$$\frac{1}{m^*_{CB}} = \frac{1}{m_0} + \frac{2P^2}{m_0^2 E_g}. \tag{2.11}$$

This gives an explanation for one of the most remarkable characteristics of narrow-gap semiconductors, the light effective masses of carriers can be attributed to interband coupling. Using this we arrive at the common form for the non-parabolic conduction band dispersion relation,

$$E(1 + \lambda E) = \frac{\hbar^2 \boldsymbol{k}^2}{2m^*} \tag{2.12}$$

where $\lambda = 1/E_g$ (known as the non-parabolicity factor), and for the sake of simplicity the zero energy position is redefined to be at the conduction band edge.

Using a full eight-band model it is possible to calculate the energy separation between the two spin states for each band, though accurate estimation of these energies requires knowledge of remote band energies which for InSb are not well understood [30].

2.3 Heterostructures and Band Structure Engineering

The band structure and approximations used to describe the physical properties of carriers within a single crystal are well understood, though further complexity is added when crystals with dissimilar properties are placed in contact with one another. So called *heterostructures* can be engineered to have a wide range of electrical characteristics, detectors, switches, diodes, lasers, modulators all can be created by taking advantage of the electrical properties of material interfaces.

2.3.1 Heterojunctions

Three distinct types of heterojunctions can be formed which depend on the alignment of the conduction and valence bands (figure 2.5), the relative alignment of the band structure is determined by the electron affinity (χ) of each material and dictates the distribution of charge within the structure. Type I heterojunctions are formed when the

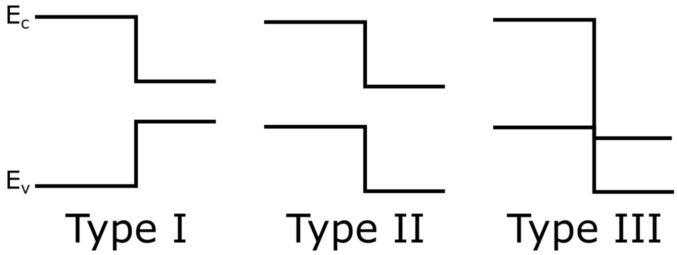

FIGURE 2.5: The three types of possible band alignment for a heterojunction.

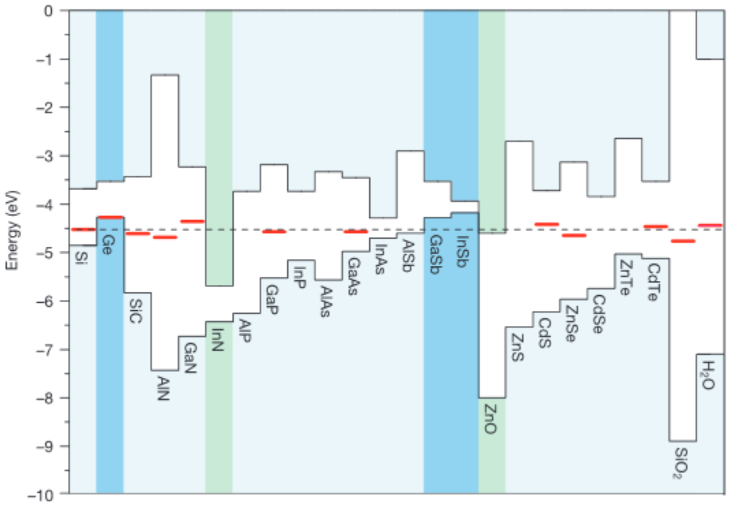

FIGURE 2.6: A comparison of the band alignments for a selection of materials, taken from [31]. The variation in energy of the valence band edge and size of the band gap hint at the variety of heterostructures that can be created.

band gap of one material is contained entirely within the band gap of the other material, this allows electrons and holes in the conduction and valence bands to decrease in potential energy by transferring from the wide gap material to the narrow gap material. Type II interfaces on the other hand decrease the potential energy of electrons in the conduction band in one material and decreases the valence band hole potential in the other material forming the junction. This introduces a charge separation at the interface as low energy electrons and holes are on different sides of the junction. Type III structures have an overlap between the valence and conduction bands across the interface, though the carriers are spatially separated they are energetically equal which allows for easy charge transfer across the interface.

2.3.2 Alloying

Heterostructures are not merely limited to the band structures or alignments available to us through the growth of binary materials. The introduction of a ternary material into the crystal has allowed for a great range of materials exhibiting different band gaps, band offsets and lattice constants. Figure 2.7 shows the relationship between III-V materials, their respective alloys, lattice constants and band gaps. AlSb has a lattice constant and bandgap of 6.14 Å and 1.7 eV respectively while similar properties of InSb are 6.48 Å and 0.18 eV. If the fraction of Indium in the crystal is altered to incorporate a percentage x of Al the resultant properties of that crystal are altered reflective of the ratio. This is summarised neatly as Vegard's law,

$$a_{alloy} = xa_A + (1-x)a_B \tag{2.13}$$

where a_{alloy}, a_A and a_B are the lattice constants of the alloy, material A and material B respectively. This linear relationship between composition and band parameters is idealistic in many cases with many materials having significant curvature depending upon their composition. $\text{Al}_x\text{In}_{1-x}\text{Sb}$ displays this ideal linearity up to a composition of around 60 % beyond which the bandstructure is no longer direct and the band parameters change quite differently with composition.

Growth technologies such as molecular beam epitaxy (MBE) or metal-organic chemical vapour deposition (MOCVD) have allowed for precise control of the alloy fraction of the materials grown allowing for dissimilar materials to be grown sequentially into the same structure. This potentially abrupt change in lattice constant introduces challenges to growth, the lattice mismatch between two materials introduces strain into the crystal structure that can disrupt the periodicity of the crystal and introduce defects as the atoms rearrange to minimise the strain. InSb has no lattice matched alloy so can only be grown unstrained on InSb substrates, which are significantly more expensive than more common GaAs or Si substrates.

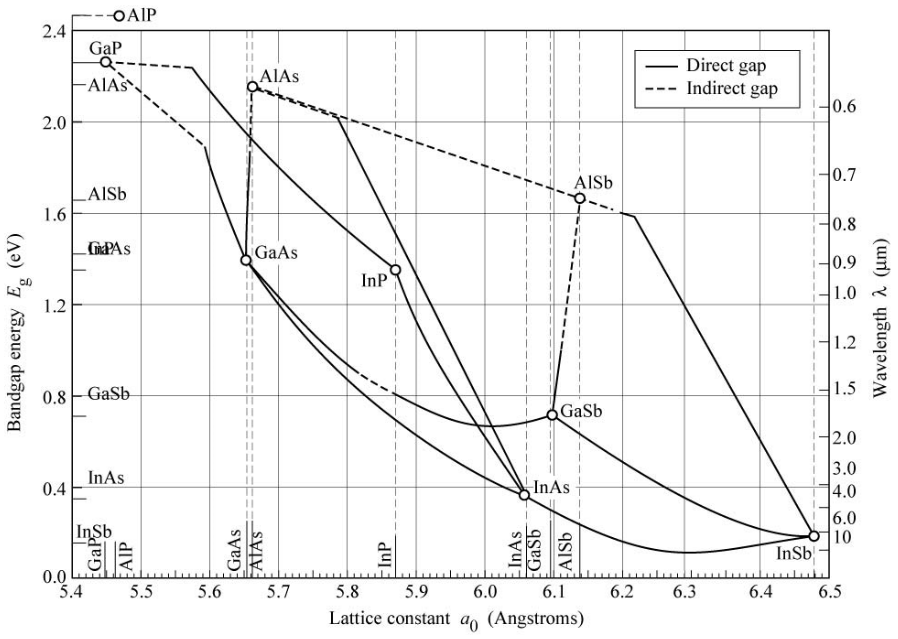

FIGURE 2.7: The conduction-valence band separation E_g as a function of lattice constant for the common III-V semiconductors and their alloys at room temperature. The small band gap of InSb is accompanied by one of the largest lattice constants of any semiconductor material.

2.3.3 Quantum Wells

Clearly by careful selection of materials and ordering of the growth process it is possible to grow crystals which have very specific band structures that can be tailored to suit specific device purposes. Growth of a narrow gap material such as InSb between two wider gap materials like AlInSb creates a region of electron states which are confined between two regions with an absence of states. Such a region of locally low potential energy is known as a quantum well due to the obvious analogy with the low gravitational potential energy of water well. If the physical dimension of this region is small enough (smaller than the thermal deBroglie wavelength of the carrier) the allowed states available to the carriers become quantised for particle motion in the growth direction, perpendicular to the growth direction the states remain unchanged. This state quantisation significantly alters the energy distribution of carriers in the well as well as their properties.

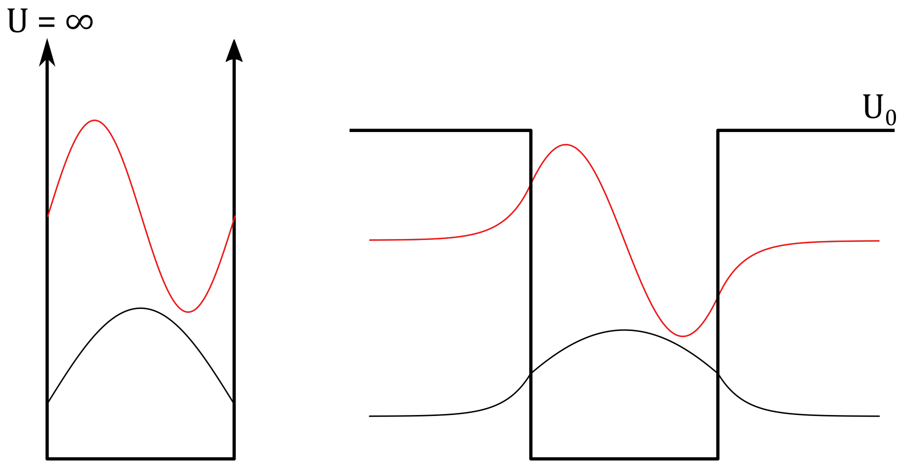

FIGURE 2.8: Schematic of the first two solutions for the confined states in both an infinite and a finite square well structure. The wavefunction solutions are drawn to highlight the penetration of the wavefunction into the barrier material in the case of the finite barrier height.

In the case of a well with an infinite barrier height an analytic solution to the energy of the quantised states is found to be,

$$E_n = \frac{\hbar^2\pi^2 n^2}{2m^* L^2} \tag{2.14}$$

where n is the integer of quantisation and L is the width of the quantum well. This is significant since the lowest energy quantised state is no longer coincident with the band edge observed in bulk materials, increasing the energy separation between the quantised conduction and valence band states.

In the case of the infinite square well the wave function of the carrier is contained purely inside the well region and cannot penetrate into the barrier material. The total energy of a particle is the sum of its kinetic and potential energies, with the infinite barrier potential the particle would require an infinite amount of energy to exist within the barrier material. A realistic case involves barriers of finite height, in this situation the wavefunction is no longer restricted to exist purely within the well and can penetrate by a finite amount into the barrier. As such we can no longer describe the wavefunction of the particle using the simple free particle Hamiltonian and must introduce the *effective mass Hamiltonian*, which takes the form,

$$\left[\frac{-\hbar^2}{2}\frac{d}{dz}\frac{1}{m^*}\frac{d}{dz}+V(z)\right]\psi = E\psi\,. \tag{2.15}$$

This imposes further restrictions onto the solutions to the Schrödinger equation. Not only does the wavefunction have to be continuous over the entire structure but also the derivative of the wavefunction *in both materials* has to be continuous to account for the difference in the effective masses of carriers in both the barrier and the well. Since there is now a finite chance of a particle existing inside the barrier the properties of the particle exhibit a mixture of the properties of particles in each material, hence particles described by wavefunctions that penetrate more deeply into the barriers exhibit more barrier like properties. The penetration of a wavefunction into the barrier depends upon the energy of the solution relative to the barrier height, more energetic solutions penetrate more deeply, and can be manipulated through the application of a bias to the structure, slewing the wavefunction toward one side of the quantum well.

In the plane of the quantum well there is no quantisation and the energy dispersion of carriers remains the same as if it were bulk material. The confinement of particles to a small region of space fundamentally changes the density of states ($g(E)$), defined as the number of states available per unit energy per unit volume, in a bulk 3D material the density of states is continuous and energy dependent,

$$g_{3D}(E)dE = \frac{1}{2\pi^2}{\frac{2m^*}{\hbar^2}}^{3/2}E^{1/2}dE\,. \tag{2.16}$$

When confined in one dimension the quantisation of energy introduces discontinuities in the density of states at certain energies (figure 2.9(a)). Under the parabolic approximation the density of states is constant within each sub band and increases each time another subband becomes occupied. The expression for the parabolic 2D density of states is given by,

$$g_{2D}(E)dE = \frac{m^*}{\pi\hbar^2}\Sigma_n\theta(E-E_n)dE\,. \tag{2.17}$$

Importantly the density of states is no longer energy dependent and the step discontinuities are represented by the Heaviside theta function $\theta(E - E_n)$. When the effects of non-parabolicity are taken into account the 2D density of states recovers an energy dependence since the effective mass of carriers increases at higher energies, hence the density of states also increases. A full derivation of the parabolic and non-parabolic 2D density of states is given in appendix A. A comparison between the density of states and the effective mass at the Fermi energy in the parabolic and non-parabolic approximations are shown in figure 2.9(a) and 2.9(b) respectively. Consequently carriers at the Fermi energy will have a larger effective mass than the low energy carriers at the band edge.

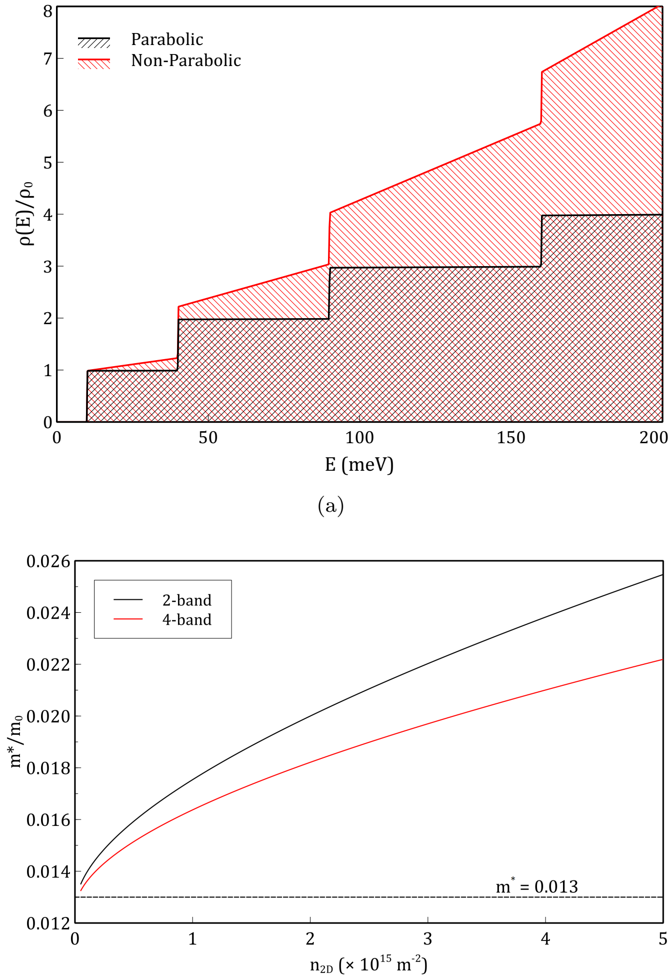

(a)

(b)

FIGURE 2.9: a) A comparison between the 2D density of states using the parabolic approximation and the non-parabolic density of states calculated using the two band model. The non-parabolic density of states rapidly increases lowering the Fermi energy of such materials. b) The effective mass of electrons extracted from the curvature of the conduction band for the 2 and 4-band Kane models. The band edge effective mass of $m^* = 0.013$ is shown to emphasise how significantly non-parabolicity can affect the properties of carriers in the conduction band.

Chapter 3

Samples, Fabrication and Measurement

The purpose of this chapter is to highlight the complete life cycle of the samples used in this Thesis, from the growth stages through processing and finally into the measurements performed to investigate the materials.

3.1 Growth of heterostructures

High quality, epitaxially grown crystals are an area of vigorous study for all manner of material systems, developments in *molecular beam epitaxy* (MBE) technologies have facilitated precise incorporation of impurity atoms into crystal structures in a technique known as modulation doping which have, in turn, facilitated the fine control of heterostructure band alignments allowing for surprising control over the electrical, optical and thermal properties of materials.

3.1.1 Epitaxy

MBE systems are ultra high vacuum (UHV) chambers where crystalline substrates inserted into the vacuum environment are exposed to elements in an atomic or molecular form, these elements then coalesce epitaxially on the substrate surface in a desired stoichiometric composition. The sources of these compositional atoms are solid source effusion cells, elementally pure material sources which are heated to evaporate atoms from the surface. The intensity of this incident beam is controlled both by temperature and mechanically through the use of a shuttering system which physically impedes the beam. Each MBE chamber is equipped with a certain range of effusion cells to grow a range of materials with specific dopants, independently controlling the temperatures of the effusion cells and the substrate, the shutter positions for each cell and the timing allows for precise control of material composition and layer thickness. All materials investigated in this thesis were grown by MBE at the EPSRC national epitaxy facility, Sheffield.

3.1.2 Studied Materials

The structures studied in this thesis were grown on semi-insulating GaAs substrates, which nominally had the following layer structure,

i. 25 nm $Al_{15}In_{85}Sb$ top cap

ii. Te δ-doping layer

iii. 25 nm $Al_{10}In_{90}Sb$ barrier

iv. 30 nm InSb quantum well

v. 3 μm AlInSb barrier layer

vi. 200 nm AlSb buffer layer

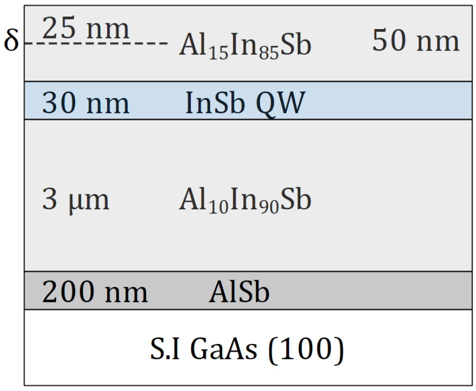

A self-consistent Schrödinger-Poisson solution to the above layer structure is shown in figure 3.1. A type I heterostructure is formed, localising electrons and holes in the quantum well, Te δ-doping ensures n-type dopant is incorporated into the crystal structure. The low potential region of the QW makes it energetically favourable for electrons to exist in the QW ionising the dopant atoms, the positive ions are spatially removed from

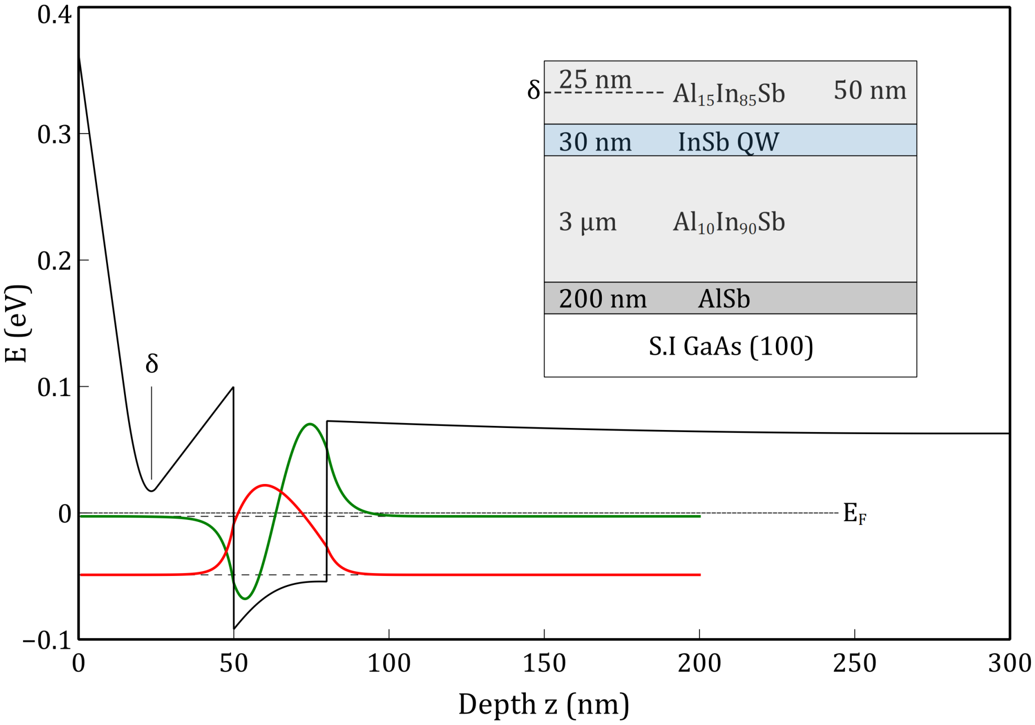

FIGURE 3.1: A self-consistent Schrödinger-Poisson solution for the typical layer structure of this material. The δ-dopant plane is heavily doped with Te and consequently contributes significantly to the carrier density of the quantum well. In this instance sufficient charge has been contributed for occupation of the second subband to occur, corresponding to a sheet carrier density of $n_{2D} \approx 3 \times 10^{15}\,\mathrm{m}^{-2}$. The inset is a schematic representation of the layer structure.

the QW reducing the scattering potential experienced by electrons and minimising scattering from the ionised impurities. Though there are reports of high mobility materials which incorporate Si doping both above and below the well [32], a single dopant plane above the QW is used in this heterostructure due to dragging of Te along the growth plane. This prevents high densities of impurities being located in the quantum well and minimises impact on the channel mobility. A number of samples with this layer structure were grown and an investigation into the effect of the dopant density was carried out.

3.2 Device Fabrication

Six-terminal gated and ungated Hall bar devices were fabricated using standard lithography techniques, acid etching and metal evaporation using the clean room facilities at Cardiff University. Dielectric depositions were done at the EPSRC national processing facility at Glasgow university and using facilities at Cardiff University.

3.2.1 Contact Photolithography

Photolithography is the technique of transferring a specific geometric pattern onto a material through the use of UV light, a patterned “mask” and a photosensitive polymer. When the polymer is illuminated through a mask, the UV light imprints the pattern into the polymer, which may then be removed to leave behind the original pattern. At each processing step a unique mask (a glass plate covered in an opaque chrome pattern) is used to pattern regions or features to allow further processing. Using these methods complex structures can be built up over multiple processing steps. The photosensitive polymer (more commonly referred to as photoresist) is dispensed as a liquid onto the sample surface and subsequently spun at high RPM to achieve an even coating across the entire surface. Once uniformly coated the sample is then baked to drive solvent off from the resist and leave behind a solid film. Contact photolithography is typically used to define patterns with features down to $\sim 1\,\mu$m, limited by the wavelength of the UV light and the extent of local vibration. After exposure the sample is chemically developed (in the photographic sense) to reveal the pattern left behind by the mask. This developed pattern can be either an exact copy of the mask pattern or a negative copy depending on the type of resist used (positive tone or negative tone respectively), this pattern can then be used as an etch mask or to confine deposition onto a region of the surface.

In processing samples used in this thesis, a *Karl Suss contact mask aligner* was used (either the MJB3 or MJB4 model) in concert with positive tone photoresists *Microposit* S1813 and *Microchem* PMGI SF11. These were baked at a temperature of no higher than 95 °C to minimise the chance of the resist reflowing and distorting the developed pattern, this hard baking of photoresist is also used to preserve material and minimise defect creep. When used as an etch mask, a single layer of S1813 was used (typically $\sim 1.3\,\mu$m thick). However, for the deposition of metal or dielectric a bi-layer resist profile must be employed, a thin initial layer of PMGI SF11 followed by a layer of S1813 (total thickness $\sim 1.5\,\mu$m). The SF11 underlayer produces an undercut to the S1813 when developed and minimises the chance of contiguous coating when metal is deposited, improving metal lift-off after deposition.

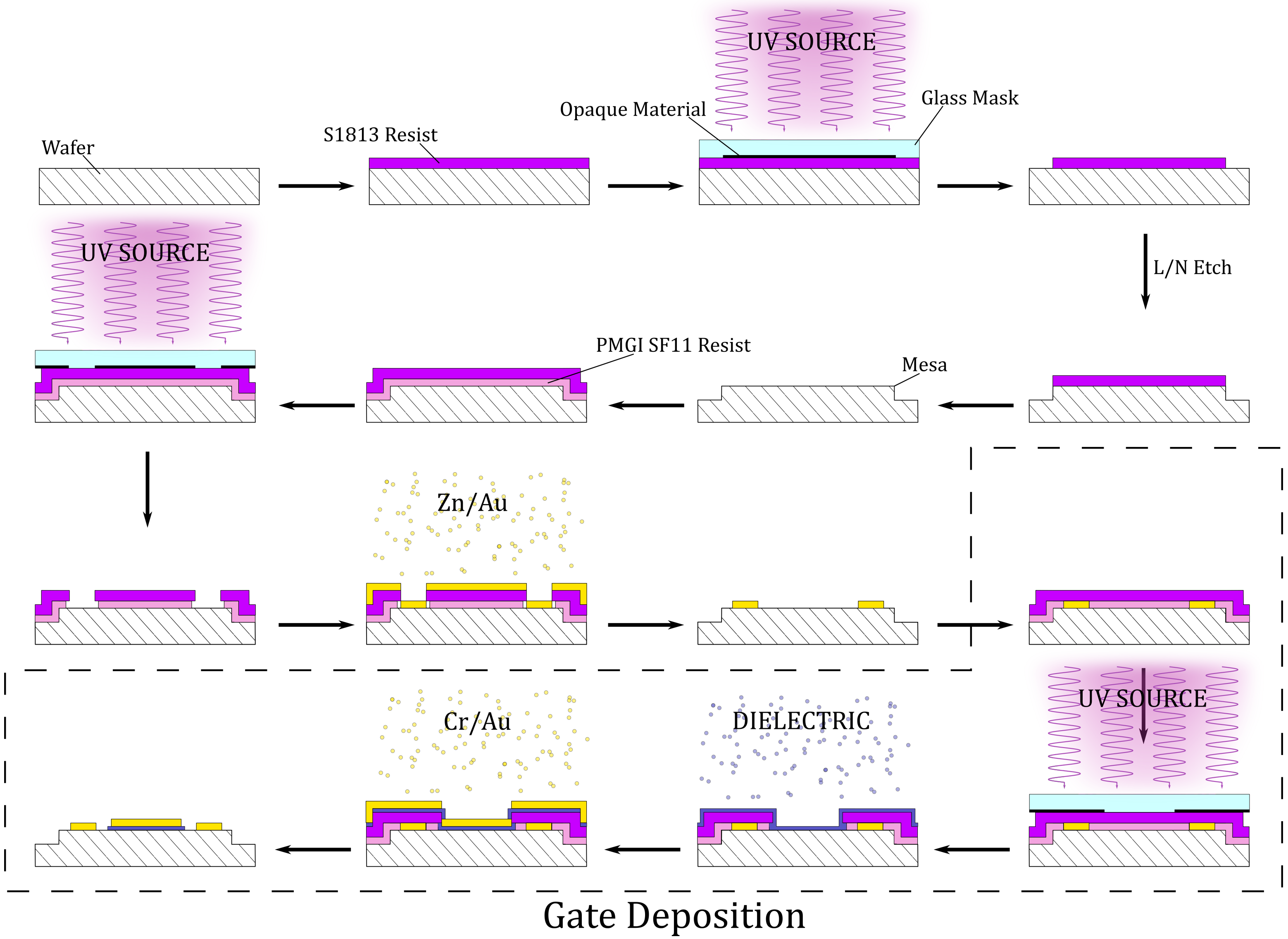
Wafer
S1813 Resist
Opaque Material
UV SOURCE
Glass Mask
L/N Etch
Mesa
PMGI SF11 Resist
UV SOURCE
Zn/Au
UV SOURCE
DIELECTRIC
Cr/Au
Gate Deposition

FIGURE 3.2: The complete processing sequence in the creation of both gated and ungated devices. Ungated devices are created by completion of the processing steps outside of the dashed area.

3.2.2 Hall bar devices

The magnetoresistance measurements presented in this thesis were performed using a conventional 6-terminal Hall bar design as shown in figure 3.3, the salient features of this design are:

i. The current probes (A & D) are sufficiently remote from the voltage probes (B,C,E & F) that carriers are adequately thermalised to the lattice temperature before reaching the voltage probes and a fully developed Hall voltage exists at the voltage probes.

ii. The length of the bar is much greater than its width such that any geometric component of the Hall voltage can be neglected. Typically an aspect ratio of 5:1 is used which allows for full formation of the Hall potential while minimising the length of the device .

iii. The Hall voltage probes exist at an electrical equipotential when $B = 0\,\mathrm{T}$ so the longitudinal and transverse components of the magnetoresistance measurements are orthogonal.

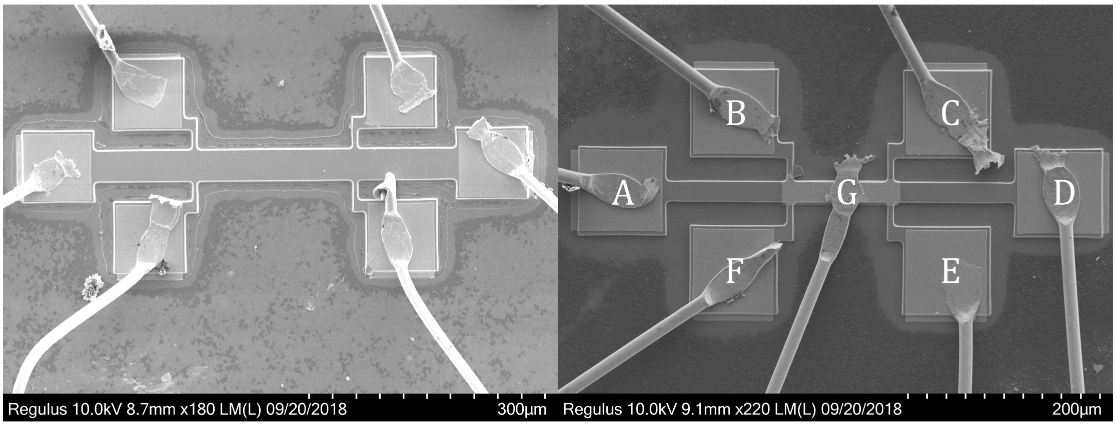
Regulus 10.0kV 8.7mm x180 LM(L) 09/20/2018
300µm
Regulus 10.0kV 9.1mm x220 LM(L) 09/20/2018
200µm
A
B
C
D
E
F
G

FIGURE 3.3: Scanning electron microscope images of a large ungated Hall bar and small gated Hall bar structure, both structures have a 5:1 ratio of length to width between the voltage probes. The gate is positioned such that the voltage probes measure the potential of the 2DEG underneath the gate.

Hall devices of 2 different sizes were fabricated using photolithography and wet etching, a large bar with an active region between voltage probes of length $200\,\mu\mathrm{m}$ and width

40 μm and a small bar with length 100 μm and width 20 μm. Investigations of the carrier density dependency were realised through the application of a gate electrode over the active region of the Hall bar, isolated by a low leakage dielectric barrier.

3.2.2.1 Ohmic contacts

Ohmic contact to the 2DEG was accomplished by thermal evaporation of metals using an Edwards E306 Thermal evaporator with a working distance of 20 cm. A Zn keying layer (around 10 nm) is initially deposited to improve adhesion to the surface followed by a thick Au layer (300 nm). These are evaporated while the substrate is heated to 100 °C to introduce more diffuse metal ions on the surface and minimise Schottky contact formation.

3.2.2.2 Gate contacts

Two types of dielectric were used for investigation throughout this thesis. A dielectric layer of Si_3N_4 was deposited at the James Watt Nanofabrication Centre (JWNC) at the University of Glasgow using an inductively coupled plasma - chemical vapour deposition (ICP-CVD) technique. A 20 nm dielectric film was deposited onto the surface at room temperature, a cold deposition technique was used to prevent lift-off issues due to reflow of the resist defining the gate aperture. A MgO dielectric was also used for a number of samples deposited using a sputter system at Cardiff University, these devices had a thicker dielectric layer of 30 nm.

Gate metal was subsequently deposited on top of the dielectric layer at Cardiff University by thermal evaporation using an Edwards E306 Thermal evaporator. A 10 nm Cr keying layer was deposited followed by a thick 300 nm Au layer whilst the substrate was attached to a water cooled stage.

Despite the thin dielectric layers, good, low leakage current dielectrics were achieved and modulation of the carrier density in the 2D system was observed.

3.3 Measurement Systems

All measurements described in this thesis were performed at Cardiff University using either a pulse tube, or cryogen free dilution refrigeration system.

3.3.1 Low field measurement system

Temperature dependent measurements between 300 K and 3 K were made using an *Oxford Instruments Optistat AC-V12*, a closed cycle, cryogen free, pulse tube refrigeration system. Compressed zero-grade He^4 gas is supplied by a water cooled *Cryomech CP830* compressor to a modified *Cryomech PT403* cold head providing 0.25 W of cooling power at 4.2 K capable of reaching base temperatures of ~ 2.8 K, as measured by a calibrated rhodium-iron thermometer. The cryostat consists of two heat exchanger plates at the ends of two pulse tubes connected in parallel. Oscillating gas pressure provided by the compressor passes through two regenerators (a type of heat exchanger) in series providing cold gas to the first and second stages and extracting heat from the system. The second stage has been modified with an ~ 30 cm cold finger attachment to allow samples mounted inside the cryostat to be positioned between the poles of an electromagnet. A simplified schematic of the pulse tube cryostat is shown in figure 3.4, more details on the design and operation of pulse tube coolers can be found in [33]. The refrigerated volume is held under vacuum provided by a *Leybold vacuum TURBOLAB 80* turbomolecular pumping system. Thermal variation is provided by a resistive heater mounted to the 3 K plate operated by an *Oxford Instruments Mercury iTC*. Temperature sweeps are controlled via software with incorporated delays to ensure samples at the end of the cold finger are in thermal equilibrium with the cold plate. Electrical connections to the cryostat were made by 10 pin *Fischer* connectors to braided, twisted pair, copper wires connecting to the DUT, thermometer and heater. Samples were mounted into a 20-way sprung contact chip carrier, thermal contact between the sample and the cold finger was provided by two bolts which force the sample package into contact with a copper block on the cold finger.

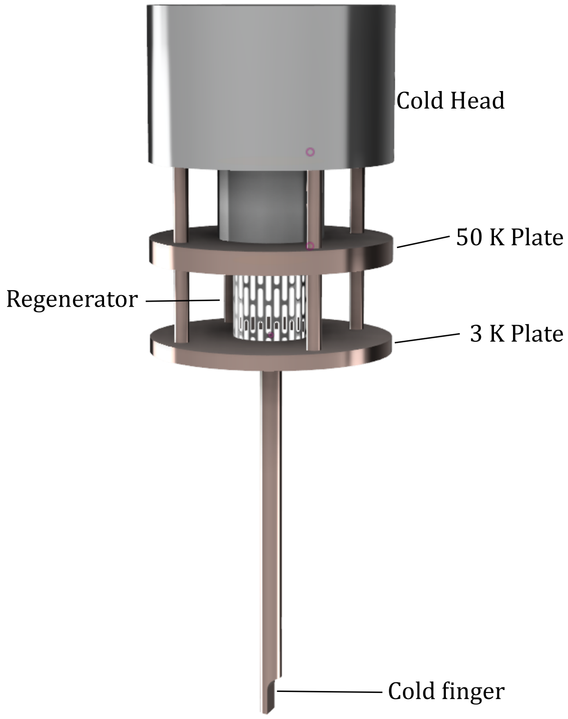

Figure 3.4: A simplified schematic of the closed cycle, cryogen free, pulse tube refrigeration system.

Operating in conjunction with this cryogenic system is a 0.85 T solid pole electromagnet with current control provided by an *Agilent N5769A* programmable DC power supply controlled through a GPIB interface. This refrigeration set-up provides a relatively rapid test system which can go from room temperature to 2.8 K in as little as 90 minutes and allows for low-field material characterisation at all temperatures in-between.

3.3.2 High field measurement system

Ultra-low temperature (10 mK measurements were carried out in a Bluefors LD250 cryogen free dilution refrigeration system (DR) with integrated superconducting solenoid magnet ($8T$). The majority of the cooling power is provided by a *Cryomech PT-410RT* pulse tube cryocooler with a *Cryomech CP2880* compressor, which cools all components of the DR to either 50 K or 4 K in the same manner as described for the previous system and provides 1 W of cooling power at 4 K. The volume of the DR is evacuated using an

Agilent SH-110 scroll pump and a *Pfeiffer HiPace 400* turbomolecular pump. Further cooling beyond 4 K is achieved by dilution refrigeration, a room temperature mixture of He^3 and He^4 gasses is compressed and circulated to the 4 K stage where it undergoes Joule-Thomson expansion and begin condensing into liquid He inside the mixing chamber. Once a critical temperature is reached the He^3 and He^4 undergo a phase change and begin to separate into a dilute phase composed $\sim 6.4\%$ He^3 in He^4 and a concentrated phase of pure He^3, since the He^3 isotope is less massive the concentrated phase floats on top of the dilute phase. He^3 is then evaporated from the dilute phase in the still by use of a heater To maintain the concentration of He^3 in the dilute phase some of the He^3 in the concentrated phase must cross the phase boundary, this provides cooling power that is proportional to the rate of flow of He^3 within the system and can supply up to $12\,\mu$W of cooling power at 20 mK.

Thermometry for the various stages was performed using a *Lakeshore 370* resistance bridge, the 4 K and Still plate thermometers were *Cernox* thin film resistance sensors and the mixing chamber temperature was extracted from a RuOx thin film resistor. To estimate the accuracy of the RuOx calibration a Coulomb blockade thermometer (CBT) was used to directly measure the thermal energy of electrons in the wires at the end of the cold finger. The two thermometers were found to be in agreement of ±1 mK at 12 mK. To allow the sample to be mounted in the region of uniform magnetic field an extension stick was designed to be mounted directly to the mixing chamber flange. This was then made at Cardiff University out of gold plated copper, consisting of a block which bolts directly to the mixing chamber flange, a tube with staggered slots milled into it to prevent eddy current heating during field sweeps and a smaller block to mount the sample holder. Samples were mounted into a *CMR-Direct mPuck* mounting system with 20 sprung contact pins, again thermal contact was provided by bolting the sample holder onto the copper block of the mounting stick.

To provide high magnetic fields an *American Magnetics* 8 T 3-inch NbTi superconducting magnet was used. Cooling is provided to the magnet through conduction by connection to the 4 K plate. Manipulation of the magnetic field is controlled by an *American Magnetics 430* power supply programmer via a RS232 interface which controls the *American*

Magnetics 4Q12125PS-430 four quadrant power supply.

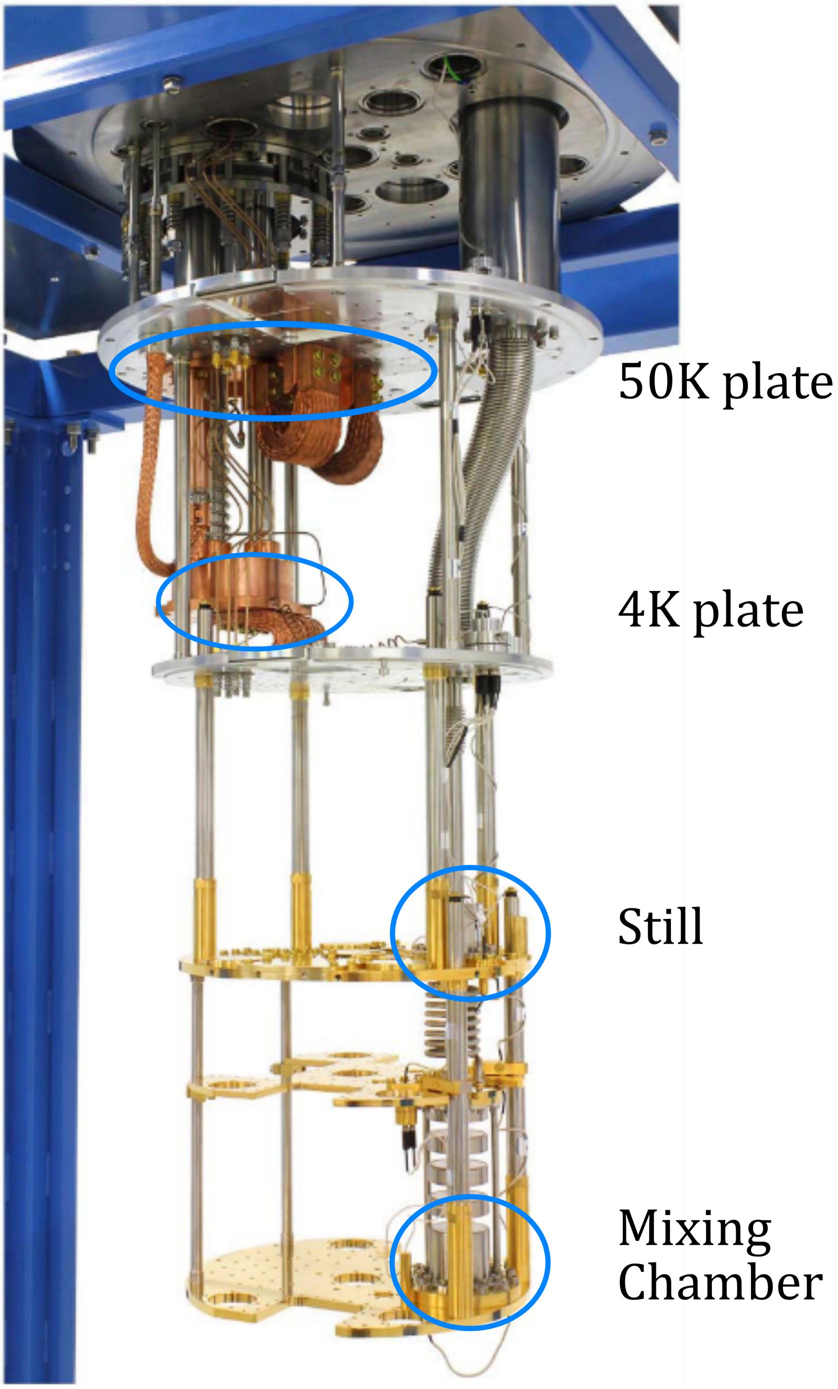

FIGURE 3.5: Image of the LS-250 dilution refrigerator interior, the impressively low temperatures are achieved by sequential staging of pulse tube and dilution refrigeration technology. The polished Au coating on the low temperature stages is to minimise thermal emissivity and limit absorption of any incident thermal radiation.

This system has the advantage of providing extremely low temperatures and large fields, minimising the need to consider any thermal aberration to a measurement and enables the distinct observation of spin states due to Zeeman interaction. The large volume of the DR means that rapid cool down is not an option, a full thermal cycle of the DR with the magnet attached takes a minimum of four days without including measurement time. As such this system was not used to characterise all samples measured in the low field measurement system.

3.4 Magnetotransport Measurements

3.4.1 Hall effect measurements

Gated and ungated Hall bar devices were mounted inside 20-pin ceramic chip carriers allowing up to 3 devices to be measured during a single cool down. Electrical connection between the chip and the carrier was made using a wedge wire bonder and 13 μm Au wire. A schematic of the measurement set-up is given in figure 3.6. A delta-mode[*] constant current measurement technique with a current amplitude of up to $\pm 1\,\mu$A was supplied by a *Keithley 6221* current source. Currents in excess of 1 μA were avoided to limit Joule heating in the device. The field control and data acquisition was controlled using bespoke computer software, written in either Python or Labview. Longitudinal and transverse differential voltages were measured using a *Keithley 2182A* dual channel precision voltmeter and gate control was provided by an *Agilent E5281B* precision, medium power SMU module. To ensure all voltage levels were recorded relative to a common ground potential the circuit ground of the *Agilent E5281B* was connected to the ground potential of the *Keithley 6221*. The benefits of sourcing a constant current becomes apparent in the context of the Shubnikov-de Haas effect where the material resistivity varies as a function of magnetic field. The current source provides the bias necessary to source the chosen current and the voltages measured are true reflections of the magnetoresistance of the sample.

---

[*] A delta-mode measurement consists of DC current of alternating polarity synchronised to a voltage measurement. This removes both thermoelectric and geometric aberrations to the measured voltage.

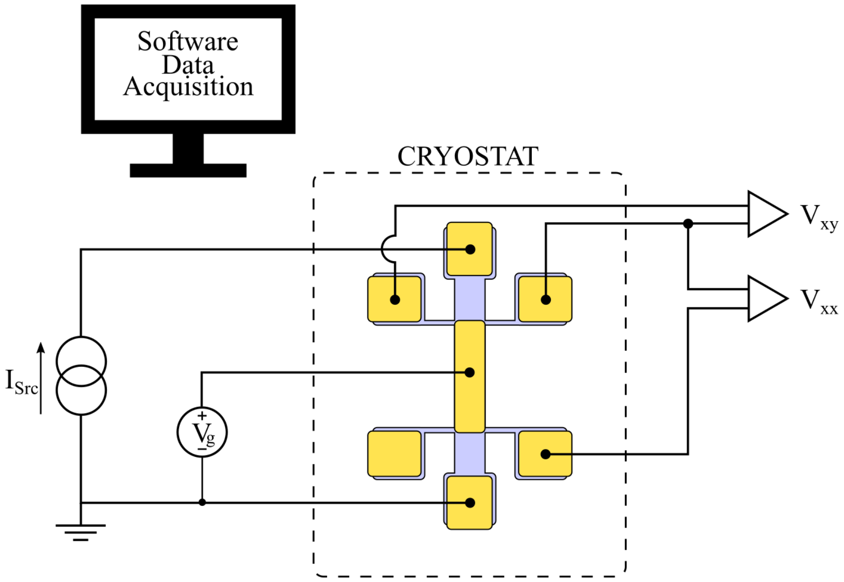

FIGURE 3.6: A typical schematic for a gated magnetoresistance measurement. The differential inputs V_{xx} and V_{xy} represent the longitudinal and Hall voltages respectively. Non-gated structures are measured in the same manner excluding the gate connection.

3.4.2 Three terminal IV measurements

Using the same gated Hall bar structures DC current-voltage (I(V)) measurements were performed using a *National Instruments Compact Data Acquisition Card* (DAQ) system while a low frequency AC differential conductance measurement was simultaneously made using the same equipment. To measure the DC and AC currents the circuit path to ground is completed through a *Stanford Research Systems SR570* low-noise current pre-amplifier with no AC filters applied, converting the small signal current into an easily measurable voltage. The differential voltage measurement was made using a *Stanford Research Systems SR560* low-noise voltage preamplifier. A current limiting (10 kΩ) resistor placed in series with the DUT ensured that none of the low noise equipment was overloaded. The AC signal to measure the differential conductance was extracted using software lock-in techniques using Labview software[†].

The three terminal measurement is performed to remove the effects of the series resistance of the 2D channel from the voltage measured between the common contact and the remote voltage probe. This allows information about the contact to be extracted from the I(V) data. In the limit where the contact resistance dominates, all of the voltage measured by the remote probe is dropped across the contact.

[†] The Labview software used for data acquisition in all three terminal measurements was written by Dr. Steve Clowes.

A schematic of the measurement set-up is given in figure 3.7 as well as the equivalent circuit.

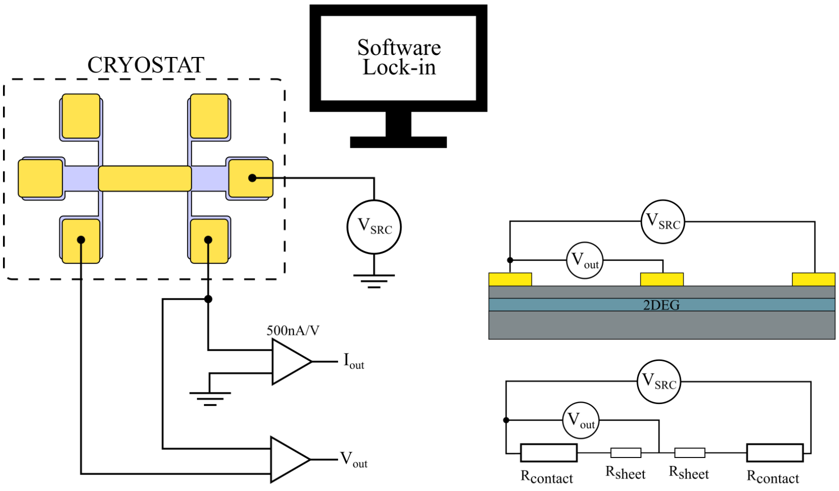
CRYOSTAT
Software Lock-in
V_{SRC}
500nA/V
I_{out}
V_{out}
V_{SRC}
V_{out}
2DEG
V_{SRC}
V_{out}
$R_{contact}$
R_{sheet}
R_{sheet}
$R_{contact}$

(a) (b)

Figure 3.7: (a) A schematic of the three terminal I(V) measurement set-up and (b) its equivalent circuit. The common contact for the voltage measurement and the current drain was chosen to be the most resistive contact on the device to maximise the voltage drop across the contact.

3.5 Sample summary

Table 3.1: A Table summarising the nominal high and low temperature classical transport properties for some of the heterostructures studied in this thesis. The values quoted for the gated samples were calculated from data measured with the gate electrode connected to ground.

			300K		3K	
Sample No.	QW (nm)	dopant spacer (nm)	n ($\times10^{15}/\mathrm{m}^2$)	μ (m^2/Vs)	n ($\times10^{15}/\mathrm{m}^2$)	μ (m^2/Vs)
SF0963	30	25	3.0	4.7	2.5	18.0
SF0968	30	25	2.7	5.1	2.1	16.8
SF1054	30	25	3.9	4.7	3.5	25.0
SF1055	30	25	3.1	4.9	3.1	23.5
SF1056	30	25	3.0	5.0	2.1	19.5
Gated Samples						
SF1055	30	25	3.6	4.2	3.1	14.1
SF1056	30	25	3.1	4.4	2.1	10.4

Chapter 4

Magnetotransport measurements on 30nm InSb/AlInSb quantum well heterostructures

The extreme electronic properties of bulk InSb have long been acknowledged as important for the study of fundamental transport physics. The possibility of creating a two-dimensional electron gas in InSb that capitalises on the improved transport properties observed in other heterostructures has also made it a prime candidate for the observation of spin related effects. In spite of this, due to growth difficulties, InSb quantum wells have received relatively little investigation compared to other narrow gap semiconductors such as InAs.

Understanding the transport mechanisms which dominate within these heterostructures is important for the continued development of material quality and subsequently improving the transport properties. The work presented in this chapter highlights characterisation techniques used to study these transport phenomena in a number of modulation doped InSb/AlInSb quantum wells. Magnetotransport measurements at low and moderate fields are compared to extract electron lifetimes while thermal effects are considered to determine the effective mass of carriers.

Section 4.1 introduces the fundamentals of carrier transport under the influence of small magnetic fields, discussing the physics underlying the Hall effect and highlighting the carrier properties which can be inferred from field dependent and temperature dependent measurements. Following this, section 4.2 details transport properties in the limit of high magnetic fields and provides a brief discussion of the effects of non-parabolicity and sample inhomogeneity.

4.1 Classical electron transport

Two key metrics used to determine the transport quality of a 2D material are the sheet carrier density (n_{2D}) and the mobility (μ). These describe the relative abundance of charge carriers and how prone they are to undergoing scattering events within the material, and combined they define the conductivity of a material. These properties as well as the charge of the majority carrier can be inferred by electrical measurement while the carriers are under the influence of electric and magnetic fields. While under the influence of a magnetic field perpendicular to the carrier momentum, charged particles experience a Lorentz force perpendicular to both their motion and to the magnetic field which causes them to undergo cyclotronic motion. When the rate of carriers undergoing significant scattering events ($1/\tau$) is greater than the cyclotron frequency (ω_c) carriers are considered to be in a low field regime of magnetotransport. Within this regime carrier transport can be accurately described by the classical description of electrical transport defined by Drude [25], indeed this is where the concept of a characteristic scattering time comes from.

4.1.1 Fundamental transport equations

In the presence of thermal excitations the ensemble of electrons within a material have a distribution of momenta which carry no net charge within the material. Under the influence of an electric field ($\boldsymbol{E}$) these electrons experience a force that is proportional to $\boldsymbol{E}$ i.e. $\boldsymbol{F}_E = -e\boldsymbol{E}$. This force accelerates electrons in the opposite direction of applied field and introduces a net current flow throughout the region where the field is applied which can be described as a *drift velocity* ($\boldsymbol{v}_d$) of carriers. The Drude assumption that electrons are non-interacting particles except when they undergo a scattering event means that (on average) electrons have to be accelerated to this drift velocity within the characteristic scattering time. The combination of the drift velocity and the number density of carriers present in a material dictates the current density,

$$\boldsymbol{J} = ne\boldsymbol{v}_d = \frac{ne^2\tau\boldsymbol{E}}{m^*}. \tag{4.1}$$

This is Ohm's law, describing the current density arising for a given electric field. The other terms in equation 4.1 defines the conductivity of the medium. The conductivity of a material under the influence of only an electric field may thus be described by the equation,

$$\sigma_0 = \frac{ne^2\tau}{m^*} = ne\mu \tag{4.2}$$

where μ is defined as the mobility of carriers in a material and is proportional to the characteristic scattering time and inversely proportional to the effective mass. The magnitude of the mobility of a material is therefore dependent upon the dominant scattering mechanisms and the type of carrier contributing to conduction. The considerable difference between the electron and heavy-hole effective mass is the primary reason why n-type materials are considered preferable to p-type for high frequency applications.

The assumption that carriers undergo diffusive transport that can be described by Drude theory therefore depends upon the scale of the devices being measured being significantly greater than the distance traversed by electrons between scattering events, known as a carriers *mean free path* (ℓ). This characteristic length scale can be estimated by considering carriers at the Fermi energy with a velocity $\boldsymbol{v}_F$ and how far they travel within the scattering time. For high quality InSb 2DEGs the mean free path can be of the order of many μm [34–37] in the highest quality materials. Within the parabolic band approximation[*] the mean free path can be described by,

---

[*] When the consequences of non-parabolicity are considered the increasing density of states at higher energies reduces $\boldsymbol{v}_F$ and subsequently reduces the mean free path.

$$\ell = \boldsymbol{v}_F \tau = \frac{\hbar \mu}{e} \sqrt{2\pi n_{2D}}, \tag{4.3}$$

evidently the mean free path is proportional to the mobility and to the square root of the carrier density. The sample sizes considered in this thesis are at least an order of magnitude larger than the mean free path of the electrons in the highest mobility material, hence the transport can safely be considered to be in the diffusive transport regime.

4.1.2 The Hall effect

The motion of charge carriers through both electric and magnetic fields was first described by Edmund Hall in the 19th century. He observed that in the presence of a magnetic field a voltage perpendicular to both the current and magnetic field is established. This has proved to be a remarkable tool and is still a standard technique for the characterisation of material quality, while also being exploited for many commercial applications pertaining to magnetic field sensing.

If a 2D sheet of material (figure 4.1), oriented in the x, y-plane has a voltage applied to the sheet along the x-axis, this produces an electric field E_x. The conventional current created due to the presence of the electric field I_x travels parallel to E_x. Perpendicular to the x, y-plane and to E_x is the magnetic field B_z, and under the influence of these fields electrons are subject to both an electrostatic and Lorentz force with the net force being described by $\boldsymbol{F}_{Tot} = (-eE_x, -ev_d B_z, 0)$. The electrons experience a net force in the x, y-plane directed away from the x-axis. Carriers subject to this force are directed toward the edge of the sheet, accumulating charge. This charge build up establishes a transverse electric field which opposes the Lorentz force. Charge continues to accumulate until the forces from the transverse electric field and the Lorentz force reach an equilibrium and charge continues to flow only along the x-axis once again. The polarity and magnitude of the transverse electric field can be measured as a voltage between the opposing sides of the sheet. This is known as the Hall voltage V_H. The polarity of V_H indicates the charge of the majority carrier contributing to conduction. Negative V_H indicates majority

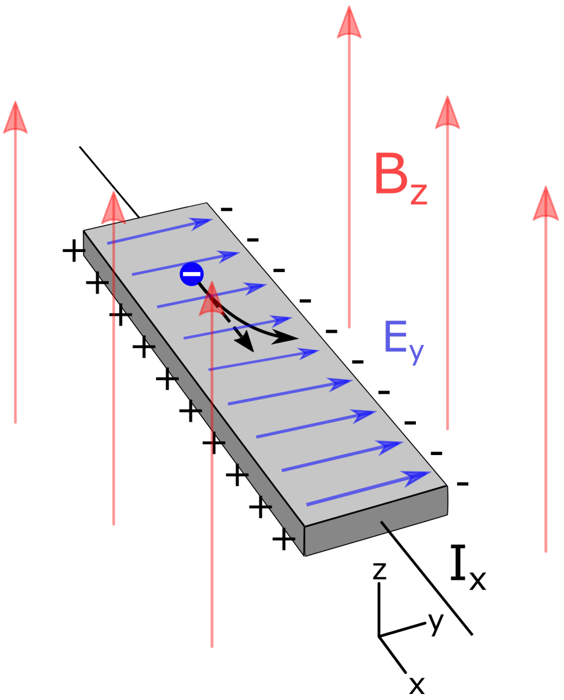

Figure 4.1: A schematic representation of the forces present on charges moving through a magnetic field to produce the Hall effect.

electron conduction while positive V_H indicates hole conduction. The magnitude of V_H is given by the equation,

$$V_H = \frac{B_z I_x}{e n_{2D}}, \tag{4.4}$$

intuitively the magnitude of the Hall voltage is proportional to the strength of the magnetic field, the magnitude of the current, and inversely proportional to the sheet carrier density. However, the presence of the magnetic field has the complicating effect of altering the conductivity of the material, at non-zero field the conductivity splits into discrete components described by the conductivity tensor,

$$\sigma = \begin{pmatrix} \sigma_{xx} & \sigma_{xy} \\ \sigma_{yx} & \sigma_{yy} \end{pmatrix} \tag{4.5}$$

where $\sigma_{xx,yy}$ is the tensor component of a material's conductivity along a coordinate axis due to forces along the same axis, and $\sigma_{xy,yx}$ is the tensor component of a material's conductivity due to orthogonal forces. These off-diagonal components arise due to the perpendicular forces acting on carriers in the magnetic field contributing to the material conductivity in the direction perpendicular to the electric fields. This perpendicular force causes carriers to undergo cyclotronic motion which has a characteristic length scale ($\ell_{cyc} = m^* v_F / eB$) known as the cyclotron radius. Any geometric aberration between voltage probes can lead to inaccurate measurement of the longitudinal or transverse conductivities. The geometry of the Hall bar structures studied in this thesis allow for simultaneous measurement of both the Hall voltage and the voltage drop along the Hall bar with negligible deviations from the true values arising from geometric error[38].

4.1.3 Carrier analysis

The samples investigated in this thesis were grown with a variety of doping densities in the δ-dopant layer to characterise the material as a function of the sheet carrier density. Figure 4.2 shows the quantum well mobility as a function of the sheet carrier density for all measured materials extracted from a simple single carrier model at 3 K. A peak in mobility of $23\,\mathrm{m^2V^{-1}s^{-1}}$ occurs at a density of $n_{2D} \approx 3.5 \times 10^{15}\,\mathrm{m^{-2}}$, away from this peak the mobility decreases rapidly indicating that scattering processes increase. These can be attributed to two distinct scattering mechanisms. At low temperature the dominant scattering mechanism comes from interaction of electrons with the Coulomb potential of the ionised dopants in the δ-dopant plane. The bare Coulomb potential has a $1/r$ dependency and since the δ-dopant plane is spatially removed from the 2DEG by nominally 25 nm the Coulomb potential encountered by electrons is reduced. This is known as *remote ionised impurity scattering* and can be the dominant scattering mechanism in 2DEGs. Due to the presence of electrons in the quantum well the Coulomb potential is further reduced due to the effects of Thomas-Fermi screening [26]. This screening causes the Coulomb potential to fall off exponentially faster than the $1/r$ dependence of the bare potential. Higher carrier densities in the quantum well lead to greater screening of the Coulomb potential and a reduction in the scattering rate from the remote ionised impurities. This screening effect increases with the amount of charge in the well until some other scattering mechanism becomes dominant.

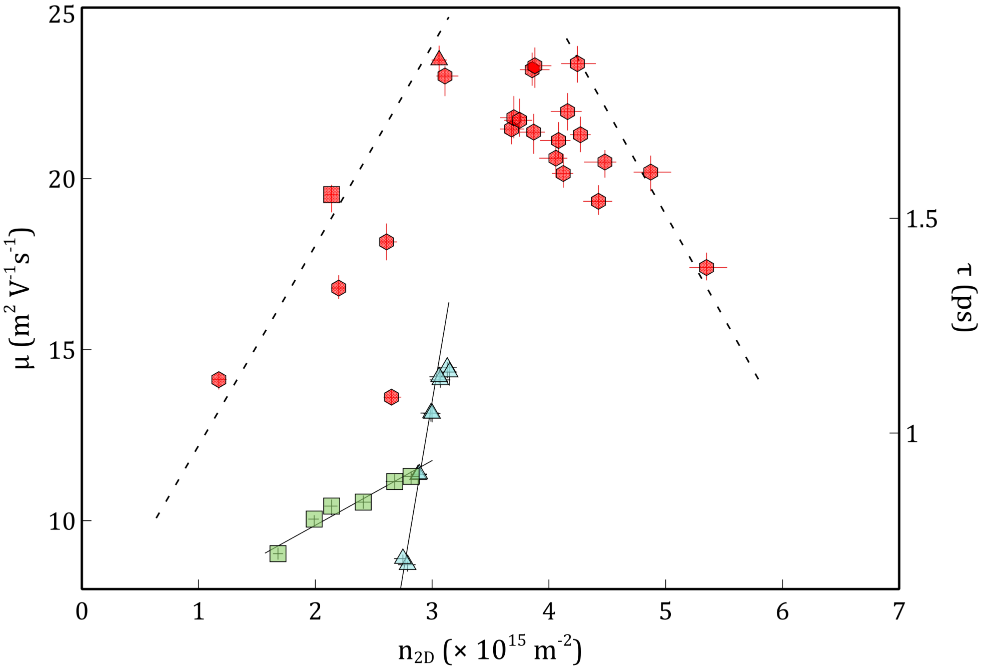

FIGURE 4.2: Carrier mobility against sheet carrier density extracted from single carrier fitting for all InSb/AlInSb quantum well samples. The dashed lines are a guide to the eye to highlight the fall off in mobility at low and high carrier densities. The red data are ungated samples while green and blue were fabricated with a CrAu gate electrode on top of amorphous MgO and Si_3N_4 dielectrics respectively. Square or triangular markers indicate structures made using the same material.

The energy separation between the first and second subbands for the quantum well have been calculated from Schrödinger-Poisson modelling to be around 40 meV. Estimation using equation 2.12 and the band edge effective mass means the carrier density in the well only has to reach $\sim 2.8 \times 10^{11}\,\mathrm{cm}^{-2}$ before the second subband becomes occupied. Inter subband scattering has been shown to reduce the overall mobility of samples[39, 40] when the Fermi energy is close to the second subband. There is also evidence that the mobility decrease is due to states in the δ-dopant layer becoming occupied and the reduced mobility of the state in the heavily doped region adversely affecting the quantum well mobility [34].

In this second regime estimation of the carrier mobility and sheet carrier density from the simple single carrier estimation is not ideal. The presence of a second carrier with a different mobility and carrier density can be discerned from the Hall data through the use of multi-carrier fitting to the now non-linear Hall response and longitudinal resistivity. The total conductivity can be expressed as the sum of the individual contributions from each carrier for each medium [41, 42], i.e.

$$\sigma_{Tot} = \begin{pmatrix} \sigma^a_{xx} + \sigma^b_{xx} & \sigma^a_{xy} + \sigma^b_{xy} \\ \sigma^a_{yx} + \sigma^b_{yx} & \sigma^a_{yy} + \sigma^b_{yy} \end{pmatrix} \tag{4.6}$$

where $\sigma^{a,b}$ represents the conductivity contributions from the different carriers. This treatment proves useful at high temperatures when donor impurities in the buffer layer are ionized and significant parallel conduction through the buffer material occurs. It is particularly adept at discerning parallel conduction channels with similar conductivities but very different mobilities and carrier densities. Figure 4.3 shows a comparison between the simple single carrier approximation and the more complex two carrier model. Clearly for high carrier density materials the single carrier method provides an indication of the transport properties but importantly also shows the limitations of a single field Hall measurement. The presence of a second parallel conduction path requires the use of more complicated models and Hall measurements at multiple fields to accurately determine values for the carrier transport properties.

Uncertainties in the transport properties extracted using this method were determined by a rudimentary resampling procedure. Longitudinal and Hall voltage data were randomly varied by up to a standard deviation and the fitting procedure was performed, this was done iteratively to build up statistics for the transport properties. All samples which displayed parallel transport at low temperature were well characterised by two n-type carriers as we would expect if the parallel channel was the second subband of the quantum well.

4.1.4 Temperature dependence of the transport properties

Characterisation of the transport properties as a function of temperature can help determine the dominant scattering mechanism. Matthiessen's rule[25] describes the mean scattering rate of a material as being the sum of all individual scattering rates for each scattering mechanism, i.e.

$$\frac{1}{\tau_{tot}} = \sum_i \frac{1}{\tau_i}. \tag{4.7}$$

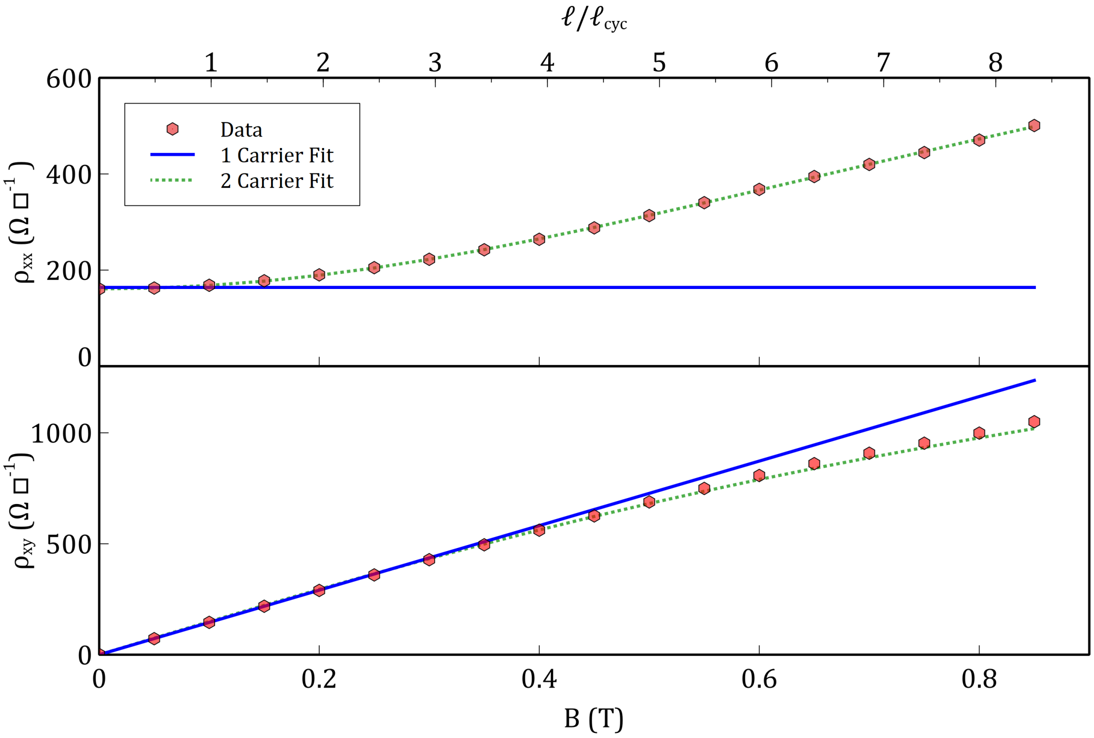

Figure 4.3: A comparison between single and two carrier fitting to magnetoresistance data at 130 K for sample SF1054. The single carrier model is most valid when the cyclotron radius (ℓ_c) is larger than the mean free path (ℓ). The single carrier model extracts a carrier density and mobility of $3.9 \times 10^{15}\,\mathrm{m}^{-2}$ and $22.7\,\mathrm{m}^2\mathrm{V}^{-1}\mathrm{s}^{-1}$ respectively, while the two carrier model extracts a high mobility carrier with density $3.5 \times 10^{15}\,\mathrm{m}^{-2}$ and mobility $25.0\,\mathrm{m}^2\mathrm{V}^{-1}\mathrm{s}^{-1}$.

This assumes that all scattering rates considered are independent. Different scattering mechanisms have a variety of energy dependencies and many of them contribute to the transport properties.

The following are short descriptions of a number of the scattering mechanisms that contribute significantly to the transport properties of these InSb/AlInSb heterostructures.

Phonon scattering

At finite temperature atoms in the crystal have thermal kinetic energy. This atomic motion leads to local deformation in the periodicity of the crystal lattice and inhomogeneity in the local density of states. In diatomic crystals both acoustic and optical phonons occur. Acoustic phonons are produced by in-phase crystal oscillations while optical phonons are created by out of phase oscillations which lead to local polarisation.

The acoustic phonon scattering rate is proportional to the deformation potential of the crystal (Ξ) and the temperature, described by [24, 43–45],

$$\frac{1}{\tau_{ac}} = \frac{3k_BT}{2}\frac{m^*\Xi^2}{\hbar^3\rho_d v_s^2 w} \tag{4.8}$$

where ρ_d is the crystal density, v_s is the speed of sound in the crystal, w is the width of the quantum well and k_B is the Boltzmann constant. The deformation potential for InSb varies greatly in the literature and is not well known ranging between 4.2 - 33 eV [46] depending on the measurement technique. This large variation in deformation potential allows for a modification of the room temperature acoustic phonon scattering time between $1 - 60$ ps. The scattering rate from optical phonons is given by,

$$\frac{1}{\tau_{op}} = \frac{e^2m^*\omega_0 w}{4\pi\epsilon_p\hbar^2}\frac{1}{\exp\left(\frac{\hbar\omega_0}{k_BT}\right) - 1} \tag{4.9}$$

where ω_0 is the phonon frequency and $\epsilon_p = \epsilon_0\epsilon_\infty/(\epsilon_\infty - \epsilon_0)$ where ϵ_0 and ϵ_∞ are the DC and infinite frequency dielectric constants respectively. It is important to note that τ_{op}^{-1} is exponentially proportional to temperature and quickly becomes insignificant at temperatures < 100 K [24].

Ionised impurity scattering

As mentioned in section 4.1.3 ionised impurity scattering is a Coulombic interaction which is analogous to Rutherford scattering. Most interactions consist of shallow angle scattering which does not significantly affect the flow of charge but occasionally there is a significant back scattering event due to a “head on” collision. In modulation doped heterostructures the dopant charge lies outside of the 2D channel (aside from unintentional doping inside the 2DEG) and the ionised impurity scattering becomes dominated by shallow angle scattering. The scattering rate from remote ionised impurities in a δ-plane is given by [24],

$$\frac{1}{\tau_{rii}} = n_{imp}^{2D}\frac{m^*}{2\pi\hbar^3k_F^3}\left(\frac{e^2}{2\epsilon_0\epsilon_r}\right)^2\int_0^{2k_F}\frac{\exp(-2q|d|)}{(q+Q_{TF})^2}\frac{q^2dq}{\sqrt{1-(q/2k_F)^2}} \tag{4.10}$$

where n_{imp}^{2D} is the $2D$ impurity density from ionised donors, k_F is the Fermi wave vector, ϵ_0 and ϵ_r are the permittivity of free space and the relative permittivity respectively, q is the scattering wave vector, $Q_{TF} = 2m^* e^2/\epsilon_0 \epsilon_R \hbar^2$ is the $2D$ Thomas-Fermi screening wavevector and d is the distance between the δ-dopant plane and the position expectation value for electrons in the well.

Unintentional doping within the heterostructure can also provide a source of scattering due to ionised impurity scattering potential which is no longer solely dependent upon a single plane of charge but as a result of the $3D$ distribution of impurities n_{imp}^{3D}, described by

$$\frac{1}{\tau_{bkg}} = n_{imp}^{3D} \frac{m^*}{2\pi\hbar^3 k_F^3} \left(\frac{e^2}{2\epsilon_0 \epsilon_r}\right)^2 \int_0^{2k_F} \frac{1}{(q+Q_{TF})^2} \frac{q dq}{\sqrt{1-(q/2k_F)^2}}. \tag{4.11}$$

Importantly, aside from any small deviations arising from the non-parabolic effective mass of InSb the scattering from ionised impurities is independent of temperature. Figure 4.4 shows the typical mobility trend of these heterostructures as a function of temperature. Below 30 K the mobility is almost completely temperature independent indicating that at low temperature we are dominated by a temperature independent scattering mechanism, such as ionised impurity scattering.

Structural defect scattering

While investigating these heterostructures Hayes *et al.* [34] determined that for realistic $3D$ background doping densities the transport mobility predicted from modelling with typical InSb parameters did not agree with previous modelling [24, 47]. They therefore suggested an additional scattering mechanism was required for the transport model to fit the measured data. McIndo *et al.* [35, 48] have suggested that the grain size of the InSb might be this limiting scattering mechanism. If the average grain size is smaller than the mean free path of electrons between remote ionised impurity scattering events then this can account for the mismatch between measurement and theory. There is currently some debate whether this scattering mechanism or remote ionised impurity scattering is dominant at low temperature [45].

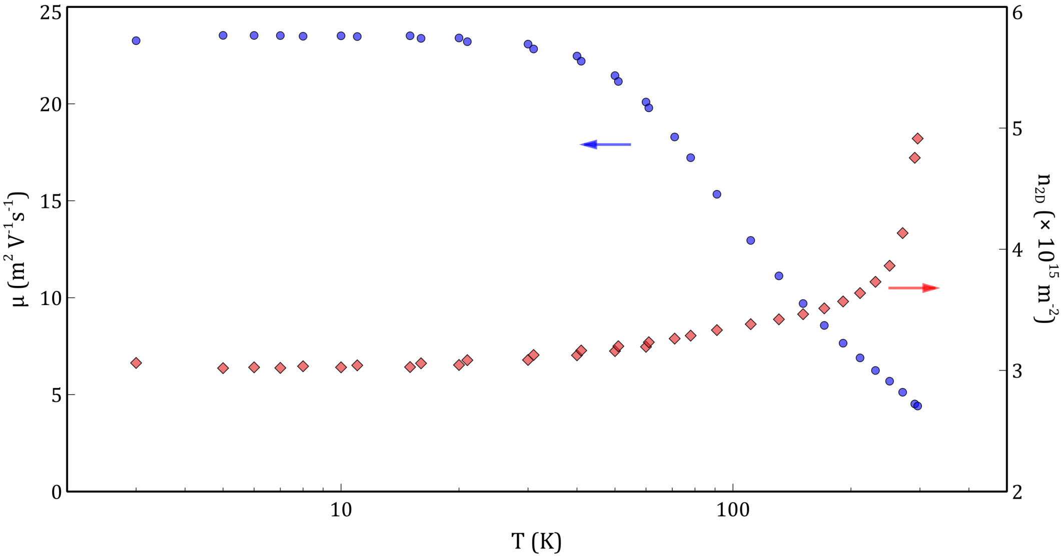

FIGURE 4.4: The carrier mobility and sheet carrier density extracted from single carrier fitting as a function of temperature. The reduction in carrier density is consistent with the freeze out of intrinsic carriers at low temperature.

4.2 Electron transport in the high field regime

Under the effects of large magnetic fields the resistivity of a material undergoes some non-intuitive effects. Figure 4.5 shows the longitudinal and Hall resistivity for a sample up to 8 T. The longitudinal resistivity oscillates with a single period as the magnetic field strength increases while the Hall resistivity increases with increasing field but also displays distinct plateaux. These are known as *Shubnikov-de Haas* (SdH) and *integer quantum Hall* (IQH) effects respectively and are not predicted by the classical theory of transport in the presence of a magnetic field.

These phenomena can be explained by introducing magnetic field interactions into the Schrödinger equation using the substitution $\boldsymbol{p} \rightarrow \boldsymbol{p} + e\boldsymbol{A}$, where $\boldsymbol{p}$ is the momentum operator $-i\hbar\nabla$ and $\boldsymbol{A}$ is the magnetic vector potential. Unlike the magnetic field the vector potential is not invariant under translation or rotation in the x, y-plane, using the Landau gauge, where $A = \begin{pmatrix} 0 \\ xB \\ 0 \end{pmatrix}$ the Schrödinger equation becomes

$$H\psi = \frac{1}{2m^*}\left[-i\hbar\frac{\partial}{\partial \boldsymbol{r}} + e\boldsymbol{A}\right]^2 \psi\,. \tag{4.12}$$

Solutions to this equation take the form of an harmonic oscillator,

$$E = \hbar\omega_c \left(N + \frac{1}{2} \right) \tag{4.13}$$

where $\hbar\omega$ is the cyclotron energy (ω is the cyclotron energy $eB_\perp/m^*$) and N is an integer starting at 0. This elegant solution means that under a perpendicular magnetic field the density of states in the transport plane becomes quantised into a ladder of discrete energy states with separation $\Delta E = \hbar eB_\perp/m^* = \hbar\omega_c$. These discrete states are known as *Landau levels*. The energy of each Landau level defines the kinetic energy of the electrons in the x, y-plane and hence the radius of the Landau level orbit. This leads to another characteristic length scale known as the magnetic length $\left(\ell_B = \sqrt{\frac{\hbar}{eB}}\right)$ which describes the orbital radius of the fundamental Landau level and is only $\sim 25\,\mathrm{nm}$ at $1\,\mathrm{T}$. This quantisation of the density of states means that, without modification, an electron's energy would increase linearly with $B_\perp$; however, simultaneously the magnetic field increases the degeneracy of states by an amount proportional to $B_\perp$. The degeneracy of states is defined as [49]

$$\mathcal{N} = \frac{eB_\perp}{2\pi\hbar}. \tag{4.14}$$

When spin is introduced into the system the degeneracy of each spin state is lifted and the energies are modified by $E = \pm\frac{1}{2}g\mu_B B$ due to the Zeeman interaction of the electron spin states with the applied magnetic field, g^* is the effective g-factor and μ_B is the Bohr magneton. The effects of Zeeman splitting can clearly be discerned in figure 4.5 at fields $\gtrsim 1.5\,\mathrm{T}$.

In a dispersionless system the energy of a Landau level would be described by a δ-function with all electron states occupying that level being completely degenerate; however, real systems are far from this ideal. The presence of scattering mechanisms in a material leads to broadening of the Landau levels which can be described by Gaussian functions [50, 51] with a width Γ. It is this broadening which explains why the effects caused by the discretisation of energy states are not observed at low fields. When the energy separation between Landau levels is smaller than the broadening then the density of states is quasi-continuous, Shubnikov-de Haas oscillations become observable once the

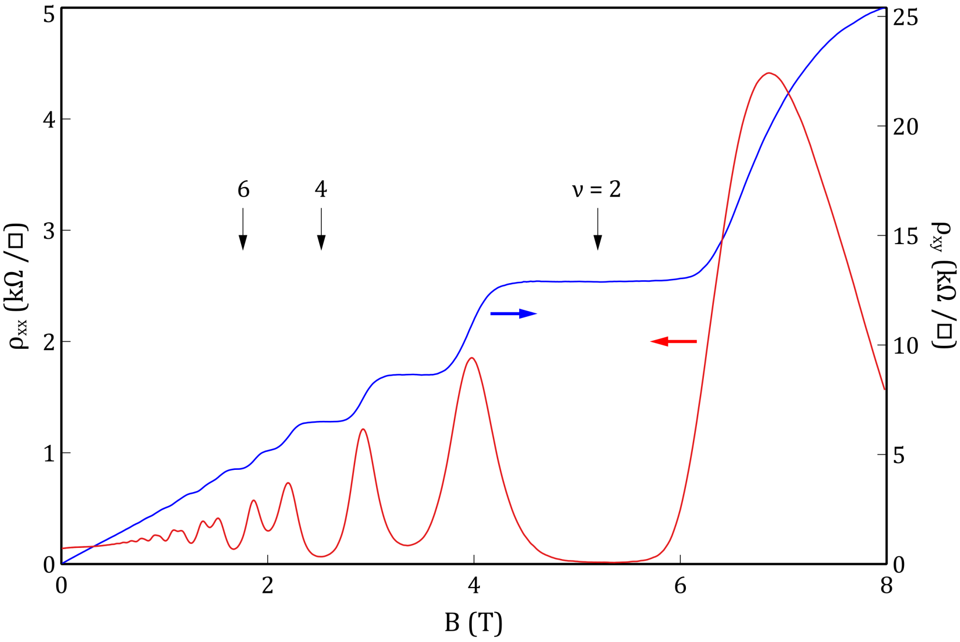

FIGURE 4.5: The Shubnikov-de Haas (red) and IQH (blue) effects measured at 12 mK for sample SF0968.

Landau level separation becomes comparable to the broadening. Figure 4.6 shows the evolution of the Landau level density of states with increasing magnetic field, the zero-field parabolic 2D DOS is shown for comparison.

The resistivity oscillations in the Shubnikov-de Haas effect are caused by a corresponding oscillation in the DOS at the Fermi energy. When a Landau level is coincident with E_F there are many states available for momentum scattering events to occupy and fewer when E_F lies between Landau levels. The variation of E_F as a function of field is discussed in more detail in chapter 5. As the magnetic field increases the number of Landau levels below E_F decreases, this is described by the *filling factor* [52],

$$\nu = \frac{2\pi n_{2D}\hbar}{eB_{\perp}} \tag{4.15}$$

which indicates how many Landau levels are occupied for a given carrier density at a specific field. This highlights a powerful analytical tool of SdH oscillations, the relationship between the periodicity of oscillation and the carrier density allows for the extraction of the carrier density simply by inspecting the periodicity in $1/B$. A Fourier transform of an ideal, single carrier SdH oscillation in $1/B$ will yield a single peak the frequency of

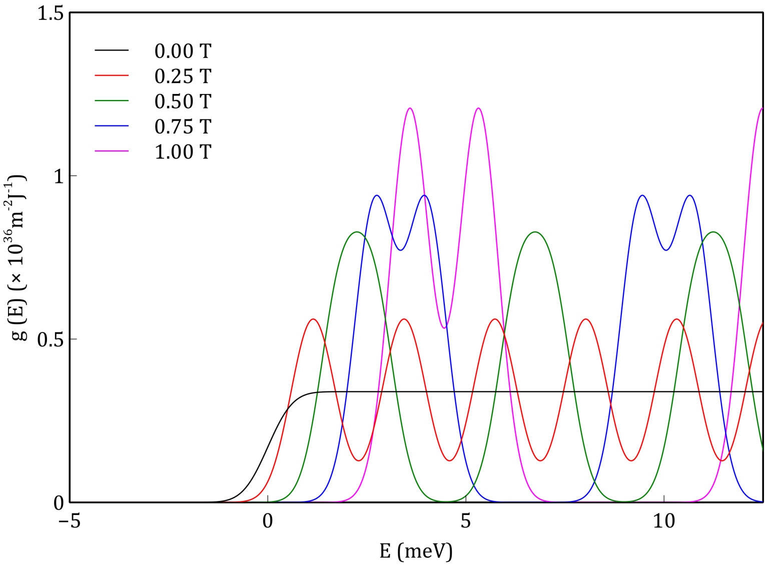

Figure 4.6: A Gaussian broadened Landau level model of the evolution of the 2D density of states for a single subband in InSb with increasing magnetic field. The 2D oscillations become significant when $\Gamma \leq \hbar\omega$. Spin split oscillations can be observed when the Zeeman contribution is larger than the broadening.

which is related to the carrier density by,

$$n_{2D} = \frac{2eB_F}{h} \tag{4.16}$$

where B_F is the peak frequency from the Fourier transform. The Fourier transform is a powerful tool for identification of periodicities in a magnetoresistance oscillation which can contain multiple oscillations of different frequency. Indeed, in high carrier density systems where a second subband is occupied, Fourier transform techniques can be used to determine the relative carrier densities of the two subbands [53]. This has been used extensively to investigate Rashba and Dresselhaus contributions to spin splitting in materials with large g^* such as InSb or InAs [54, 55]. However this oscillation in the DOS is not sufficient to describe the phenomena of the IQHE. First observed by von Klitzing *et al.* [56] in a Si inversion layer, the Hall resistivity displays plateau over a range of magnetic fields, the conductance of which is quantised into steps of ie^2/h, where i is any positive integer. These plateaux have been shown to be due to the existence of extended and localised states within the material, localised states carry no current while the extended states move toward the edges of the material to conduct via edge states. The presence of impurities in the 2D system has been shown to have no effect on the resistance values of each plateaux in the Hall measurement [57–59]. These striking results means that the IQHE is independent of material, purity and geometry and has been observed in many 2D systems [32, 36, 56, 60].

4.2.1 Quantum lifetime extraction

The scattering lifetime, τ, discussed earlier is the mean time between an electron undergoing a significant momentum scattering event. This is not, however, necessarily an accurate estimate of the *actual* time between an electron undergoing any individual scattering event. In remote doped heterostructures an electron can encounter many long range scattering potentials which only perturb the carriers momentum slightly before it undergoes a critical back scattering event which contributes significantly to the measured resistivity [61]. The characteristic lifetime τ is therefore highly dependent upon the scattering angle θ, such that $\tau^{-1} \propto (1 - \cos(\theta))$ and can be a considerable overestimate of the actual carrier lifetime or *quantum lifetime* (τ_q).

Extracting a value for τ_q can be achieved by analysis of the amplitude of the low-field Shubnikov-de Haas oscillations shown in figure 4.7. The amplitude of oscillation ΔR in terms of the zero-field resitance value R_0 is described by [62]

$$\frac{\Delta R}{R_0} = 4\chi_T e^{\left(\frac{-\pi}{\omega\tau_q}\right)} \tag{4.17}$$

where $\chi_T = \frac{A}{sinh(A)}$ is the thermal damping factor of the oscillation with $A = \frac{2\pi^2 k_B T}{\hbar\omega}$. This approximation ignores the effects of higher harmonics from the periodic expansion of the cosine term in [61]. As one would expect the thermal damping term is strongly temperature dependent, hence accurate quantum lifetime measurements require low temperatures to allow for low-field oscillations to be discernible. χ_T is also dependent on effective mass. The small effective mass of InSb means oscillations are still observable at temperatures where the damping factor would dominate in other materials [34]. Figure 4.8 compares χ_T for InSb and GaAs at different temperatures using band edge parameters, and highlights the low field extent to which low temperature oscillations could potentially be observed in InSb.

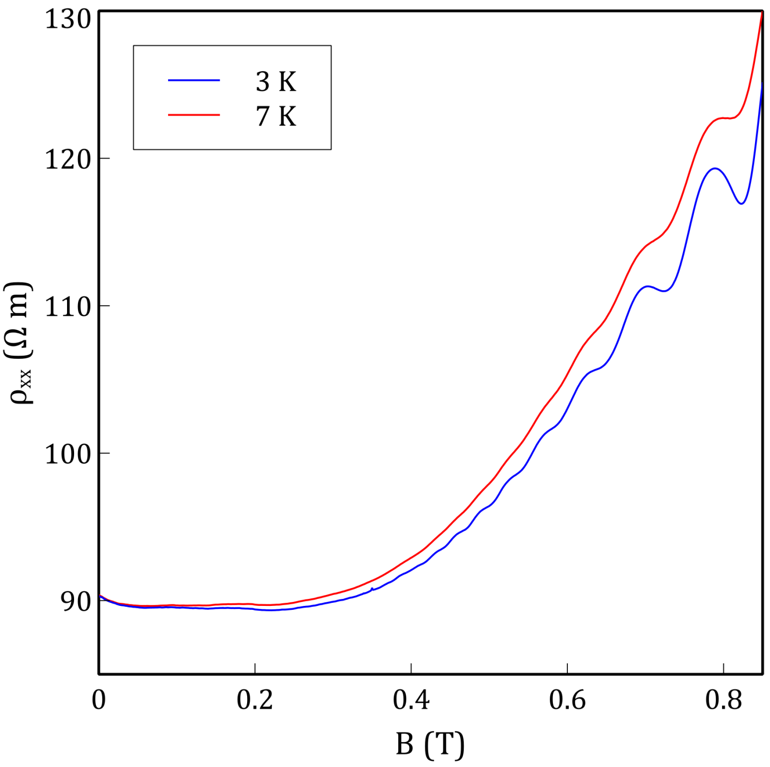

FIGURE 4.7: Typical low field resistivity trace of sample SF1055. The obvious Shubnikov-de Haas oscillations at 3 K are noticeably diminshed by 7 K.

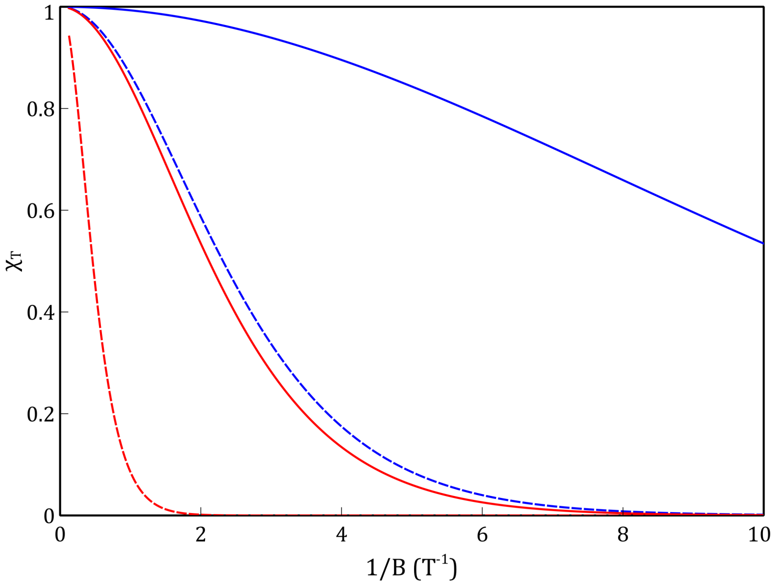

FIGURE 4.8: Thermal damping factor χ_T for InSb (solid) and GaAs (dashed) at 1 K (blue) and 5 K (red) calculated using the band edge effective masses of 0.014 m* and 0.043 m* respectively. Clearly the damping factor for InSb at 5 K is similar to that of GaAs at 1 K highlighting why the quantum lifetime in InSb can be discerned at higher temperatures.

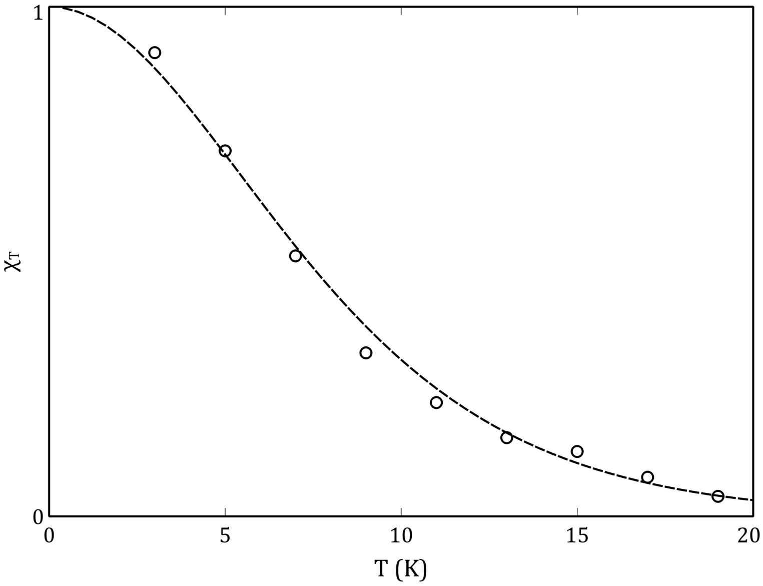

FIGURE 4.9: The thermal damping term as a function of temperature for ungated sample SF1055. The data are extracted from a field value of $B = 0.75\,\mathrm{T}$, the dashed line is fit using a least squares minimisation.

4.2.1.1 Thermal dependence of the quantum lifetime

Analysis of the SdH oscillation amplitude at various fields as a function of temperature allows us to extract a value for the in-plane effective mass. The amplitude is proportional to the damping factor, where the only free fitting parameters are the effective mass and finite temperature normalisation. This assumes that all oscillations are manifestations of a single quantum lifetime such that τ_q is independent of temperature, which is not necessarily true for low density heterostructures[32, 63]. Figure 4.9 shows the clear agreement between the damping factor and temperature, using a least squares minimisation a best fit to the data was achieved with an effective mass of $\mathrm{m}^*/\mathrm{m}_0 = 0.018 \pm 0.003$, the error estimation was again achieved using a simple bootstrapping[†] method. The carrier density for this sample extracted by both the two-carrier and FT methods discussed earlier yield densities of $n_{2D} = 3.15 \times 10^{15}\,\mathrm{m}^{-2}$ and $n_{2D} = 3.11 \times 10^{15}\,\mathrm{m}^{-2}$ respectively. Using a 4-band **k.p** method (see chapter 2) at this density carriers at the Fermi energy are expected to have a mass of $m^*/m_0 = 0.019$, which is in excellent agreement with the value extracted here.

[†] A bootstrapping procedure is a statistical confidence test where data are replaced by randomly deviating each data point by up to a standard deviation from the mean value.

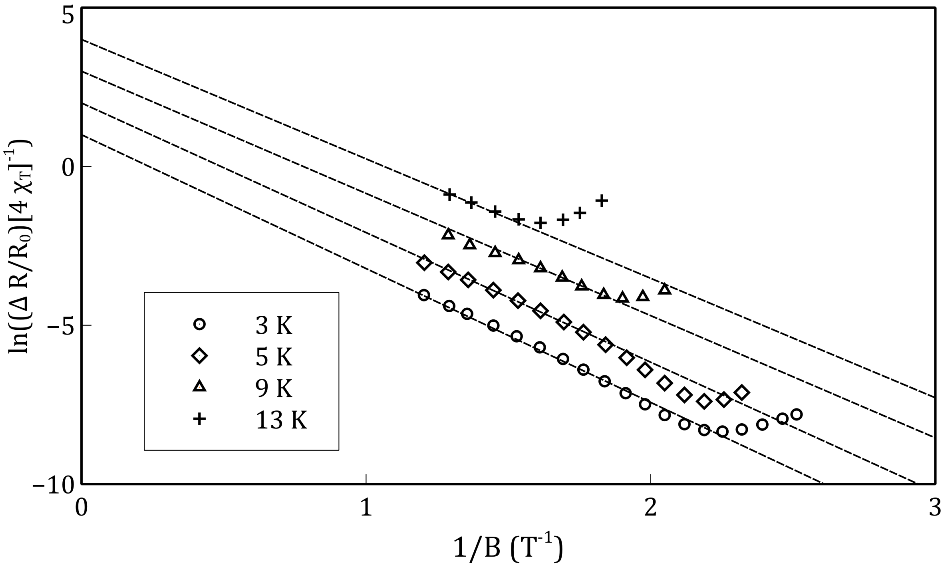

FIGURE 4.10: Dingle plot for sample SF1055 at various temperatures. The dashed lines are linear fits forced to an intercept of 1 to highlight the data quality. Elevated temperatures have been offset by integer values for clarity.

Rearrangement of equation 4.17 allows the quantum lifetime to be extracted from the gradient of a so called Dingle plot, $\ln(\Delta R/(4R_0\chi_T))$ versus B^{-1} (figure 4.10). Using this method samples which show ideal single carrier behaviour are expected to have an intercept of 1 and be well described by a straight line, though sample inhomogeneity [64] and parallel conduction [39] can cause deviation from this idealistic behaviour. Figure 4.10 shows Dingle plots for a range of temperatures, even up to 13 K the linear trend of the data is obvious though deviations from the straight line fits become apparent at lower fields. Peaks and troughs in the SdH oscillations were deduced from a graph of $\frac{-\partial^2\rho_{xx}}{\partial B^2}$. The small amount of data at higher temperatures is due to the oscillation amplitude becoming indiscernible below a threshold value of $1/10^{th}$ the peak amplitude. At low field values all data show a rapid upward turn in the Dingle plot, the point of curvature moves to higher field as the temperature increases corresponding with the exponential drop off of χ_T.

The extracted values of τ_q are shown in figure 4.11 for various temperatures. The data shows no obvious dependence upon temperature, suggesting that the dominant scattering mechanism is a temperature independent one such as remote ionised impurity scattering. Murphy [63] measured the electron lifetimes in GaAs/AlGaAs double well heterostructures with approximately one third to one half the carrier density of the

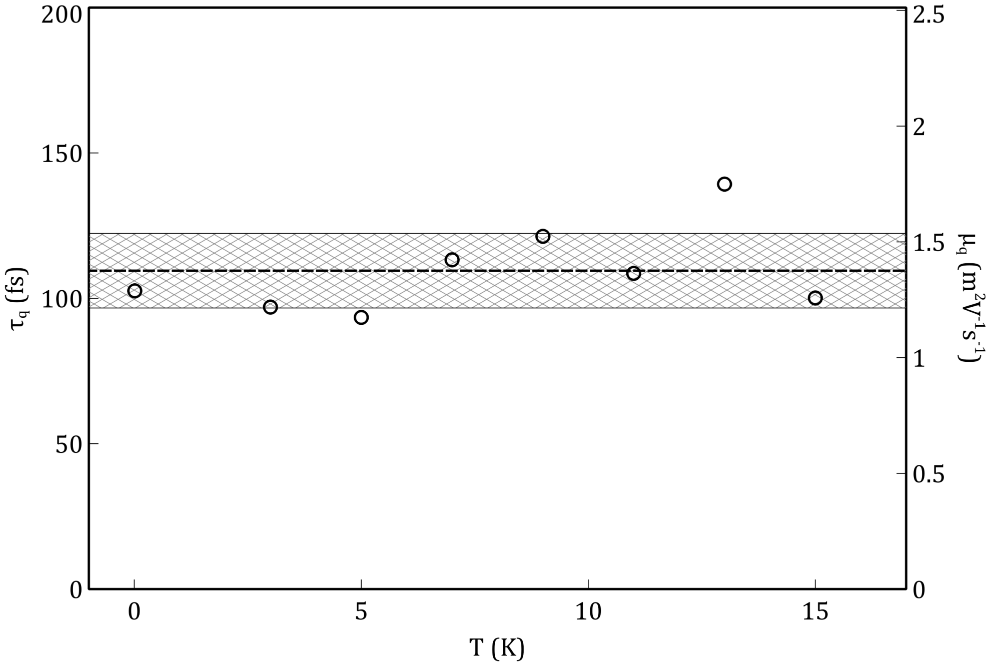

FIGURE 4.11: The extracted quantum lifetime and corresponding quantum mobility as a function of temperature for sample SF1055. The dashed line is a guide showing the mean value while the cross-hatched region highlights a standard deviation around the mean.

samples studied here. They observe a strong T^2 dependence of τ_q^{-1} which becomes more pronounced at low carrier densities, which is attributed to enhanced inelastic electron-electron scattering events. Giuliani and Quinn [65] determined the scattering rate from e-e interactions in an ideal 2DEG to be

$$\frac{1}{\tau_{e-e}} \approx \frac{-E_F}{2\pi\hbar}\left(\frac{k_BT}{E_F}\right)^2\left[ln\left(\frac{k_BT}{E_F}\right) - ln\left(\frac{Q_{TF}}{k_F}\right) - ln(2) - 1\right]. \tag{4.18}$$

This predicts electron-electron limited quantum lifetimes of ~ 200 ps at 3 K and ~ 6 ps at 20 K for a carrier density of $n_{2D} = 1\times10^{15}$ m^{-2} similar to these InSb heterostructures. This approximation is only valid at temperatures where $k_BT << E_F$, the fact that our structures are degenerately doped means this approximation holds well beyond room temperature. The dependency of τ_{e-e}^{-1} on E_F means that it is subject to the effects of non-parabolicity, substituting E_F into expression 2.12 gives a perturbation to E_F which decreases the scattering rate and increases the quantum lifetime even further emphasising how the limiting scattering mechanism cannot be due to $e-e$ effects.

4.2.1.2 Carrier density dependence of the quantum lifetime

Investigation of the quantum lifetime as a function of carrier density allows for variation of the Fermi energy while in principle keeping the effects of scattering mechanisms constant. Figure 4.12 shows the extracted quantum lifetimes of gated samples SF1055 & SF1056 as a function of carrier density extracted from a single carrier fit. The extracted lifetimes of both samples show a strong dependence on carrier density similar to that observed in the characteristic transport lifetime shown in figure 4.2 and consistent with observations in other material systems [60]. This is characteristic of enhanced screening of the scattering potential experienced by carriers in the 2DEG, as the charge density increases k_F increases $\propto n_{2D}^{1/2}$ this decreases the interaction time between carriers at the Fermi energy and the scattering potential.

In studies of high mobility ($\mu > 100\,\mathrm{m^2V^{-1}s^{-1}}$) GaAs/AlGaAs quantum wells the quantum lifetime has been observed to increase linearly with carrier densities below $1 \times 10^{15}\,\mathrm{m^{-2}}$ before reaching a plateau [66, 67]. They attribute this to enhanced screening before reaching limiting scattering from background impurities in the 2DEG. The absence of any plateau in this data would suggest that transport in these samples is limited by scattering from remote ionised impurities. This result is not surprising since the δ-plane is only 25 nm above the QW interface. In similar structures the carrier lifetime has been observed to increase with greater separation between the δ-plane and the QW [24]. The quantum lifetime of both samples appears to belong to a single limiting mechanism, this is counter-intuitive since the 2D impurity potential should be proportional to the dopant in the δ-plane and we would expect an increase in remote ionised impurity scattering for a greater dopant density. However, investigation of this mechanism using the transport model described in [24, 35] reveals that doubling the scattering potential only yields a $\sim 2\,\%$ decrease in the quantum lifetime, this is attributed to increased Thomas-Fermi screening of carriers in the quantum well.

A summary of the transport properties for studied samples is given in table 4.1. An important figure of merit for electrical transport in modulation doped heterostructures is the ratio between the transport and quantum lifetimes. A large ratio indicates that the most significant source of scattering is from long range potentials which do not adversely

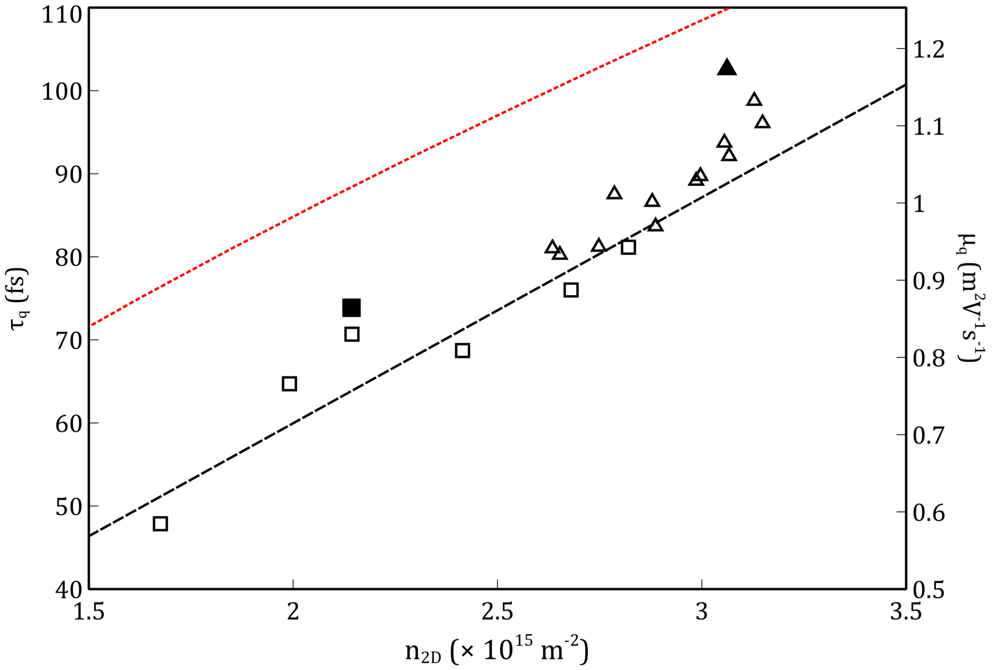

FIGURE 4.12: The extracted quantum lifetime and corresponding quantum mobility as a function of carrier density for samples SF1055 (triangles) & SF1056 (squares) at 3 *K*. The dashed fit line is a guide to indicate the upward trend in the data. Hollow markers indicate data taken from gated samples over a range of carrier densities while solid markers are measurements of ungated devices. The red dotted line is the predicted quantum lifetime from a relaxation time approximation model including the effects of remote ionised impurities, background impurities and non-parabolicity.

affect the conductivity, whereas small ratios indicate that the transport and quantum lifetimes are limited by similar mechanisms. It is noteworthy that the transport ratio for these heterostructures are all consistent with those reported by Hayes [34].

Figure 4.13 shows the behaviour of the lifetime ratio for these samples as a function of carrier density. The lower ratios of the gated samples are consistent with the reduced transport lifetime while the quantum lifetime remains largely unchanged. The presence of a dielectric layer clearly has a negative impact on the quality of the transport. To account for this in the transport model a second plane of defects was positioned at the surface 60 nm above the QW, with a density $\sim \times 10^{17}\,\mathrm{m}^{-3}$. Including this second plane of defects gives a closer agreement between the calculated transport ratios and those predicted from the transport model. The inclusion of a second plane of defects

Table 4.1: Summary table of the classical and quantum transport properties for two samples investigated. The range of lifetimes reveal an almost constant ratio between transport lifetimes.

Vg (V)	n ($\times 10^{15}/\,\mathrm{m}^2$)	μ (m^2/Vs)	τ (ps)	τ_q (fs)	τ/τ_q	Γ (meV)
			SF1055			
Ungated	3.06	23.5	1.87	93	20.0	2.3
-0.5	2.63	6.2	0.50	74	6.7	2.8
-0.4	2.79	8.7	0.69	80	8.7	2.6
-0.3	2.88	11.3	0.90	79	11.5	2.7
-0.2	2.99	13.1	1.04	81	12.9	2.6
0.0	3.07	14.1	1.12	84	13.4	2.5
0.1	3.13	14.5	1.15	90	12.8	2.3
0.1	3.15	14.3	1.14	87	13.1	2.4
0.0	3.06	14.2	1.13	85	13.3	2.5
-0.2	3.00	13.1	1.05	82	12.8	2.6
-0.3	2.89	11.3	0.90	76	11.9	2.8
-0.4	2.75	8.9	0.71	74	9.6	2.8
-0.5	2.65	6.2	0.49	73	6.8	2.9
			SF1056			
ungated	2.14	19.5	1.56	67	23.2	3.1
-0.4	1.68	9.0	0.72	44	16.5	4.8
-0.2	1.99	10.0	0.79	59	13.6	3.6
0.0	2.14	10.4	0.83	64	12.9	3.3
0.2	2.41	10.5	0.84	62	13.4	3.4
0.4	2.68	11.1	0.89	69	12.8	3.0
0.6	2.82	11.3	0.90	74	12.2	2.8

contributing to the overall scattering potential seen by carriers in the QW is not unrealistic, the presence of a dielectric creates interface traps which collect charge and could plausibly contribute to the overall scattering potential. The impurity density required to improve the fit of the model is similar to interface state densities reported throughout for the literature [68, 69]. Though work regarding interface quality between high κ dielectrics and antimonide ternaries is sparse, values reported for InGaAs which has a similar band gap to the top barrier AlInSb report defect densities ranging anywhere between $10^{15} - 10^{17}\,\mathrm{m}^{-2}\mathrm{eV}^{-1}$.

4.2.2 Estimation of the Landau level broadening

The observation of Shubnikov-de Haas oscillations at low fields is highly dependent upon the single particle broadening Γ, also known as the Landau level broadening parameter

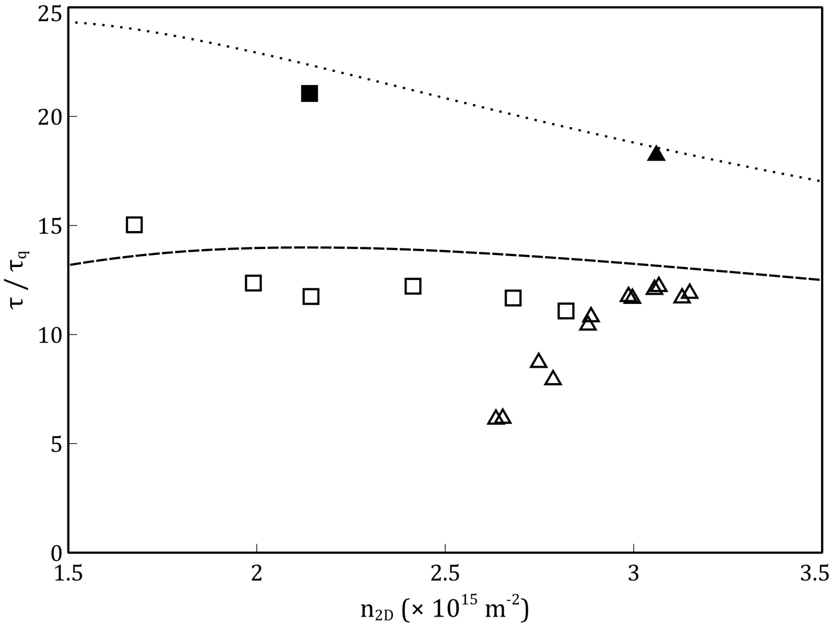

FIGURE 4.13: The transport and quantum lifetime ratio dependence on carrier density. The ungated samples (solid markers) have a distinctly higher ratio than the gated sample (hollow markers). The dotted line is the lifetime ratio predicted from the transport model with a single impurity with a density of $n_{2D} = 1 \times 10^{16}\, m^{-2}$ in the δ-plane. The dashed line shows the predicted lifetime ratio when a 2^{nd} plane of charged impurities with a density of $\sim 10^{17}\,\mathrm{m}^{-2}$ is included at the samples surface.

it dictates the minimum field required to separate Landau levels by more than the broadening Γ. Under the assumption that Γ is independent of temperate (a reasonable assumption since τ_q shows no obvious T dependence) a value can be determined by scrutiny of the longitudinal resistivity where oscillations become resolved, defined here as B_{SdH} and given by equation 4.19.

$$\Gamma = \frac{\hbar e B_{SdH}}{m^*}. \tag{4.19}$$

This method has some distinct disadvantages as the ability to discern where the onset of SdH starts is up to interpretation. Figure 4.14 shows ρ_{xx} and its corresponding second differential, though the oscillations are almost unobservable in the low field resistivity, in the second differential the oscillations are apparent to significantly lower fields. Determining this point is therefore highly dependent on data quality.

In agreement with the trend observed for the quantum lifetime the broadening parameter is observed to be highly dependent on carrier density as shown by figure 4.15 with values

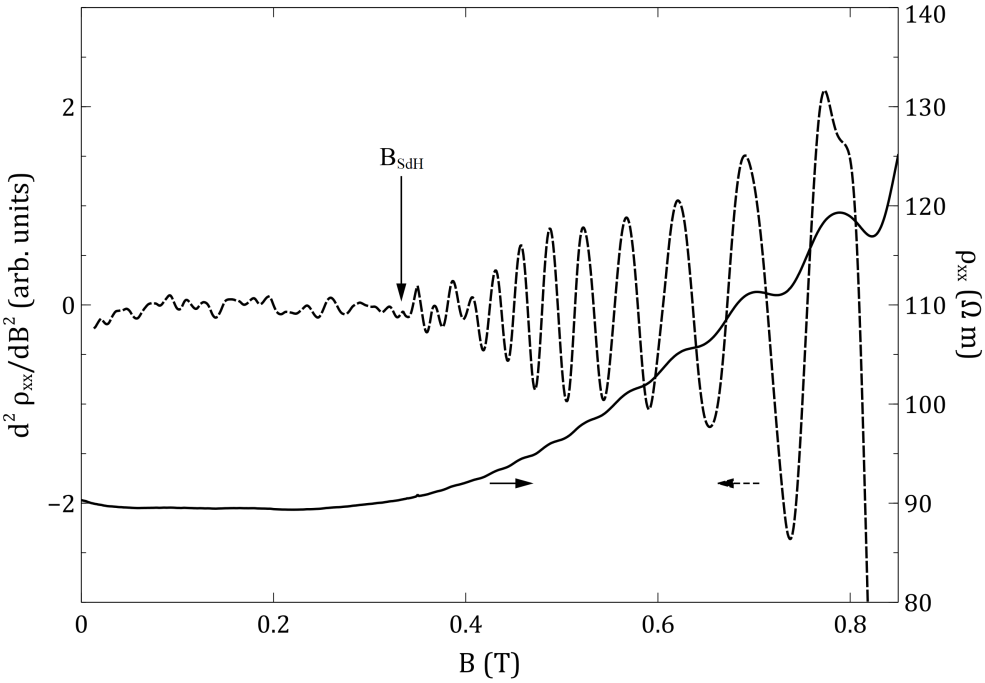

FIGURE 4.14: The low field longitudinal resistance of ungated sample SF1055 and the corresponding second differential. The onset of Shubnikov-de Haas oscillation are highlighted, this correspond to the point were oscillations are no longer periodic in $1/B$. The second differential highlights shows an apparent beat pattern with a non-zero beat amplitude, this phenomenon will be addressed in chapter 5.

ranging from $3-8$ meV, this is unsurprising since the broadening is dependent upon the quantum lifetime. It is also possible to estimate the broadening from the quantum lifetime itself [70] since the broadening is inversely proportional to the quantum lifetime as shown in equation 4.20.

$$\Gamma \propto \frac{\hbar}{\tau_q^{\gamma}}. \tag{4.20}$$

Here γ is highly dependent on the form of the scattering potential, in modulation doped heterostructures the scattering potentials are all long range and $\gamma \sim 1$ [70]. The values for Γ extracted here are consistent with values extracted in other narrow-gap material systems [21], though are somewhat surprising when compared to other high mobility materials [60, 67] which display almost an order of magntiude smaller broadening. The combination of large transport lifetimes and large single particle broadening suggest that the scattering process dominating the quantum lifetime does not limit the transport lifetime. This is consistent with evidence in other materials [66, 67] where the transport mobility is observed to increase long after a plateau in quantum lifetime is reached. This is the “smoking gun” indicating that the dominant scattering mechanism is from a long

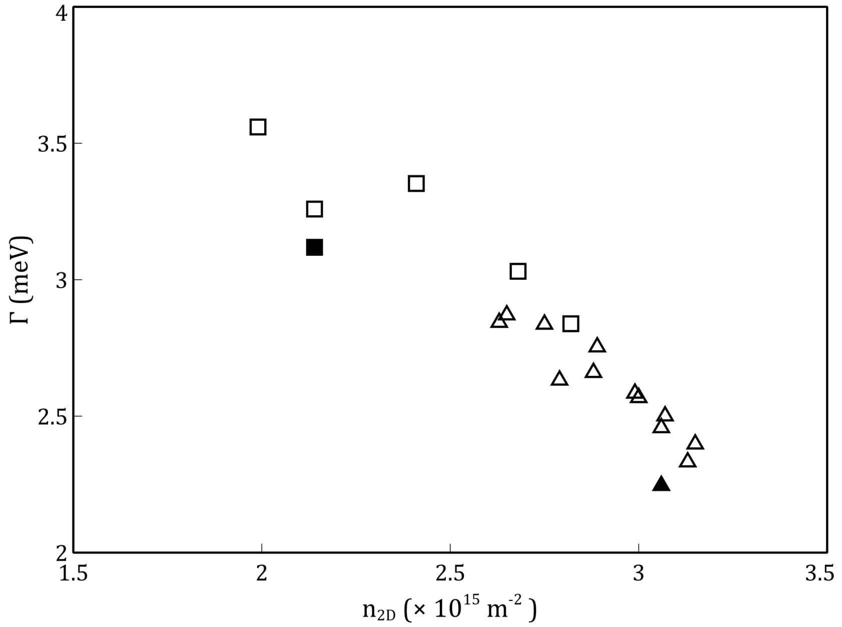

FIGURE 4.15: The broadening parameter Γ as a function of carrier density determined from the onset of SdH oscillations and calculated from the quantum lifetime.

range potential which is likely from the superposition of the scattering potential from surface charge trapped in the dielectric layer and from the δ-dopant layer.

4.3 Summary

Low and high field magnetotransport data have been presented in high quality InSb quantum wells for both gated and ungated samples. The effect of temperature on transport mechanisms has been discussed and it was highlighted that no significant temperature dependence was observed in either the classical transport lifetime below 30 K or the quantum lifetime before thermal broadening made observations of the quantum states impossible.

It was noted that the application of a gate dielectric severely degraded the classical transport quality of a heterostructure, while only a small degradation in the quantum transport was observed. Using a top gate electrode, the 2DEG potential was modulated to observe the effects of carrier concentration on transport properties. Both the classical and quantum transport were observed to be highly dependent on carrier density and the quantum lifetime of carriers was observed to vary between $50 - 100\,\mathrm{ps}$ over a carrier density range of $1.5 - 3.2 \times 10^{15}\,\mathrm{m}^{-2}$.

Using a transport lifetime model described by Orr et al. [24], close agreement between the observed ratio between classical and quantum lifetimes was achieved. The degradation in the quantum mobility with the application of gate dielectric was accounted for by the incorporation of a second plane of charge at the interface between the dielectric and the top barrier. A charge density of the order $\sim 10^{17}\,\mathrm{m}^{-2}$, consistent with defect densities observed in materials with similar bandgaps [69], was required to obtain good agreement between data and theory.

Chapter 5

Density of states modelling

5.1 Introduction

Modelling of the magnetoresistive behaviour in the quantum Hall regime might, at first glance, seem complex. However, an effective, simple model can be constructed by numerical calculation of the evolution of the density of states as a function of the magnetic field. The following model can be an informative tool in investigating the effect of changes to various parameters on the density of states. Comparison between the model and measured magnetoresistance data for these heterostrucures provides valuable insights, aiding the extraction of accurate material parameters.

Using properties for the Landau level broadening and the electron effective mass extracted in the previous chapter, alongside carrier densities extracted via fourier transformation of the SdH behaviour the number of free fitting parameters in the model is reduced. Improving the quality of fit between the observed magnetoresistance and the model can subsequently yield material information.

In section 5.2 the model is introduced and progressive layers of complexity such as band non-parabolicity are introduced observing the effects on the density of states. Section 5.3 addresses the inclusion of inversion asymmetry arising from the electric fields present within these materials and heterostructure designs predicted from Schrödinger-Poisson modelling. Comparisons between the modelled oscillations in the density of states at the Fermi energy and measurement are discussed in section 5.4.

5.2 Modelling Shubnikov-de Haas oscillations by conductivity

The physical principles responsible for the observation of Shubnikov-de Haas oscillations were discussed in the previous chapter, though for completeness a brief summary of the important principles will be restated here. The application of a magnetic field perpendicular to a transport plane forces charged particles to experience a Lorentz force and undergo cyclotronic motion. Solutions to the Schrödinger equation incorporating the magnetic vector potential take the form of a harmonic oscillator, a ladder of allowed states are formed known as Landau levels. Each Landau level consists of states for both spin up and spin down electron's, the degeneracy of which are lifted by the magnetic field due to the Zeeman interaction. The energy of each spin split Landau level is described by

$$E = \hbar\omega\left(N + \frac{1}{2}\right) \pm \frac{1}{2} g^* \mu_B B, \tag{5.1}$$

simply a reiteration of equation 4.13 including the Zeeman energy, while the Landau level degeneracy is given by 4.14. Both the energy of each Landau level and the degeneracy of levels are proportional to the applied magnetic field. Increasing the magnetic field decreases the number of Landau levels which exist below the Fermi energy while increasing the DOS. The oscillation in the DOS which exists at the Fermi energy is subsequently responsible for the modulation of the conductivity and observation of SdH oscillations.

A given spin split Landau level has an energy described by equation 5.1, the density of states can be approximated by a series of broadened Landau levels, each contributing a number of states determined by the level degeneracy at a certain field. The nature of this broadening has been suggested to take multiple forms such as Gaussian or Lorentzian profiles and its dependency on the magnetic field are contentious. A series of Gaussian broadened Landau levels as considered in [50] would create a DOS distribution described by equation 5.2,

$$g(E,B) = \frac{eB}{\pi\hbar}\frac{1}{\Gamma}\frac{1}{\sqrt{2\pi}}\sum_{N=0}^{\infty}\exp\left(-\frac{(E-E_N)^2}{2\Gamma^2}\right), \tag{5.2}$$

whereas a series of Landau levels with a Lorentzian broadening profile would be described by the equation

$$g(E,B) = \frac{eB}{\pi^2\hbar}\sum_{N=0}^{\infty}\frac{\frac{1}{2}\Gamma}{(E-E_N)^2-\left(\frac{1}{2}\Gamma\right)^2}. \tag{5.3}$$

The energy which contains sufficient states to accommodate all electrons in a material is the Fermi energy E_F, this can also be considered the minimum energy an electron would require to be added to the system. The carrier density of the material is assumed to be constant with magnetic field, hence, E_F can be calculated from the criteria

$$n_{2D} = \int_0^{E_F} g(E,B)\,dE \tag{5.4}$$

i.e. the Fermi energy is where the sum off all states below it is equal to the carrier density.

The longitudinal magnetoconductivity of a material can be calculated numerically from this simple expression using a method similar to that used by Englert *et al.* [50] while investigating the effective g-factor in a GaAs-AlGaAs system. At zero temperature, the longitudinal conductivity is proportional to the number of states available within the broadening width of the Fermi energy, each state contributing a unit of conductance and described by [50]

$$\sigma_{xx} = \frac{e^2}{2\pi\hbar}\int\frac{-d\,f(E,E_F)}{dE}\sum_{N=0}^{\infty}\left(N+\frac{1}{2}\right)\exp\left(\frac{-(E-E_N)^2}{\Gamma^2}\right)dE \tag{5.5}$$

where $f(E,E_F) = [\exp(E-E_F/k_BT)+1]^{-1}$ is the Fermi-Dirac distribution.

The tensor relation which describes the resistivity of a material is given by

$$\rho_{xx} = \frac{1}{\sigma_{xx}^2+\sigma_{xy}^2}\begin{pmatrix}\sigma_{xx} & \sigma_{xy}\\ \sigma_{yx} & \sigma_{yy}\end{pmatrix}. \tag{5.6}$$

Most models regard the transverse conductivity as the simple low field estimation of the Hall conductivity $\sigma_{xy} = -n_{2D}e/B$. Even at moderate fields where quantisation effects from the extended and confined states are only just discernible the model is sufficient as an estimation of the conductivity. At greater fields where the effects of the quantum Hall effect are more pronounced the validity of this estimation breaks down.

It is important to note from inspection of equation 5.5 that the longitudinal conductivity is proportional to the density of states at the Fermi energy. As such many important parameters can be extracted simply by considering the variation of the DOS at the Fermi energy, $g(E_F)$, as a function of field. Though this method does not provide resistivity values for direct numerical comparison with measurement it still clearly highlights the effects of parameter variation.

The following sections discuss the effects of varying parameters on the observed density of states at the Fermi energy. Unless otherwise stated the simulations were made using a Lorentzian broadening to the density of states with further parameters used summarised in table 5.1

Table 5.1: The default parameters used for modelling the DOS at the Fermi energy.

Parameter	Value
n_{2D}	$2.5 \times 10^{15}\,\mathrm{m}^{-2}$
m^*	$0.013\,\mathrm{m}_0$
Γ	$2.5\,\mathrm{meV}$
g^*	30

5.2.1 Modelling of high field magnetoresistance oscillations

Figure 5.1 compares the Fermi energy and corresponding DOS created by Landau levels with Gaussian and Lorentzian lineshapes. There is debate in the literature as to which broadening profile most accurately describes the Landau level [71–82]. Both broadening profiles show the amplitude of the DOS oscillation increases with magnetic field as expected due to the increasing degeneracy of states in each Landau level.

There are a number of interesting differences between the two broadening profiles. The Gaussian broadening has an oscillation amplitude larger than that of the Lorentzian broadening due to the higher concentration of states at the center of the Landau level. The spin split Landau levels are resolved at much lower fields with Lorentzian broadening whereas the Gaussian lineshape of the spin split Landau levels have already coalesced into a single broad peak. The implication of this is that for Gaussian broadening, a smaller value for Γ is required to discern spin split states at low field, where they are observable when considering Lorentzian broadening. The long tails of the Lorentzian lineshape ($\sim E^{-2}$) cause a smooth oscillation of the DOS at the Fermi energy while the Gaussian DOS oscillation appears to have discontinuous minima. This sharp discontinuity is also observed in the Fermi energy where it transitions abruptly between Landau levels compared with a more gradual transition from Lorentzian broadening.

The Landau level spectrum given by equation 4.13 is derived using a parabolic approximation for the energy dispersion for electrons in the conduction band. The effects of non-parabolicity on the Landau level energy spectrum in narrow-gap materials such as InAs and InSb has been investigated using a 4-band Kane model by Askenazy *et al.* [83]. Their approach is valid when the energies considered are significantly smaller than the spin split-off energy of the material, $E \ll \Delta$. InSb has one of the largest spin split-off energies of the III-V materials [15], 800 meV compared to 340 meV for GaAs and 110 meV for InP. All structures available for investigation had a Fermi energy $E_F < 100\,\text{meV}$, well within the region of validity for this approximation.

The increasing effective mass of carriers at higher energies causes the Landau levels to behave sub-linearly with magnetic field, subsequently resulting in a decrease in the energies of each Landau level. The non-parabolic dispersion of carriers increases the average DOS, which causes a reduction in the Fermi energy since more states exist per unit energy.

Figure 5.2 shows a comparison between parabolic and non-parabolic energy dispersions for both Lorentzian and Gaussian broadening profiles. The peaks in the DOS at high

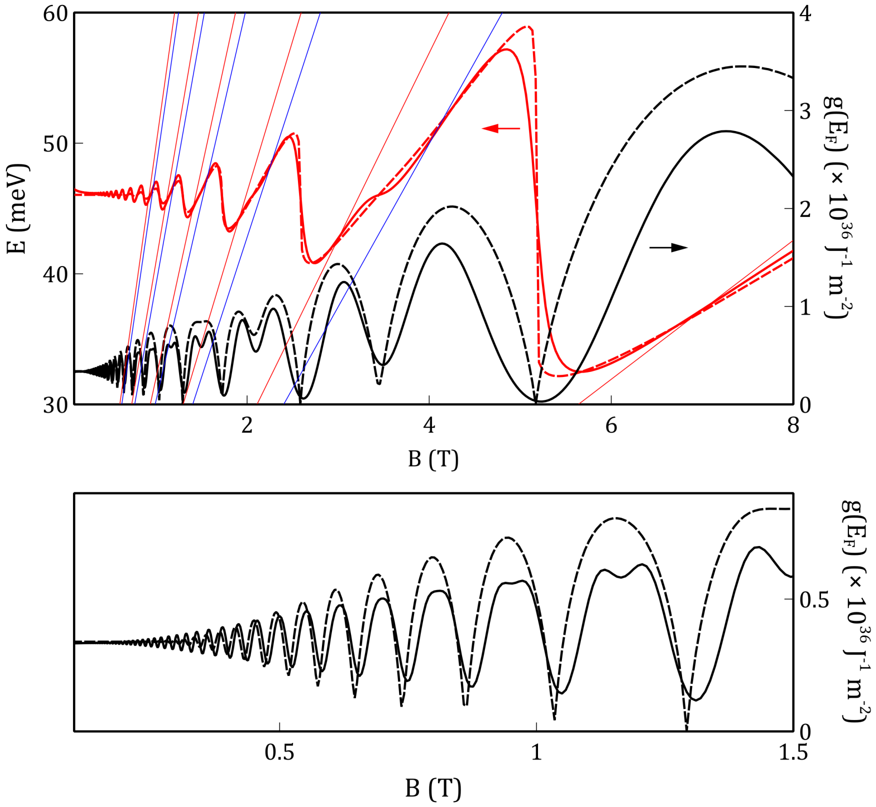

Figure 5.1: Magnetic field evolution of the Fermi energy (red) and DOS at the Fermi energy (black) for both Lorentzian (solid) and Gaussian (dashed) broadened lineshapes, the lower plot is zoomed in at lower fields. The energies of the first ten spin split Landau levels are plotted to highlight that a peak in the DOS occurs when a Landau level crosses the Fermi energy. A carrier density of $n_{2D} = 2.5 \times 10^{15}\,\mathrm{m}^{-2}$, effective mass $m^* = 0.013 m_0$, a LL broadening of $\Gamma = 2.5\,\mathrm{meV}$ and effective g-factor $g^* = 30$ were used in the calculation.

fields are unaffected by the introduction of non-parabolic effects, however, at low field the maxima in the non-parabolic DOS coincides with minima in the parabolic calculation for both Gaussian and Lorentzian broadening. This occurs because the non-linearity of the Landau level energy spectrum in the non-parabolic case leads to decreasing energy separation between Landau levels $\Delta E_{N,N+1} \propto 1/N$. This introduces a degeneracy between the high and low energy spin states of different Landau levels at certain fields. Observation of this effect would be highly dependent on the single particle broadening, carrier density and g-factor of the system.

As described in the previous chapter, the frequency of Shubnikov-de Haas oscillations is defined by the carrier density of the material and oscillations are periodic in $1/B$. A

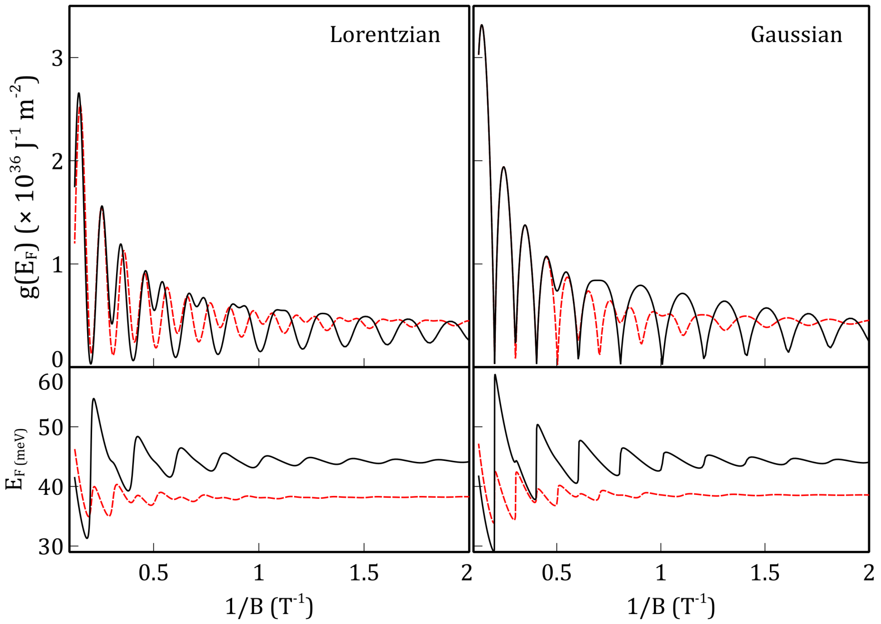

FIGURE 5.2: Comparison between both Lorentzian and Gaussian broadening types in both the parabolic (black) and non-parabolic (red) approximations for the Landau level energies. (Top) The DOS at the Fermi energy (Bottom) as a function of field. A carrier density of $n_{2D} = 2.5 \times 10^{15}\,\mathrm{m}^{-2}$, effective g-factor of $g^* = 30$ and broadening of $\Gamma = 2.5\,\mathrm{meV}$ were used in the simulation.

spin degenerate system will oscillate with a single frequency proportional to the carrier density, described by equation 4.16 [84]. A Fourier transform of a spin degenerate oscillation will yield a single large peak and harmonics of diminishing amplitude. Figure 5.3 shows the DOS oscillation and associated Fourier transform for spin-split DOS oscillations with different carrier densities. The Fourier transform of an oscillation including spin splitting introduces a higher frequency peak which is twice the fundamental frequency, hence, when analysing the Fourier transform of a non spin-degenerate oscillation the factor of 2 in equation 4.16 must be removed.

The ability to accurately estimate the carrier density through the use of a Fourier transform is sensitive to the number of oscillations sampled in a given field region. Lower carrier density samples yield fewer oscillations at energies high enough to resolve individual Landau levels, broadening the frequency response and decreasing the amplitude of the Fourier transform. In very high mobility GaAs heterostructures with similar carrier densities [67], resistivity oscillations have been resolved at fields as low as 15 mT due to the long quantum lifetimes and subsequently small Landau level broadening ($\Gamma \sim 20\,\mu\mathrm{eV}$). The relatively large broadening of the heterostructures studied in this

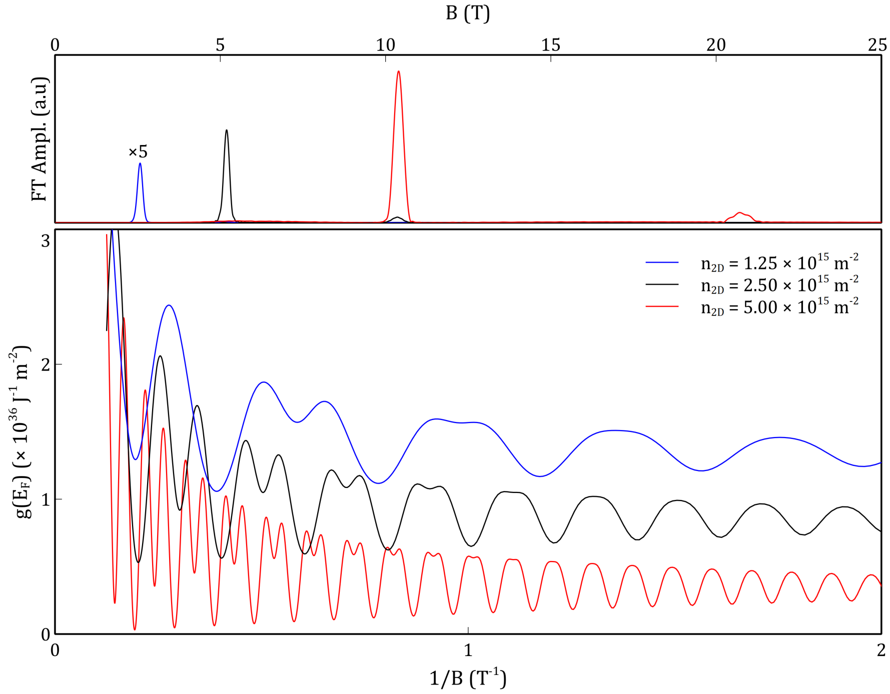

Figure 5.3: (Bottom) A calculation of the DOS at the Fermi energy as a function of magnetic field at different carrier densities. The periodicity of the DOS oscillations are highly carrier density dependent as shown by the Fourier transform plot above. (Top) The corresponding Fourier transform of each oscillation, the amplitude of the FT peak typically increases with carrier density due to a greater number of oscillations being sampled within a given field region.

thesis yield resolvable Landau levels at fields as low as $\sim 300\,\text{mT}$, significantly reducing the number of observable oscillations when compared with higher quality samples. This is clearly emphasised in figure 5.4 where the effects of variation in Γ are modelled using values similar to those extracted in the previous chapter. This comparison highlights that for a given material, the quantity of observed Shibnikov-de Haas oscillations is a consequence of both the carrier density and the transport qualities of the system.

A variety of DOS oscillations calculated using different values of the effective g-factor are shown in figure 5.5. As expected the onset of spin resolved oscillations occurs at lower fields in simulations with a larger value for g^*. The large effective g-factor of InSb means that even though the transport qualities of these heterostructures are comparable to those of similar GaAs/AlGaAs heterostructures in 1980 [85], the effects of spin splitting can be resolved at relatively low fields. By comparison, a GaAs heterostructure with $|g^*| = 0.44$ [15] and an equivalent broadening would not show spin split oscillations until $B \sim 100\,\text{T}$. The amplitude of oscillation decreases at larger g-factors since there is less

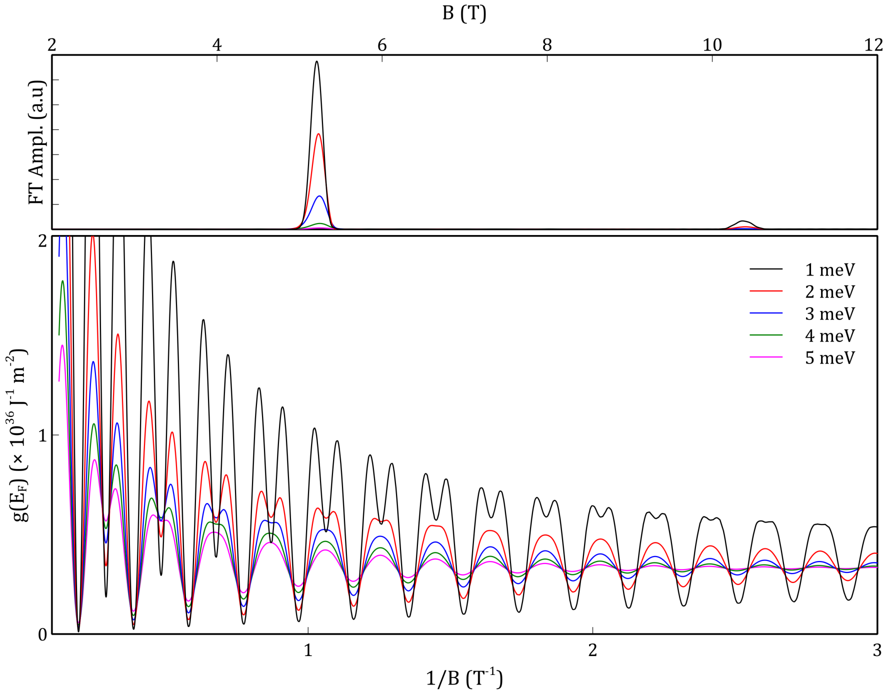

Figure 5.4: Investigation of the effects of variation in broadening parameter Γ as a function of magnetic field. Smaller broadening results in larger DOS oscillations and spin split peaks being resolved at lower magnetic fields. The broadening has no obvious effect on the FT peak position, though clearly affects the amplitude.

overlap between the DOS of the spin split energies. Changing the sign of g^* has no effect on the observed DOS oscillation since the spin states are assumed to have equal broadening, this assumption will be explored further later in the chapter.

Analysis of the field where a peak in oscillation occurs against peak number reveals a gradient change when spin split states are no longer resolved. A method commonly used for estimating the strength of a materials effective g-factor is to compare this field and the field where SdH oscillations become observable [86]. These fields are where the Landau level separation $\hbar\omega$ and the separation between spin states $g^*\mu_B B$ become comparable to Γ. This allows a simple expression for g^* to be inferred,

$$g^* = \frac{\hbar e}{\mu_B m^*}\frac{B_1}{B_2} \tag{5.7}$$

where B_1 is the field where SdH oscillations become observable and B_2 the field where spin splitting is resolved.

This provides a good estimate for the magnitude of g^* but has significant disadvantages

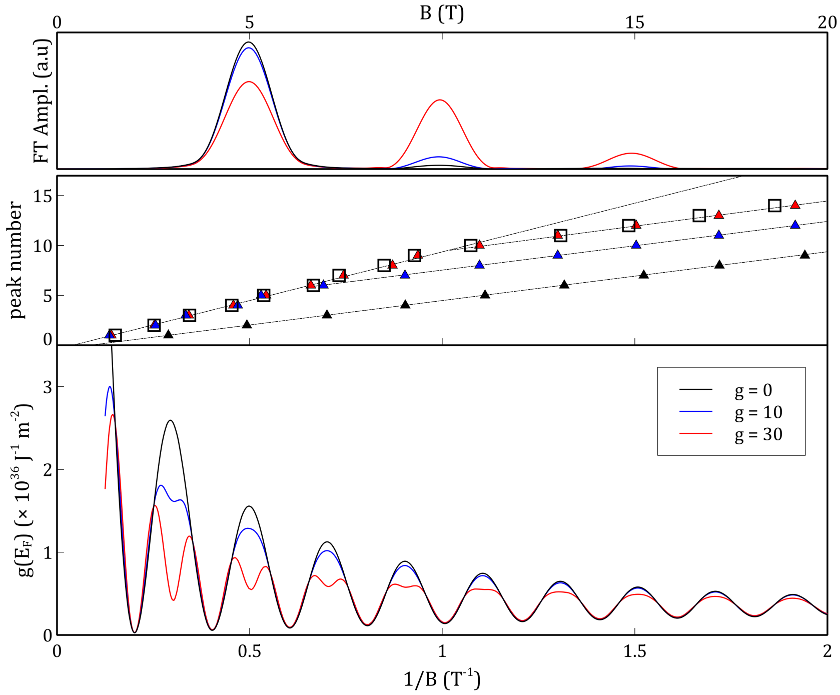

FIGURE 5.5: (Bottom) A plot comparing the effects of different g-factors on the observed DOS at the Fermi energy. (Middle) A plot of the peak number against peak field for the calculated DOS (triangles), compared to actual data (squares) from sample SF0968 with similar carrier density. The field at which the gradient turnover occurs is dependent upon the g-factor of the material and the broadening of the Landau levels. (Top) The calculated FT of the different oscillations.

compared to more elegant methods such as tilted field or optical injection measurements [87–89]. Electrically the two spin states are indistinguishable and equally contribute to conduction, hence no information about the sign of g^* can be extracted. This drawback is also encountered in tilted field measurements. A more visible downside is the fact that it requires the estimation of the onset fields and this is highly dependent upon quality of data. Most fundamentally it assumes that the Landau level broadening is independent of magnetic field, which is debated in the literature. Some authors suggest the broadening is independent of field, while others report a $B^{-1/2}$ dependency. Theoretically it has been suggested that the broadening changes from being field dependent to independent depending on the the magnetic length of the occupied Landau levels and the average disorder separation in the structure [90, 91].

5.3 The effects of inversion asymmetry on density of states oscillations

When the potential through which an electron moves within a quantum well lacks a valid center for an inversion transformation it is said to be *inversion asymmetric*. Under this condition the spin degeneracy of states is lifted even when no magnetic field is applied, this results in electrons in the conduction band with the same spin having different energies dependent upon the direction they are travelling i.e.

$$E_{\uparrow}(k) \neq E_{\uparrow}(-k) \tag{5.8}$$

with $E_{\uparrow}$ representing the energy of a single spin state. This is a manifestation of relativistic effects of electromagnetic fields on charged particles.

Bulk Inversion Asymmetry

The zincblende crystal is one such structure which lacks a center of inversion, resulting in most III-V compounds having some form of zero-field spin splitting. This inversion asymmetry is known as *bulk inversion asymmetry* and results from the microscopic potential of the zincblende unit cell being non-zero. This type of inversion asymmetry in bulk crystals was first described by Dresselhaus [92], who showed that the spin-splitting between conduction band states was proportional to $\boldsymbol{k}^3$ and defines the material parameter $\gamma\,[\mathrm{eVm}^3]$ known as the *cubic Dresselhaus* term. As the crystal potential is dependent upon the direction of carrier motion in the crystal, the magnitude of the spin-splitting is highly anisotropic. The maximum splitting is observed along the [110] direction, with zero splitting along both the [100] and [111] directions.

The strength of the Dresselhaus splitting is expected to increase for narrow-gap materials with large spin-orbit gaps [93] such as InSb. Estimation of γ for different materials can be made using band parameters, and for InSb is expected to be $\gamma_{InSb} = 760.1\,\mathrm{eV\AA}^3$ compared with GaAs which is predicted to have $\gamma_{GaAs} = 27.6\,\mathrm{eV\AA}^3$ [93, 94]. The values for γ for bulk InSb predicted throughout the literature vary somewhat [93, 95–97] but all anticipate values $\gamma > 200\,\mathrm{eV\AA^3}$. These discrepancies arise from uncertainties in the parameters of the theoretical models used to calculate them.

The confinement of electrons in a quantum well and subsequent quantisation of k_z was shown by Eppenga and Shuurmans [98] to separate the Dresselhaus splitting into two contributions, the k-cubic term and a further k-linear term ($\beta\,[\mathrm{eVm}]$). An estimation for β for wide wells can be given in terms of the bulk value γ,

$$\beta \approx \gamma \left(\frac{\pi}{W}\right)^2 \tag{5.9}$$

where W is the width of the well. For 30 nm quantum wells studied here this is a reasonable approximation, but for narrower wells the W^{-2} dependence leads to significant overestimation of β when more sophisticated models are considered [36].

It has been asserted that the contribution to spin splitting from the Dresselhaus term in quantum well heterostructures is insignificant and can be neglected in most material systems [99, 100]. Though recent work in InSb claims that the contribution from the Dresselhaus term can be a significant source of spin splitting in narrow quantum well heterostructures [36], for the purposes of this model the effects of bulk inversion asymmetry are not included.

Structural Inversion Asymmetry

The other primary source of inversion asymmetry in a quantum well is from the presence of any built-in electric field due to the band structure of the heterostructure interface. Since this phenomenon is dependent upon the arrangement of the heterostructure it is known as *structural inversion asymmetry*. A built-in electric field introduces another source of spin splitting known as *Rashba spin splitting*, which is linear in $\boldsymbol{k}$ and characterised by the Rashba coefficient $\alpha\,[\mathrm{eVm}]$. The Rashba coefficient is proportional to the strength of the electric field and can be (naively) described by the equation [93],

$$\alpha = \alpha_0 \langle E_z \rangle \tag{5.10}$$

where α_0 [eVm^2] is a material constant dependent upon band structure parameters and $\langle E_z \rangle$ is the expectation value of the built-in electric field for electrons in the conduction band. This model was shown by Pfeffer and Zawadski [100] to be an oversimplification and the measured Rashba parameter cannot be directly related to the electric field, though it provides a useful estimation for α in terms of the α_0, which has been discussed extensively throughout the literature. Using Kane model parameters, Winkler [93] predicts InSb to have $\alpha_0 = 523\,\mathrm{eV\AA^2}$ compared to $\alpha_0 = 117\,\mathrm{eV\AA^2}$ for InAs and $\alpha_0 = 5\,\mathrm{eV\AA^2}$ for GaAs. The large value for InSb highlights how sensitive the spin splitting is to the electric field, small potential variations such as those provided by electrostatic gating can result in easily observable changes in the splitting. This large spin orbit interaction is the primary reason InSb has received attention with regards to spintronic applications [101, 102].

The Hamiltonian describing the strength of the Rashba interaction is given by [93],

$$H_R = \alpha_0 \boldsymbol{\sigma} \cdot \boldsymbol{k} \times \boldsymbol{E} \tag{5.11}$$

where $\boldsymbol{\sigma}$ are the Pauli spin matrices, $\boldsymbol{k}$ is the in-plane wave vector and $\boldsymbol{E}$ is the built-in electric field in the heterostructure. Applied to a quantum well with growth in the z-direction and considering only the electric field out of plane, equation 5.11 can be reduced to

$$H_R = \alpha(k_x \sigma_y - k_y \sigma_x) \tag{5.12}$$

which has the familiar solution

$$E_{\uparrow\downarrow}(k) = \frac{\hbar^2 k^2}{2m^*} \pm \alpha k, \tag{5.13}$$

leading directly to the linear spin splitting $\Delta E = 2\alpha k$, where $k = \sqrt{k_x^2 + k_y^2}$. The dispersion relation arising from the inclusion of the Rashba interaction is shown in figure 5.6. A striking feature of Rashba spin splitting is that the dispersion relation for the two spin states are horizontally offset in k and degenerate at $k = 0\,\mathrm{m^{-1}}$ unlike Zeeman split states which have an equal energy separation at all k.

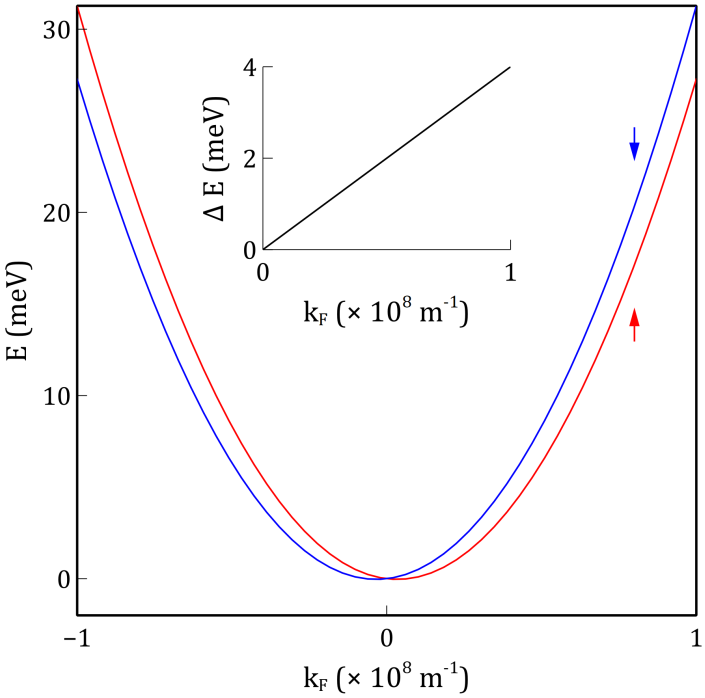

Figure 5.6: The 1D parabolic dispersion relation for electrons in the conduction band including the effects of the Rashba interaction. The inset shows the linear energy separation of the two spin states for the parabolic approximation. A Rashba parameter of $\alpha = 2\,\mathrm{eV\AA}$was used for the calculation.

It is more common to restate the Rashba and Zeeman interactions in the form of a precession vector from an effective magnetic field

$$\boldsymbol{\Omega}(k_{||}) = \frac{1}{\hbar}\begin{pmatrix} \alpha k_y \\ -\alpha k_x \\ \frac{1}{2}g^*\mu_B B \end{pmatrix}. \tag{5.14}$$

This vector defines a k-dependent rate of precession which is determined by the material parameters governing the spin orbit interaction within the material. The implications of this for a system dominated by diffusive transport is that any spin polarisation will relax due to the randomisation of wave vectors during momentum scattering events. Known as D'yakonov-Perel spin relaxation [103], the rate at which a spin polarised current decoheres depends upon the precession rates of individual particles about the effective field.

To include the effects of structural inversion asymmetry in the model the equation for the Landau level energies needs to include contributions from both the Zeeman term and the k-dependent Rashba term. The equation for the Landau level energy is then

$$E = \hbar\omega\left(N + \frac{1}{2}\right) \pm \hbar|\mathbf{\Omega}| \tag{5.15}$$

where $|\mathbf{\Omega}| = \frac{1}{\hbar}\sqrt{\alpha^2 k^2 + \frac{1}{4}g^{*2}\mu_B^2 B^2}$. Using the parabolic approximation we can substitute the expression for $k^2 = 2m^*E/\hbar^2$ with E being the energy of the Landau level, giving $k^2 = 2eB/\hbar\,(N + 1/2)$. Substitution of these back into equation 5.15 leaves

$$E = \hbar\omega \pm \sqrt{\frac{2\alpha^2 eB}{\hbar}\left(N + \frac{1}{2}\right) + \frac{1}{4}g^{*2}\mu_B^2 B^2}, \tag{5.16}$$

which is functionally equivalent to the form used in [93]. The implications of including the Rashba term in the Landau level energy spectrum can be seen in figure 5.7. Low energy Landau levels with small k display the characteristic Rashba dispersion by being degenerate at $E = 0$. Lou *et al.* [86] considered the effects of both a constant and an energy dependent splitting, the constant splitting was found to display all of the pertinent features created by the energy dependent splitting but the oscillations are shifted in B. They found excellent agreement between the measured SdH oscillations for an InAs/GaSb quantum well and the oscillations predicted by a Landau level spectrum including an energy dependent spin slitting.

Spin splitting necessarily introduces a net spin population due to the unequal density of states below the Fermi energy, the relative proportion of carriers in each spin states being proportional to the amount of spin splitting present in the system. The carrier density of a system has already been shown to dictate the frequency of oscillation in the DOS, with the individual spin split Landau levels giving rise to oscillations with frequencies determined by the relative populations of the two spin states. In the limit that the spin splitting is larger than the Fermi energy (for example a very low density sample) a single set of oscillations would be observed and a completely polarised spin population would exist since only one set of spin states are occupied. The Fermi energy in these structures is considerably larger than the magnitude of the spin splitting hence the frequency of oscillation for the two spin states will be comparable, oscillations created by multiple similar frequencies display beating patterns with the beat frequency being dependent on

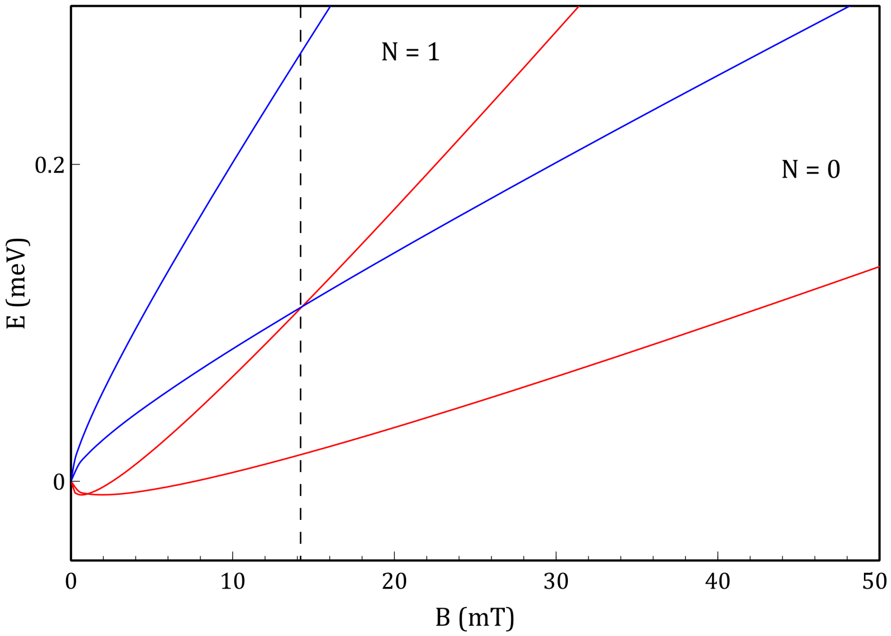

Figure 5.7: The spin splitting due to the Rashba interaction of the first two Landau levels as a function of magnetic field. At very low fields the energies are highly non-linear and degenerate at $B = 0\,\mathrm{T}$. The vertical dashed line shows the point of a Landau level crossing, a distinct feature of zero-field spin splitting.

the difference between the individual frequencies. The frequencies of these can still be extracted by Fourier transform if sufficient beat oscillations are observed and will yield two narrowly separated peaks. Engels *et al.* [104] derived a simple density of states correction which included the effects of spin splitting and formulated an expression to determine α from the relative carrier densities of the two spin states and is given by the equation

$$\alpha = \frac{\Delta n_{2D}\hbar^2}{m^*}\sqrt{\frac{\pi}{2(n_{2D} - \Delta n_{2D})}}, \tag{5.17}$$

Δn_{2D} being the relative difference in carrier densities of the two spin states determined by the separation of the two frequency components. This expression was derived neglecting the effects of any Dresselhaus contribution to the spin splitting, though is a good method for extracting the magnitude of the total spin splitting of a system from the Fourier transform.

The beating effects observed from spin orbit coupling have been investigated extensively in many material systems [21, 36, 86, 104–118] , generally with narrower wells and significantly greater carrier densities than those investigated here in order to maximise the spin splitting in the system. Surprisingly, compared to materials such as InAs and

InGaAs [21, 86, 104, 105, 107–116, 118] InSb has received relatively little attention [23, 36, 101] due to growth and processing challenges in creating high mobility samples with small broadening comparable to those found in other materials.

The effects due to a variation in α are shown in figure 5.8. As expected, beating patterns present themselves clearly in the oscillation in the density of states. The number of beat nodes observed in the data is found to be proportional to the strength of the spin splitting which is in good agreement with results expected from theory [86] and observations [21, 36]. Increasing the strength of the spin orbit coefficient has a curious effect on the phase of certain peaks in the density of states oscillation, introducing a change of phase of the oscillation.This change of phase occurs due to the degeneracy of different spin states between two different Landau levels, where an absence of states would be anticipated when not considering spin orbit interaction. An example of this can be observed at $B \approx 14\,\mathrm{mT}$, indicated in figure 5.7 by the dashed vertical line. Subsequently the amplitude of oscillations and peak locations can be modulated by the strength of the g-factor of the material, though this does not affect the position of the nodes as these are purely a consequence of the relative spin populations. The Fourier transform of the oscillations yield the expected twin peak response with a peak separation proportional to the strength of the spin splitting.

The small effective mass of InSb in conjunction with the large broadening means that even moderate carrier density samples often yield only one or two beat nodes. This means that more sophisticated methods of estimating the spin splitting are not practicable. In samples where multiple nodes are observed, Das *et al.* [119] proposed that an estimate of the spin splitting can be made through analysis of the node minima. The node frequency is directly related to the spin splitting and scrutiny of the node position in $1/B$ gives a direct estimate for the spin splitting.

The simulations modelled here consider purely the oscillations arising from the occupation of the spin states of a single subband, though beating patterns may also arise due to the effects of magneto inter-subband (MIS) scattering [120–123], where carriers may scatter elastically between subbands. The primary experimental method for determining whether oscillations are due to MIS scattering is to analyse the temperature dependence

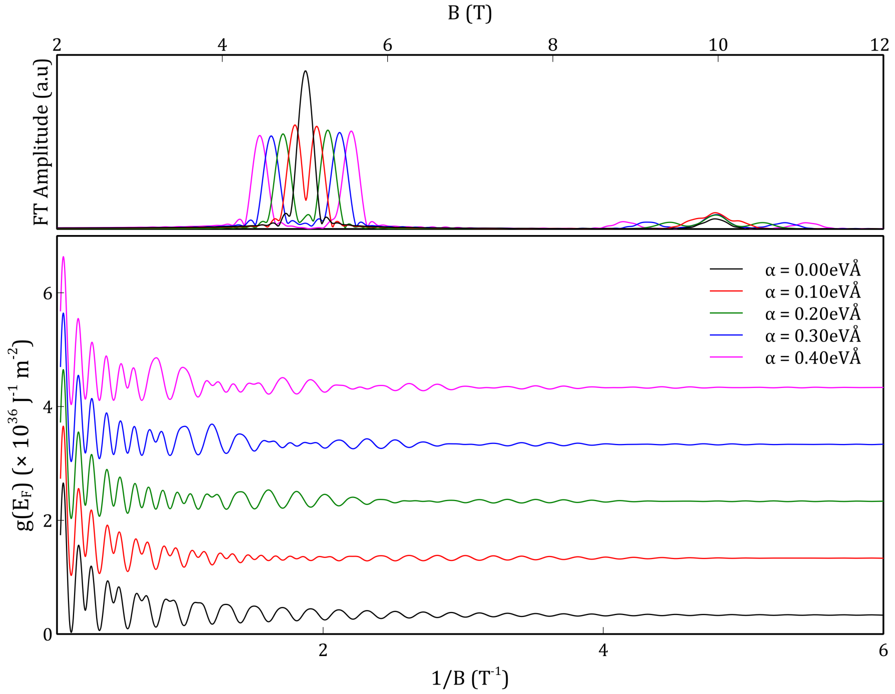

Figure 5.8: Investigation of the effects of variation of the Rashba coupling strength α as a function of magnetic field. The frequency of the beat oscillations is determined by the magnitude of the spin-orbit coupling parameter. An large Rashba parameter is associated with significant separation between the peak frequencies in the Fourier transform.

of the oscillations, which are relatively insensitive to temperature when compared with the heavily thermally damped oscillations in the density of states as discussed in the previous chapter.

The concept of a single particle broadening time, introduced in the previous chapter, arising from a single period oscillation in the density of states subsequently stumbles with the introduction of spin splitting to the density of states. The observed Shubnikov-de Haas oscillations behave with an amplitude proportional to

$$\Delta R \propto \exp\left(\frac{-\pi}{\omega\tau_q}\right). \tag{5.18}$$

This oscillation is no longer created by a single frequency but has a complex form bringing into question the interpretation of both spin states being characterised by the same amount of broadening when they have different carrier densities and thus different oscillation frequencies. The concept of spin dependent broadening mechanisms has been discussed by various authors [36, 86], the primary experimental evidence for spin dependent broadening is by investigation of the amplitude of beat nodes in the beating patterns observed in the oscillation of the density of states. If the two spin states have an equal amount of broadening the point where their oscillations are π radians out of phase would have zero amplitude. If these amplitudes were unequal then a beat node would have a finite amplitude. Experimental evidence for this phenomenon has been observed in InSb, InAs and InGaAs systems [36, 86, 113] all of which have significant spin orbit coupling interactions.

Figure 5.9 shows the effects of unequal Landau level broadening on the observed density of state oscillation at the Fermi energy. Any inequality in the magnitude of the broadening materialises as a considerable asymmetry in the amplitude of the Fourier transform of the density of states oscillation. Larger broadening results in a suppression of the FT amplitude for that spin state. Peaks in the density of states resulting from a spin state with a larger broadening have diminished amplitude, thus the presence of unequal scattering may also become apparent in resistivity data as a significant suppression of peak amplitudes in addition to the beat amplitude modulation caused by the spin orbit interaction.

5.4 Comparison between model and measured data

Having discussed some of the mechanisms affecting the Landau level energy spectrum in InSb and how these manifest as periodic oscillations in the density of states at the Fermi energy, it is pertinent to compare the model to observed Shubnikov-de Haas oscillations. The following discussion attempts to extract realistic values for some of the heterostructure parameters in order to confirm whether, by simply considering the density of states at the Fermi energy, a realistic agreement between observed and measured oscillation can be achieved.

A typical example of Shubnikov-de Haas oscillations for these structures is shown in figure 5.10, the raw data shows no clear beating effects consistent with reports for similar structures reported in the literature [36, 55]. The second differential of the resistivity data with respect to magnetic field shows a clear beat oscillation consistent with the

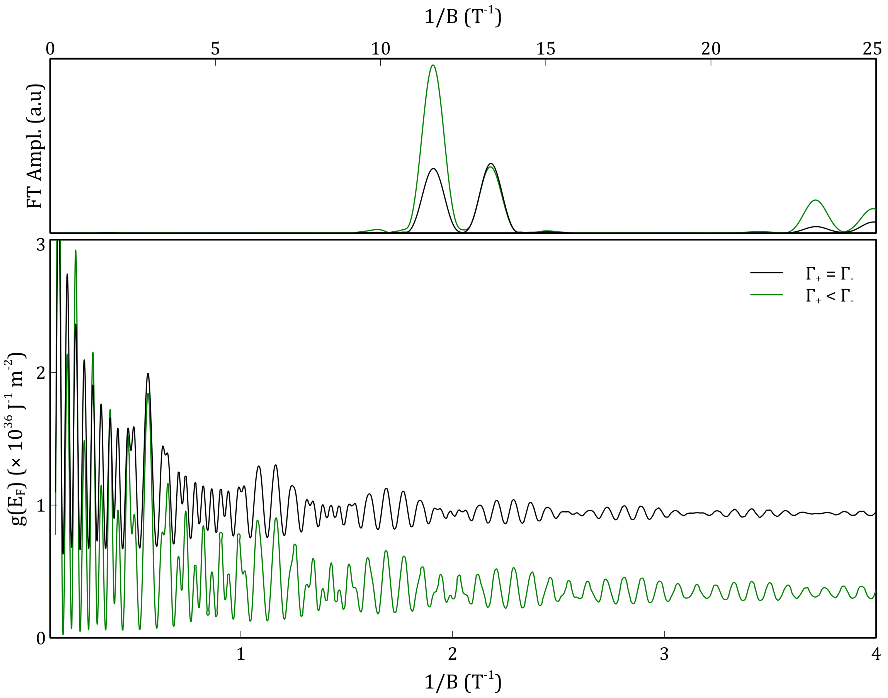

Figure 5.9: A comparison between the density of states at the Fermi energy created by Landau levels with both equivalent and unequal broadening. While peak positions remain unchanged the peaks corresponding to the spin state with larger broadening have a smaller amplitude. The presence of unequal broadening also causes the oscillation amplitude at a beat node to increase significantly. A carrier density of $n_{2D} = 6.0 \times 10^{15}\,\mathrm{m}^{-2}$ was used in the simulation to increase the number of oscillations between nodes to emphasise the non-zero amplitude.

formalism described above. The second differential was interpreted as the gradient of a linear fit to m neighbouring points at each field. The quality of the second differential is highly susceptible to the size of m and the resolution of the measured data. It is worth noting that most samples (including all gated structures) measured did not display an observable beating pattern, this is attributed to large Landau level broadening.

Estimation of the spin splitting in a number of samples with different carrier densities is shown in figure 5.11. All samples yield values for the spin splitting around 0.14 eVÅ displaying a clearly linear trend with increasing carrier density, this is consistent with reports from similar samples in the literature [36]. The increasing strength of the spin splitting with increasing carrier density can be attributed to the increased asymmetry of the quantum well in samples with greater doping. The larger transfer of charge causes an increase in the magnitude of the built-in electric field and a corresponding increase in the Rashba spin splitting. Interestingly, for samples which have a dopant plane below the 2DEG the observed variation of spin splitting with carrier density is the reverse of

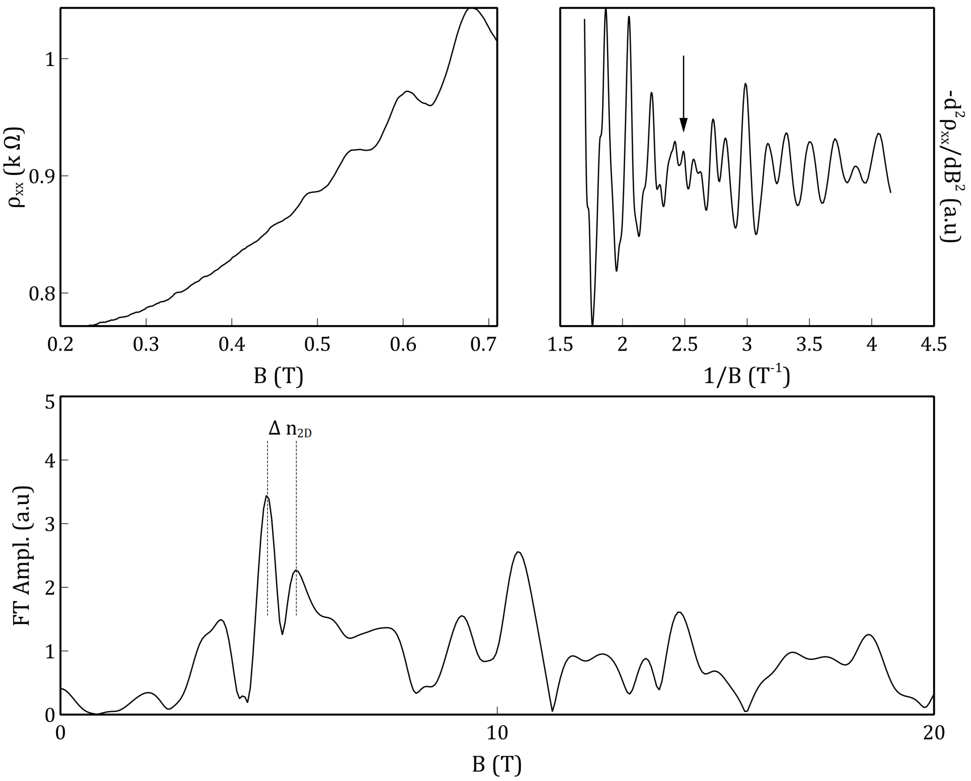

FIGURE 5.10: The measured Shubnikov-de Haas oscillations for ungated sample SF0968. Though no beating effects are obvious from the raw data, inspection of the second differential shows a clear beat node. The Fourier transform of the second differential is shown and the spin split nodes are highlighted.

that observed here [104, 124]. The error bars shown in figure 5.11 were determined by the variation in Fourier transform peak position when performed over different magnetic field ranges.

Using values for the carrier density and spin splitting extracted from the Fourier transform of the data, a more direct comparison between the oscillations observed in the density of states at the Fermi energy and the Shubnikov-de Haas oscillations may be made. The second differential of the resistivity is compared to the predicted density of states oscillations from parabolic and non-parabolic simulations in figure 5.12, the second differential is used for comparison due to the enhanced oscillations at low field.

Remarkable agreement between the peak positions of the data and those predicted using the non-parabolic energy spectrum are achieved using the predicted parameters. The number of oscillations between beat nodes and the node locations are also in good agreement at low field. Perhaps unsurprisingly the parabolic simulation fails to give any kind of agreement between beating effects and node locations, for the same spin splitting

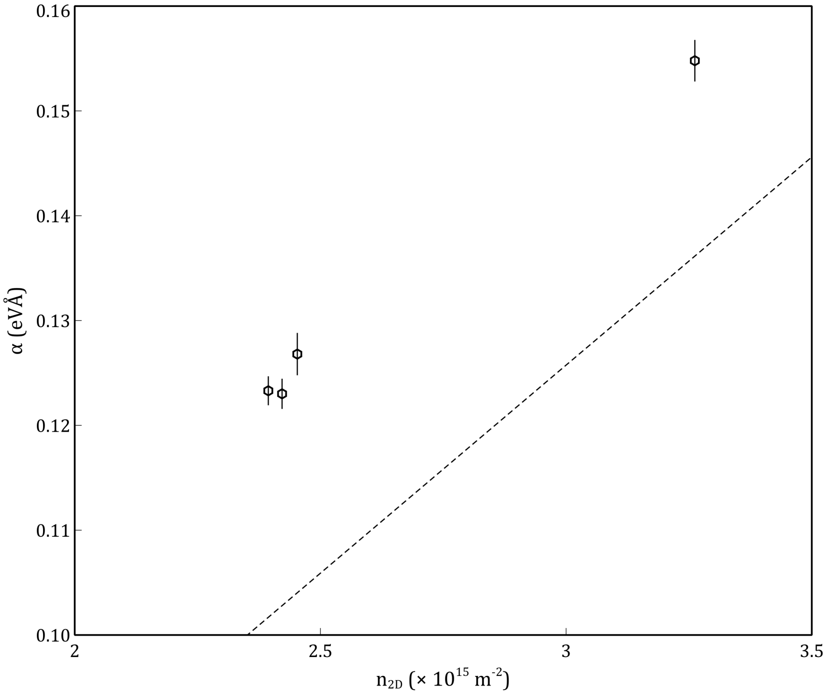

FIGURE 5.11: The extracted spin splitting from Fourier transform data for samples SF0963, SF0968, SF1056 and SF1055. The samples SF0963, SF0968, SF1056 intentionally have significantly lower doping than sample SF1055. The dashed line shows the expected strength of spin splitting predicted by equation 5.10 using the parameter for α_0 quoted in [93]. The strength of the electric field in the heterostructure was determined by Schrödinger-Poisson modelling.

twice the number of oscillations are observed between nodes when compared to the data. The non-parabolic oscillation predicts another node position above 0.5 T, this node does not materialise in the data and may be evidence for field dependent broadening of the Landau levels [57], where the broadening is dependent upon the length scale of each Landau level given by [58]

$$\ell_N = \sqrt{\frac{\hbar(2N+1)}{eB}}. \tag{5.19}$$

Evidence for this phenomenon being present in these structures is presented in chapter 6.

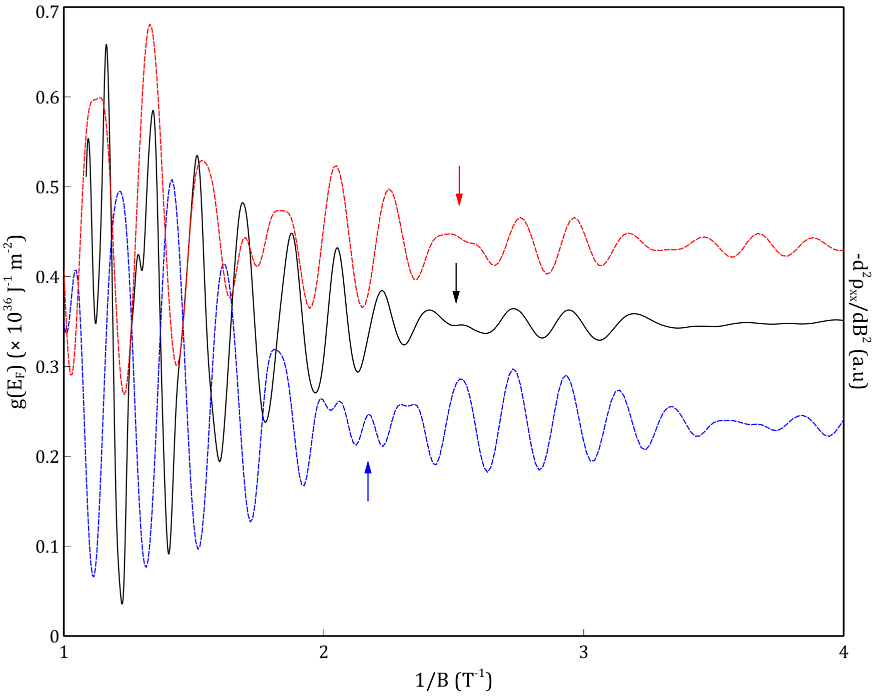

FIGURE 5.12: A comparison between the second differential of the resistivity data for SF0968 (black) and the predicted oscillation in the density of states using both the parabolic (blue) and non-parabolic (red) simulations. The value for α used in the simulation was 0.124 eVÅ with a carrier density of $2.39 \times 10^{15}\,\mathrm{m}^{-2}$. The density of states oscillations have been offset to improve the clarity of the comparison.

5.5 Summary

Numerical simulations of the variation in the density of states at the Fermi energy have been performed to demonstrate the effects that different parameters have on observed oscillations. A comparison between Gaussian and Lorentzian broadening models have been made. For a given level broadening, a Gaussian broadening profile was shown to obscure oscillations due to spin splitting when compared with Lorentzian profiles with an equivalent broadening. The carrier density of a system was found to determine the frequency of oscillation and in the absence of spin splitting the amplitude of these oscillations were shown to be purely dependent on the degeneracy of states at each field. The inclusion of an energy dependent spin splitting to the Landau level energy spectrum was shown to introduce a periodic beating into the simulated density of states, which are created by oscillations of similar frequency interfering. A description of how the magnitude of the spin splitting could be discerned through the use of a Fourier transform was given.

The strength of the spin splitting parameter was deduced using magnetotransport measurements on a range of InSb quantum well samples with different carrier densities. The data shows the strength of the spin splitting monotonically increases with carrier density. Estimates of the spin splitting were found to be in the range $0.12 - 0.16\,\mathrm{eV\AA}$ for samples with carrier densities between $2.4 - 3.4 \times 10^{15}\,\mathrm{m}^{-2}$. Using values extracted from the raw data a comparison between the density of states oscillation using a parabolic and non-parabolic Landau level dispersion relationship was made. Good agreement was found between the observed oscillations in the data and those predicted using the non-parabolic energy spectrum.

The good agreement between the observed oscillation in ρ_{xx} and those predicted using the non-parabolic approximation suggests the approximation that Shubnikov-de Haas oscillations may be modelled by purely considering the variation in the density of states at the Fermi energy is a valid one. When the effects of quantum Hall discretisation become observable, the classical Hall model for the transverse conductivity breaks down and modelling the high field magnetoresistance becomes more complex. Valid parameters can still be extracted in the high field region, purely when considering the oscillation in the density of states.

Chapter 6

Three terminal differential conductance measurements

6.1 Introduction

The work presented in this chapter describes the measurement of the two-dimensional density of states extracted from the I-V characteristics of a device measured using a three-terminal setup. Performing this measurement over multiple magnetic fields allows the field and energy evolution of the average density of states to be probed without the need for external tools typically used for density of states measurements such a scanning tunnelling microscope (STM). The measurement of the density of states allows for device properties such as the Fermi energy, Landau level broadening, electron g-factor, and effective mass to be directly inferred.

The ability to make an ohmic contact to a device is important for efficient device design and operation. Non-linearities in the current-voltage (I-V) characteristic caused by the formation of a Schottky contact at the interface between a metal and semiconductor are used to investigate the potential profile of the band structure at an interface.

6.2 A metal-semiconductor interface on AlInSb

6.2.1 Schottky Barriers

The formation of Schottky barriers at a metal-semiconductor interface is a very well established phenomenon in all semiconductor materials [123, 125]. Much research has gone into understanding the processes and properties which govern the formation of such barriers. Schottky contacts behave as an electrical rectifier, allowing large amounts of current to pass when forward biased and only allowing a small current to flow when reverse biased, similar to the reverse bias characteristics of a p-n junction.

The formation of Schottky contacts on InSb heterostructures has been studied extensively [126–128] with Schottky behaviour having been observed at room temperature. Experience has shown that at low temperatures the formation of Schottky barriers in shallow contacted InSb heterostructures is quite common even when using techniques intended to create ohmic contacts. These small barrier heights are only significant at low temperature when the thermal distribution of carriers is small. Studies of the formation of small barrier Schottky contacts on InSb at low temperatures have not been widely reported, hence the low temperature properties of such barriers in this material are not greatly understood. This is a significant drawback when attempting to create devices with repeatable bias characteristics, such as split-gate structures intended to observe quantised conductance.

At low temperature, transport across a Schottky barrier is understood to occur by three main mechanisms, shown in figure 6.1. Carriers which have been thermally excited above the barrier can freely contribute to conduction, a process known as thermionic emission (TE). In structures studied here, the relatively narrow band gap of the surface AlInSb alloy results in a small Schottky barrier which only requires a small amount of energy for carriers to overcome. However, the low temperatures where devices were investigated in this thesis provide a negligible amount of thermal energy compared to a typical mid-gap pinned Schottky barrier, and as such thermionic emission will not be discussed in any more detail.

A particle wavefunction has a finite probability of penetration through a potential barrier (tunnelling) [129]; therefore, electrons at the Fermi energy have a finite probability of tunnelling through the Schottky barrier. At low temperatures, the quantum mechanical tunnelling of electrons close to the Fermi energy is the dominant source of leakage current in a Schottky device. This is because the thermal distribution of carriers around the Fermi energy is small and and an insignificant number of electrons have sufficient thermal energy to overcome the barrier. Thus, the majority of carriers which contribute to low temperature conduction through a Schottky barrier must tunnel through the barrier at the Fermi energy.

Schottky barriers can be approximated to a triangular potential being narrower at higher energies. Thermally excited carriers impinge on a narrower barrier and hence undergo an increased rate of tunnelling; therefore, thermally excited carriers with an energy less than the barrier height have a greater tunnelling probability due to their higher energy, and the narrower barrier at that energy. The probability of carriers tunnelling through the barrier is described by the *transmission coefficient* $T(E)$, an energy dependent quantity between 0 and 1.

In principle, ideal Schottky barriers have a potential height, Φ_B, that is proportional to the difference in the electron affinity of the two materials at the interface. This dictates the amount of charge transfer and band bending for the Fermi energies in the two materials to approach a state of equilibrium. This concept relies strongly upon the band structure of the materials being brought into contact being flat band, the same as that of material deep in the bulk. At the surface of a material, the symmetry of the crystal is interrupted and the periodicity of the Bloch function no longer holds. As such the idea that the band structure at the surface is similar to that in the bulk is not necessarily valid, and surface states can dominate the physics of surface interfaces.

6.2.2 Surface Pinning

The presence of defects, dangling bonds and native oxides at the surface of a semiconductor is known to create a distribution of available states which are not conformal with the band structure of the bulk material described by the solution to the Schrödinger

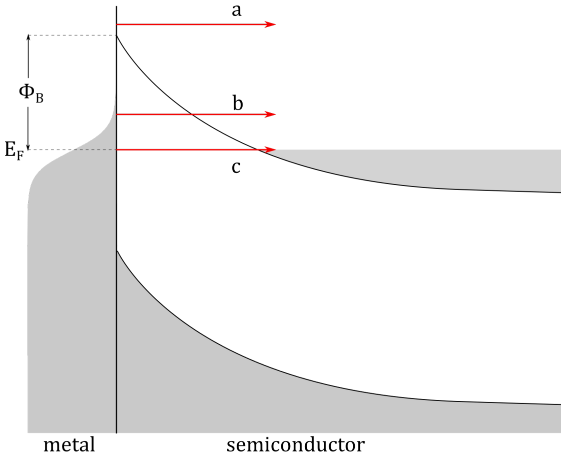

Figure 6.1: A schematic of the band structure of a heavily doped semiconductor with a Schottky barrier at the surface. The different transport mechanisms, (a) Thermionic emission of carriers over the top of the barrier, (b) Thermionic field emission of carriers above the Fermi energy tunnelling through the barrier, and (c) Field emission, carriers at the Fermi energy tunnelling through the barrier.

equation [125]. A finite number of states exist at energies within the band gap energy of the bulk material, creating a finite density of states between the conduction and valence band edges. These states are highly confined to the surface since the wave function of these states essentially decays exponentially into the band gap.

Available states which exist in the band gap require a sufficient transfer of charge from the conduction band to maintain charge neutrality. This transfer of charge raises the energy of the surface states until the Fermi energy at the surface is coincident with the Fermi energy of the bulk material. The resulting band profile has a barrier at the surface which is pinned to the surface states within the band gap and is established without the presence of a surface metal. The actual distribution of states in the band gap being purely at the mid-gap is unlikely; indeed, investigations have reported surface barriers which are pinned at the mid-gap, 1/3 - gap and at values in between [130].

Importantly for these material systems, this means that the height of the surface barrier is minimally affected by the work function of the metal deposited on the surface and is dominated by the distribution of surface states. Figure 6.2 shows a schematic example of the formation of a surface barrier due to nominally mid-gap pinning of the Fermi energy at the surface.

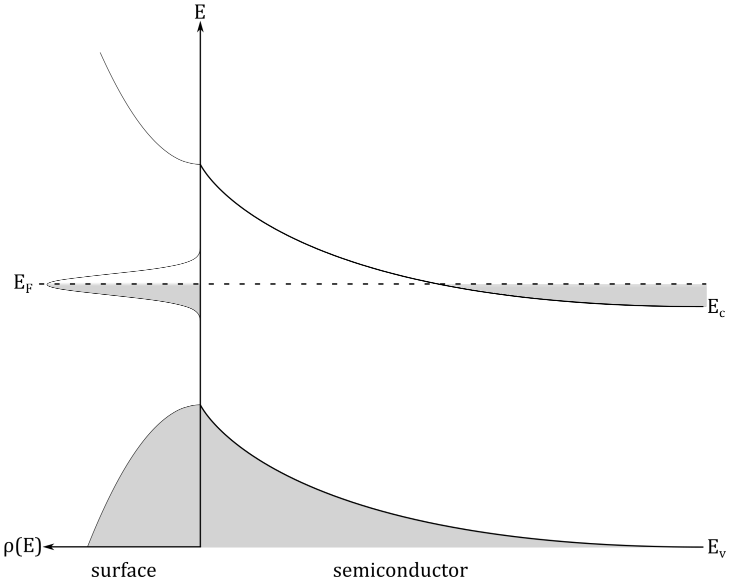

FIGURE 6.2: A schematic showing the density of states at the surface of a heavily doped semiconductor and the associated band structure created due to the pinning of the Fermi energy to the mid-gap states at the surface.

6.2.3 Tunnelling current through a surface barrier

The tunnelling current density from a metal to a semiconductor through a Schottky barrier at low temperatures at a metal-semiconductor interface can be described by the equation,

$$J_{ms} = e \int_0^{\phi_B} N(E)\nu(E)T(E)F_m(E)(1 - F_{sc}(E))dE \tag{6.1}$$

where $N(E)$ is the 3D density of states in the metal, $T(E)$ the transmission coefficient, $F_m(E)$ and $F_{sc}(E)$ are the Fermi-Dirac distribution of carriers in the metal and semiconductor respectively and $\nu(E)$ is the velocity of carriers toward the interface. For a single barrier, the transmission coefficient increases for carriers with increasing energy. The current through a barrier is therefore dependent upon the number of available states in the semiconductor and the number of carriers available at that energy in the metal, of which half should have a velocity component directed toward the interface. At higher temperatures, the average kinetic energy of carriers increases, this increased average carrier velocity increasing the likelihood of a carrier tunnelling through the barrier.

The quantisation of energy introduced by reduced dimensionality in heterostructures has a significant impact on the tunnelling coefficient since fewer states exist in the low-dimensional system than in the 3D system. When considering tunnelling from a 3D to a 2D system the constraints of conservation of energy and momentum requires a carrier which tunnels from one system to the other to conserve momentum between states. This can be envisaged as the coincidence between the Fermi sphere of the three-dimensional system and the Fermi circle of the 2D system, shown in figure 6.3. The greatest number of carriers which satisfy tunnelling conditions exist close to the zone center, thus the largest tunnelling rate is expected when the quantised state is coincident with the band edge of the 3D material.

In a metallic 3D system, the overlap of the conduction and valence band provides a uninterrupted density of states, unlike the 3D to 2D scenario where only a finite slice of the 3D electrons satisfy conditions to tunnel into the 2D system. In the reverse scenario there are sufficient states in the metal that satisfy the conservation conditions for all carriers to tunnel from the 2D system into the 3D system. At very low temperature, to a good approximation, all states below the Fermi energy are filled and the only states available for the transfer of carriers exist above the Fermi energy. Thus, for an electron to tunnel from the semiconductor into the metal carriers must have an energy greater than the Fermi energy. The application of an electric field alters the potential energy profile of the junction. The energy of carriers in the quantised states in the heterostructure can be increased by the application of an external voltage. A small bias will provide carriers with sufficient potential energy to tunnel into available states above the Fermi energy in the metal. If sufficient bias is applied to make the subband energy incident with the Fermi energy of the metal, all electrons in that subband have adequate potential energy to tunnel into the metal. The tunnel current of such a junction would therefore increase approximately linearly with bias until the potential energy of all carriers in the quantised states of the heterostructure is greater than the Fermi energy of the metal. At this voltage, all carriers are contributing to conduction and further increases in bias will not yield a significant increase in current, causing the I(V) characteristic to plateau once all states in the conduction band of the heterostructure are above the Fermi energy of the metal.

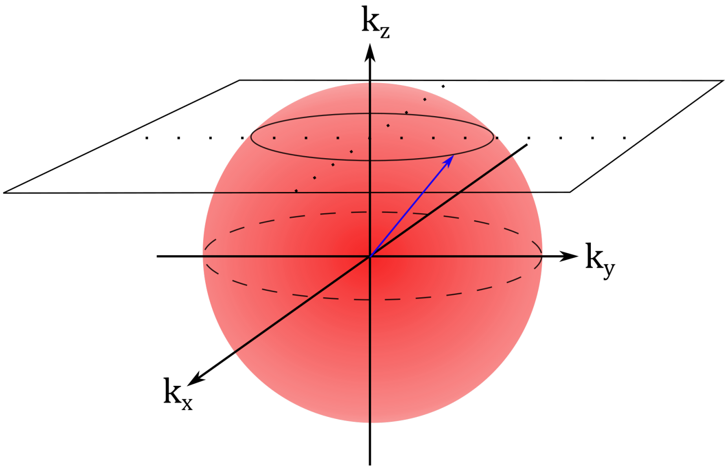

Figure 6.3: A schematic of the intersection between the 2D Fermi circle and 3D Fermi sphere. A carrier can only tunnel from a 3D to a 2D system by satisfying the conservation of momentum represented by the ring at the edge of intersection between the Fermi surfaces between the two systems.

In the presence of a magnetic field, the individual subbands of the heterostructure are additionally quantised into Landau levels and the distribution of states in the heterostructure is no longer linear as they are when B = 0 T. Therefore, under the presence of a quantising perpendicular magnetic field the I(V) characteristic of the junction should develop discrete steps until the energy of the fundamental Landau level is greater than the Fermi energy of the metal.

At low temperatures the I-V characteristics of a metal semiconductor interface can provide valuable information about the energetic distribution of carriers in the heterostructure. The small thermal distribution means carriers are well confined and the dominant transport mechanism is via tunnelling, the main contribution to changes in the current being through the number of carriers tunnelling through the barrier at the Fermi energy.

6.3 Differential Conductance Measurements

The non-linearity of the I(V) characteristics of a structure result in the break down of Ohm's law, the resistance of the material is no longer characterised by a constant gradient in the I(V) characteristic. More precise local information is required to define the resistance of a material as a function of the bias. The local gradient of the I(V) characteristic is known as the differential conductance, $(G = dI/dV)$. Such measurements

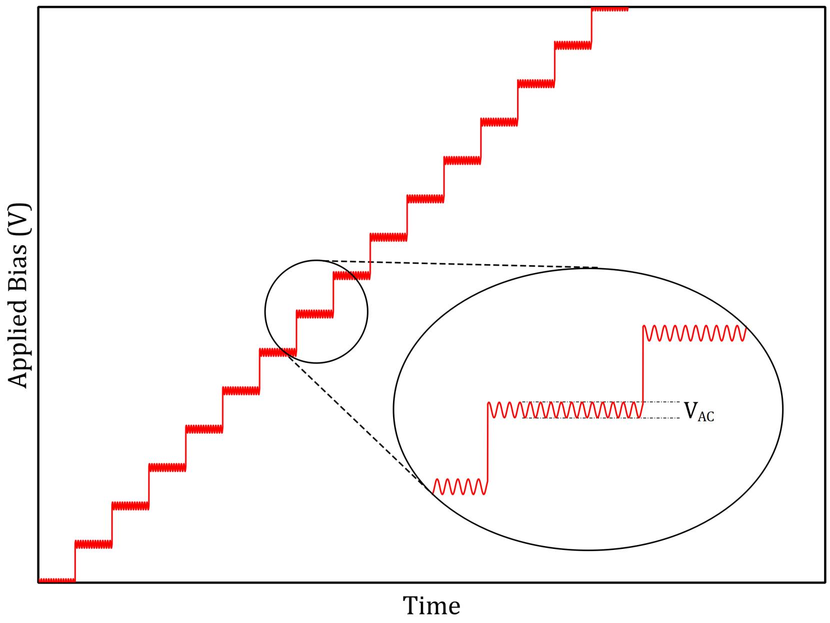

FIGURE 6.4: The excitation voltage applied to the device to measure the differential conductance as a function of DC bias. The differential conductance is extracted by software lock-in techniques of the AC signal.

are used extensively throughout the literature to map the energy spectrum of electrons in nano-devices [23, 131], in the study of material surfaces with a scanning tunnelling microscope [132–139], or to study the density of states of a heterostructure [140]. A differential conductance spectrum is a useful tool as it gives a maximal response where a small change in voltage yields a large change in current, highlighting energetically significant regions in the structure's density of states.

Though it is possible to extract the differential conductance by analysis of the gradient of the DC I(V) curve, this is highly susceptible to noise in the DC data. Application of a small AC excitation bias superposed on a DC offset (as shown in figure 6.4) allows both the I(V) characteristic and the differential conductance to be measured simultaneously. The time averaged current through the device at a certain bias provides the DC current of the I(V) characteristic. The current variation created by the AC excitation can be measured by lock-in techniques and does not rely on the difference between discrete points in the I(V) curve, allowing for improved signal to noise ratio from a single DC sweep. Observation of features using differential conductance is highly dependent on the size of the DC bias steps and the amplitude of the AC excitation, too large an excitation can smear out evidence of features in the differential conductance.

Various methods of using differential conductance measurements in two-dimensional heterostructures under the influence of magnetic fields have been investigated throughout the literature [140–147]. Main *et al.* [140] showed that the ground state of a quantum dot implanted into the barrier of an InAs quantum well can be used to probe the density of states as a function of field, and used the differential conductance to directly study the effective g-factor under the effects of exchange enhancement. A quantum dot is an ideal probe for this form of electron spectroscopy due to the precise energy of the confined state, allowing for a small energy range (and few carriers) to be probed. However, this has the downside that very small tunnel currents are measured since few electrons are energetically coincident with the confined state and techniques for measuring low currents must be employed. Differential conductance measurements are also used in Couloumb blockade thermometers (CBTs) to directly infer the temperature of the electron population [148].

The large spin-orbit interaction and large effective g-factor of narrow gap materials such as InSb or InAs make them attractive candidates for the study Landau level evolution from STM spectroscopy [132–134, 136, 139] and in the investigation of Majorana fermions (particularly in nanowires [131, 149–153]). For example, a distinct signature of the formation of the Majorana zero mode is the presence of a finite density of states in the superconducting gap [131].

6.3.1 Three terminal measurement

As described in chapter 3, the process for creating Ohmic contacts to the InSb/AlInSb heterostructures studied in this thesis was to thermally evaporate a Zn keying layer of $\sim 10\,\mathrm{nm}$ followed by a $300\,\mathrm{nm}$ thick Au layer while the sample is heated to $100\,^{\circ}\mathrm{C}$. During the measurement of two terminal devices intended for quantised conductance measurements it was found that the contact resistance of contacts deposited using this process was inconsistent, and in general significantly higher than the material resistance. This made observation of quantised states impracticable due to the large series resistance of both contacts. Shubnikov-de Haas measurements using devices processed into Hall bar geometries were made using 4-terminal measurement techniques where the contact

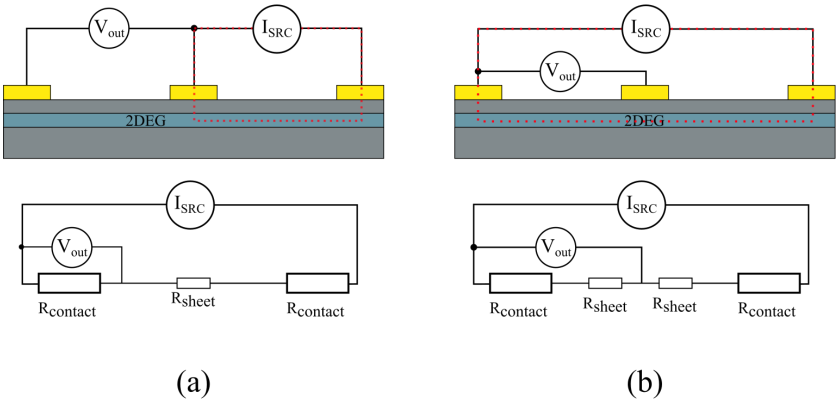

FIGURE 6.5: (a) A schematic of a typical three terminal I(V) measurement and (b) the three terminal circuit used during these measurements. Typical measurements exclude measuring the voltage drop across the 2DEG such that the only contribution to the voltage drop is from the contact resistance. The circuit configuration in these experiments necessarily measures the voltage drop across the 2DEG and the contact. As such the common contact for the voltage measurement and the current drain was chosen to be the most resistive contact on the device to maximise the voltage drop across the contact.

resistance is not an issue. The zero-field resistivity of a typical sample (SF1055) between Hall bar voltage probes was $\sim 100\,\Omega/\square$. In contrast, the contact resistance for devices made using this material ranged between $1.4\,\mathrm{k}\Omega$ to $> 1\,\mathrm{M}\Omega$.

Unlike a four contact measurement configuration, where the lead resistance of voltage probes may be neglected since they are assumed to carry minimal current, in a three terminal measurement configuration the contact resistance of the contact common to both the current and voltage probes is measured. In typical three terminal geometries the remote voltage probe does not measure any potential drop due to material series resistance, however, if the remote probe is located along the current path it will measure a series resistance contribution from the material. Hall bar geometries are typically unsuited for three terminal measurements as a series resistance contribution is always included in the measurement. If the common probe is selected such that the resistance of the common contact is significantly greater than the material resistance in these heterostructures, we can assume that the potential difference measured between the voltage probes is almost wholly dropped across the contact and not within the material of the 2DEG. Under this assumption the voltage measured can be used as an estimate of the potential difference between the Fermi energy of the metal and the quasi Fermi Energy of the 2DEG. A three terminal measurement across a very high resistance contact in series with a low resistance 2DEG thus allows an almost 1:1 equivalence between the measured potential and the potential difference between the quasi-Fermi energy of the metal and the quasi-Fermi energy of the 2DEG underneath the contact.

A self consistent Schrödinger-Poisson calculation for a typical InSb heterostructure studied in this thesis is shown in figure 6.6. Located between the quantum well and the surface is a δ-dopant plane. The role the δ-dopant plane plays in the transfer of charge from the 2DEG to the contact is uncertain. At sufficient dopant densities in the δ-doping plane the conduction band energy of the dopant plane can be lowered such that a predicted quantised state in the dopant layer exists below the Fermi energy. As there are available states at the Fermi energy in the dopant plane, electrons from the 2DEG may tunnel into the dopant plane before subsequently tunnelling into the contact, contributing to conduction in a two stage sequential tunnelling process. Alternatively, carriers might coherently tunnel directly from the 2DEG into the available states in the contact once sufficient bias has been applied without interacting with states in the dopant plane. Figure 6.7 shows a 3D schematic of this second process, the conduction band diagram indicates how the bias allows a proportion of carriers to tunnel from the 2DEG into the metal contact.

In these InSb Hall bar devices, the large variation in contact quality for multiple devices on a single chip indicates that the location of the contact has significant effect on the resistance. It is speculated that the better Ohmic contacts to this material are generated by contacting surface defects which continue through to the 2DEG. These defects interrupt the surface barrier and provide a conductive path for carriers to enter into the 2DEG. The consistency of material resistivity between devices on the same chip characterised using data from Hall effect measurements outlined in chapter 4 indicates that the variation in contact resistance is not likely to be due to material inhomogeneity. Therefore, somewhat counter intuitively, the lower the material quality the more likely it is to create higher quality Ohmic contacts to the 2DEG due to a greater defect density.

A schematic representation of the band alignment at finite magnetic field where the potential is dropped solely across the contact layer above the 2DEG is shown in figure 6.8. A peak in the differential conductance occurs when the applied potential difference

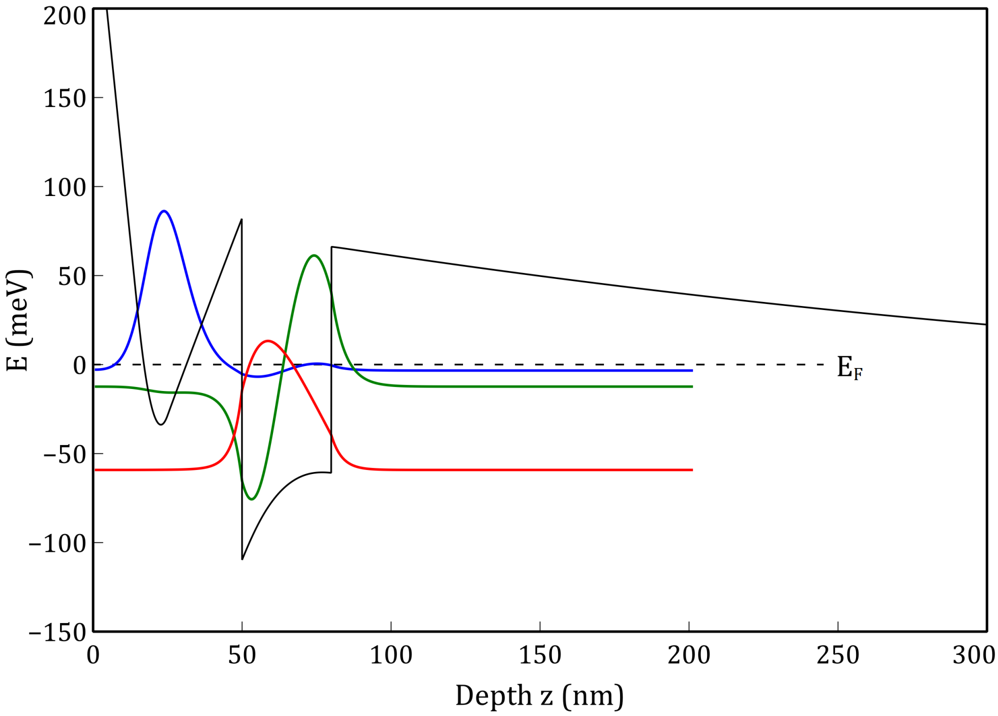

FIGURE 6.6: The Schrödinger-Poisson solution for the heterostructures studied in this thesis. Considering the δ-dopant as a 2 nm thick plane located 25 nm from the edge of the quantum well, a dopant density of $1.98 \times 10^{24}\mathrm{m}^{-3}$ is required for a state in the dopant plane to exist below the Fermi energy. Corresponding to a quantum well carrier density of $n_{2D} \simeq 4.2 \times 10^{15}\mathrm{m}^{-2}$. A low density n-type background of $4.0 \times 10^{20}\mathrm{m}^{-3}$ was used in the calculation.

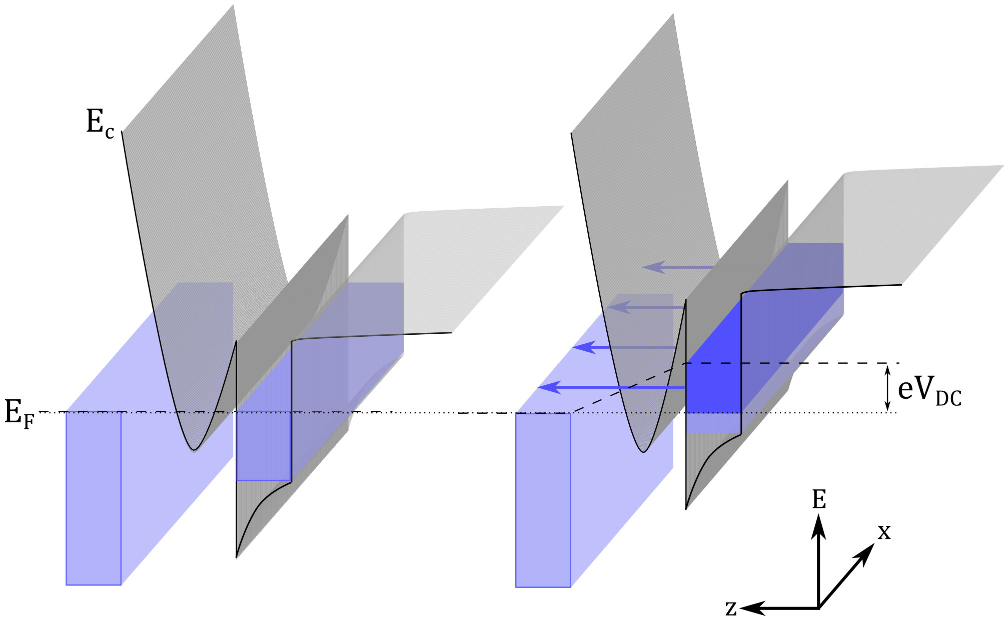

FIGURE 6.7: A 3D schematic of a likely transport mechanism. (Left) The equilibrium condition under zero bias. (Right) When bias is applied to the structure the quasi-Fermi energy of the 2DEG increases, the number of electrons in the quantum well with an energy greater than the Fermi energy of the metal is proportional to the applied bias.

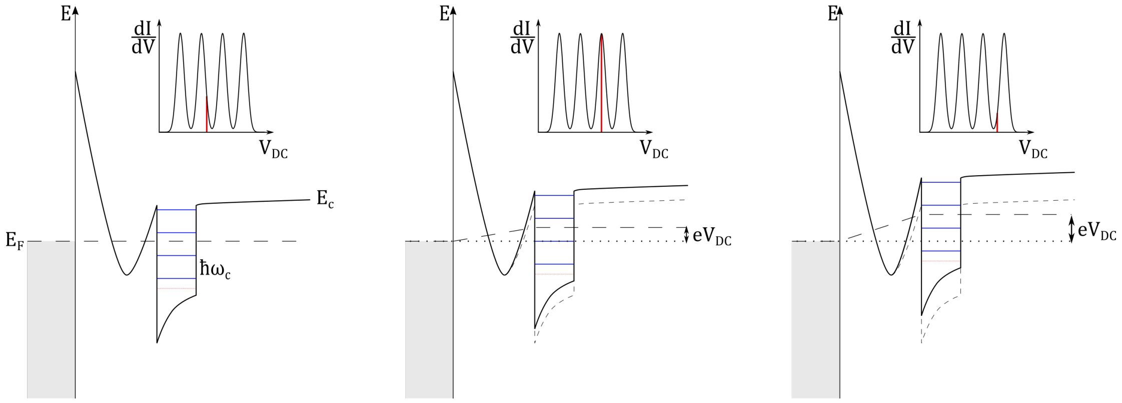

Figure 6.8: A 2D schematic of the band structure of the system at a finite magnetic field and the corresponding differential conductance. Left to right images show the effects of increasing the linear bias across the device. When the Fermi energy of the metal is coincident with a Landau level in the quantum well a peak in the differential conductance is observed due to the large variation in current over a small bias region.

causes a Landau level to become coincident with the Fermi energy of the metal. The large number of electrons which occupy the Landau level will then have sufficient energy to tunnel from the 2DEG into the contact increasing the current through the device.

6.4 Measurements on a high mobility InSb 2DEG

Differential conductance measurements were performed for two samples (SF0963 and SF1055) at cryogenic temperatures below 4 K. The low temperature I(V) characteristic and corresponding differential conductance trace measured across a single contact at multiple magnetic fields is shown in figure 6.9. The I(V) characteristic at all fields displays a distinct plateau at high reverse bias corresponding to the subband edge being raised above the Fermi energy of the metal and all electrons occupying the subband becoming available for conduction. The differential conductance trace exhibits distinct peaks. The separation of peaks observed within the bias range is found to be inversely proportional to the magnitude of the applied field consistent with the formation of Landau levels. The amplitude of each peak is evidently proportional to the magnetic field strength. This is commensurate with the increasing degeneracy of states in each Landau level at higher fields. At high field the fundamental Landau level clearly consists of two peaks suggesting the emergence of spin resolvable Landau levels. The lack of complete separation between these peaks is due to the extent of the finite level broadening for each Landau level.

There is an obvious suppression in the differential conductance peak amplitude when the reverse bias is smaller than $\sim -40\,\mathrm{mV}$, this is believed to occur due to the contact resistance being non-dominating in this bias region. Hall bar geometries are ill-suited for three terminal measurements as the remote voltage probe will always measure the voltage drop across the contact in conjunction with a small amount of material which carries current to the contact. The small amount of material which is measured between the remote voltage probe and the contact contributes as a series resistance which "smears" features out in voltage, when the contact resistance dominates this smearing is insignificant. The oscillation of the resistance of the 2DEG under the influence of a perpendicular magnetic field results in the ratio between the resistance of the 2DEG and the contact changing dependent upon the magnitude of the applied field. Under these circumstances measurements are performed on contacts with the largest possible contact resistance to minimise the effects of the oscillating 2DEG resistance.

The current plateau in the I-V characteristic at large negative bias reduces approximately linearly with magnetic field, from $-1.8\,\mu\mathrm{A}$ at $0\,\mathrm{T}$ to $-1.3\,\mu\mathrm{A}$ at $8\,\mathrm{T}$. The linearity suggests the current limiting is not due to the variation in the resistance of the 2DEG with increasing field which would cause it to oscillate with a $1/B$ periodicity, instead this is likely attributed to a reduction in the carrier density under the effects of a large bias.

Observation of the amplitude of differential conductance for the $N = 0$ peak versus field is shown by the upper panel of figure 6.10, the amplitude shows clear oscillation with increasing field. Assuming the contact resistance remains largely unaffected by the application of a magnetic field, these oscillations can be explained due to the varying ratio of resistances in the potential divider model between the contact and the 2DEG due to the oscillating material resistivity. This shows the extent to which the variation in 2DEG resistance affects the amplitude of the differential conductance measured at a single field. Assuming the magnitude of the differential conductance is proportional to the number of electron states which exist at that energy, and the total number of

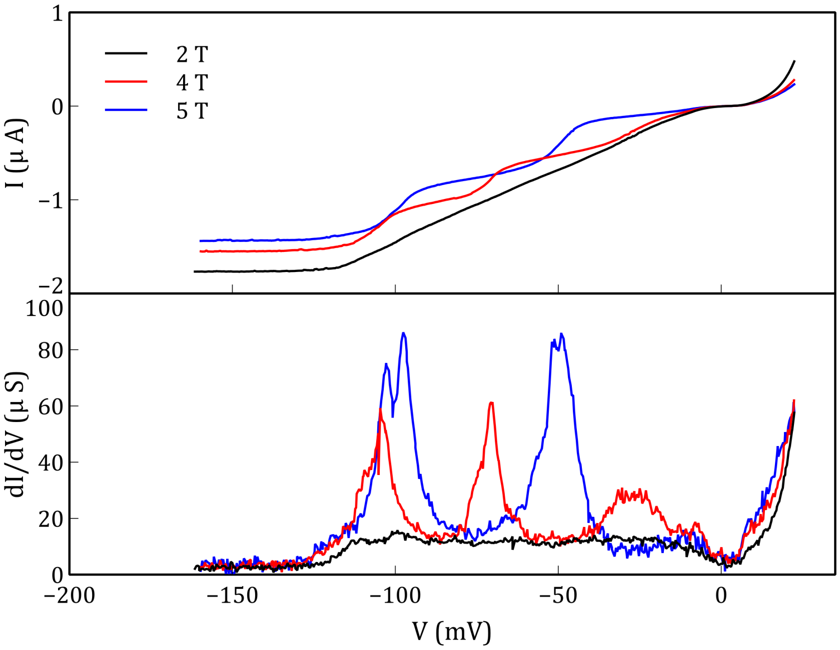

Figure 6.9: The 4 K I-V characteristic and differential conductance data for sample SF1055 at multiple fields. Under reverse bias the low field I-V shows an almost constant gradient before a plateau at high bias. The data at higher fields shows more complicated structure. Turning points in the I-V curve manifest as peaks in the differential conductance.

occupied states remains the same, normalisation to the area underneath the differential conductance curve provides a relative estimation of how the degeneracy of states increases with magnetic field. Though this assumption does not take into account the oscillation in the Fermi energy of the 2DEG, it provides a decent first order estimation of the degeneracy of the density of states within the fundamental Landau level.

The effects of this normalisation are shown in the lower panel of figure 6.10, yielding two distinct linear regimes overlapping at $B \approx 2\,\mathrm{T}$. Below 2 T the observation of individual Landau levels is not possible against the background density of states. This background density of states may, for example, be due to the presence of states in the dopant plane of the top barrier of the quantum well [139]. The quantised states in the δ-dopant plane would also discretise under the application of a magnetic field; however, due to the larger effective mass of electrons in the AlInSb barrier these barrier Landau levels would separate in energy much less rapidly. The presence of the δ-dopant would also result in extremely broad Landau levels due to the large scattering potential encountered by carriers from the ionised impurities; thus, if any carriers did occupy a state in the

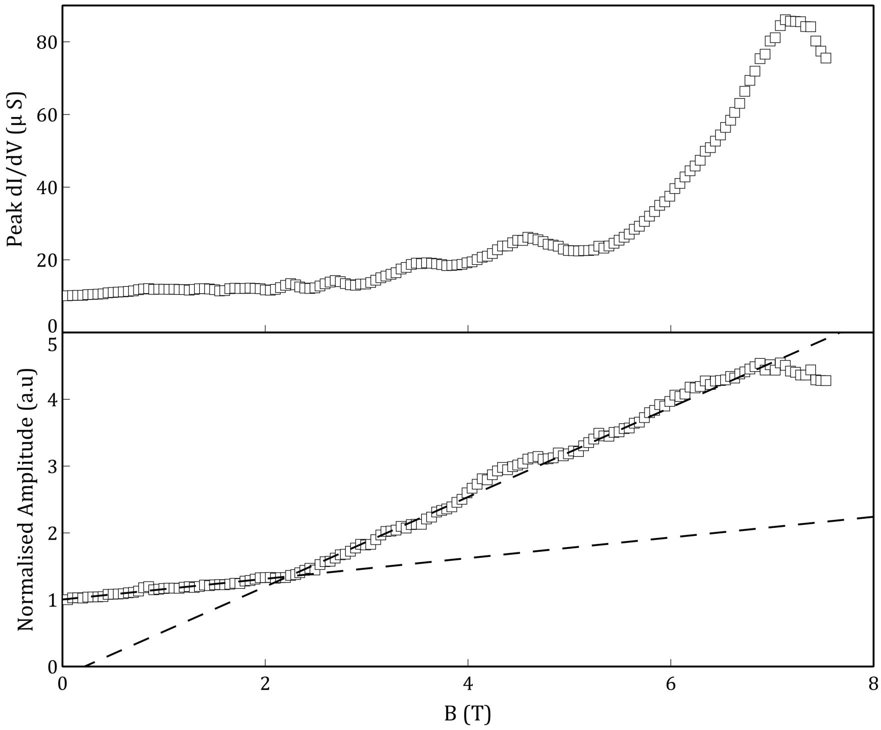

FIGURE 6.10: (Top) The amplitude of the differential conductance peak from the $n = 0$ Landau level as a function of magnetic field. (Bottom) Normalisation of the differential conductance data to the area underneath the curve yields two distinct linear regions.

dopant plane the quasi-Fermi energy may be considered as approximately constant due to the large level broadening. In the high field region, the straight line fit to the data projects backward to a zero field intercept of almost 0 as would be expected if the peak magnitude was proportional to the degeneracy of states, which is zero at $B = 0\,\mathrm{T}$.

Investigating the differential conductance over the same bias range but at finer field steps is shown in figure 6.11(a). The magnetic field evolution of the differential conductance yields an experimentally determined Landau fan. A Landau fan for the first four Landau levels is overlaid to show the close agreement between the data and the predicted evolution with field. The high bias data in region 2 is found to be approximated well by a Landau fan calculated using the band edge effective mass for InSb of $m^* = 0.014\,m_0$ The effects of the "smearing" at low bias becomes extremely obvious when compared to the prediction, the peaks in region 1 of figure 6.11(a) show significant deviation from the predicted magnetic field evolution. The absence of peaks below 2 T also becomes more apparent, interestingly surface STM analysis of induced surface accumulation layers on bulk n-InSb also fail to resolve peaks in this region [139]. The minimum field at which observation of Landau levels is possible using this technique is therefore not limited by the energy resolution, and the minimum field is governed by the background density of states of the dopant plane.

A linear scaling of the low bias data in region 1 can compensate for the effects of this bias smearing. Multiplication of the low bias region by a single scaling factor of ≈ 1.5 is sufficient to make the peak energies coincident with the energies predicted by the Landau fan as shown in figure 6.11(b). This can be understood by considering the material as a potential divider, a series resistance contribution in addition to the contact resistance such that the measured potential difference is not wholly dropped across the contact. The single scaling factor indicates that the series resistance contribution is not dependent on the magnitude of the bias, instead it changes abruptly beyond a critical bias. The precise cause of the change can not be directly inferred from these measurements and may only be speculated as being from the exclusion of an energy dependent scattering mechanism. A possible candidate for such a mechanism is the presence of a second subband in the quantum well. The occupation of the second subband increases the scattering probability due to both intra and inter-subband scattering mechanisms being present [39]. If sufficient bias is applied to deplete carriers from the quantum well, such that the second subband becomes depopulated, the scattering probability will decrease since inter-subband scattering becomes less probable resulting in a decrease in the resistance of the quantum well. A greater proportion of the potential difference measured would then be dropped across the contact and a nearer to 1:1 equivalence between the measured voltage and the potential difference between the Fermi energies of the metal and semiconductor would be observed.

The low temperature carrier density extracted for this heterostructure from low field Hall analysis gives $n_{2D} = 3.3 \pm 0.2 \times 10^{15}\,\mathrm{m}^{-2}$. Self consistent Schrödinger-Poisson calculations for a bare structure with a similar carrier density predicts the lowest subband of the quantum well to be approximately 50 meV below the Fermi energy and a separation between confined states of 48 meV. The Landau fan in figure 6.11(b) has a zero field intercept of −98 meV suggesting that the quantised state in the well exists 98 meV below the Fermi energy, almost twice the predicted value for the bare structure. Since this

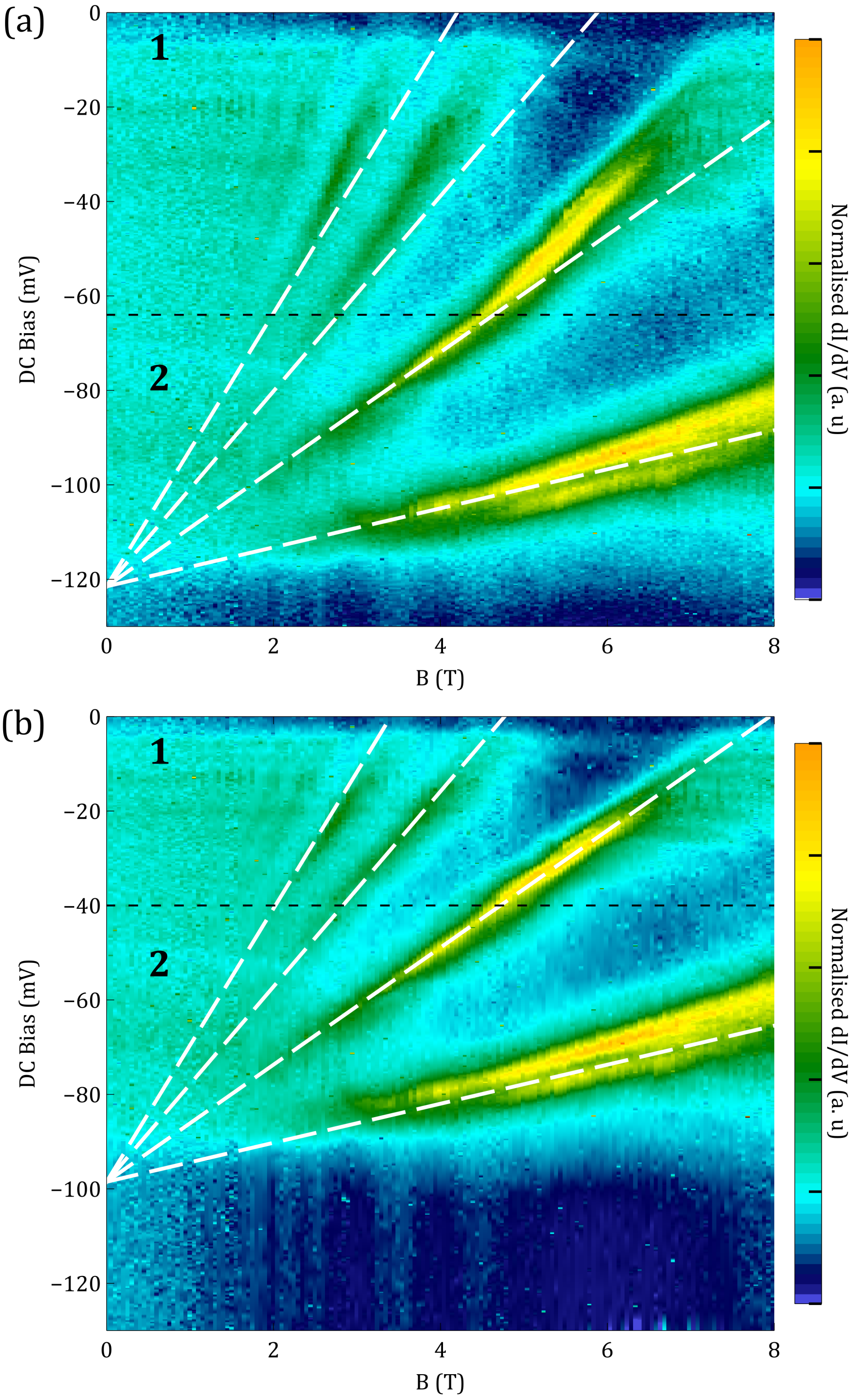

FIGURE 6.11: (a) A 2D plot of the differential conductance measured across a high resistance contact as a function of bias measured across the contact and magnetic field. In region 2 high intensity regions evolve in very good agreement with the predicted evolution of a Landau fan calculated using the band edge effective mass of InSb, while in region 1 the high intensity peaks show significant deviation from the prediction. (b) Scaling the data in region 1 by a constant value of $0.7V_{DC}$ brings the high intensity regions back into good agreement with the energies predicted by the Landau fan. This data predicts the Fermi energy of the quantum well underneath the contact to be $\sim 100\,\text{meV}$ above the subband energy at zero field.

measurement only probes the density of states below the contact this suggests that the presence of the metal creates a significant distortion to the bandstructure, considerably decreasing the subband energy below the Fermi energy.

If the bias smearing in region 1 of figure 6.11(a) is caused by the occupation of the second subband the boundary between regions 1 and 2 should be approximately equal to the subband separation above the bottom of the lowest subband. The boundary between the two regions is found to be approximately 58 mV above the zero field intercept of the Landau fan. This is not an unreasonable value for the subband separation as any enhancement of the asymmetry in the quantum well will lead to an increase in their energy separation. It is worth noting however that the differential conductance data shows no evidence for a second Landau fan with a zero field intercept at the boundary between regions 1 and 2, which suggests that no second subband exists in the quantum well beneath the contact.

6.5 Magnetic field evolution of peak width and line shape

Scrutiny of the $N = 0$ peak at high field reveals it to have an asymmetric, double peaked structure thought to be from individual density of state contributions from spin split Landau levels. As discussed in the previous chapter there is debate in the literature as to the form of the distribution of carriers within Landau levels, different authors describe their data as having either a Gaussian or Lorentzian distribution. The shape of the differential conductance curve can yield information about the distribution of states within that Landau level. Through use of a residual minimisation algorithm it is possible to fit a multiple peak lineshape to the differential conductance data in an effort to determine the shape of the distribution of the density of states.

The results of such a minimisation when using Lorentzian broadened Landau levels is shown in figure 6.12. The expression which describes the density of states of a 2D material under the application of a magnetic field is given in chapter 5 but it shall be reiterated here for discussion. The equation for the density of states for two Landau

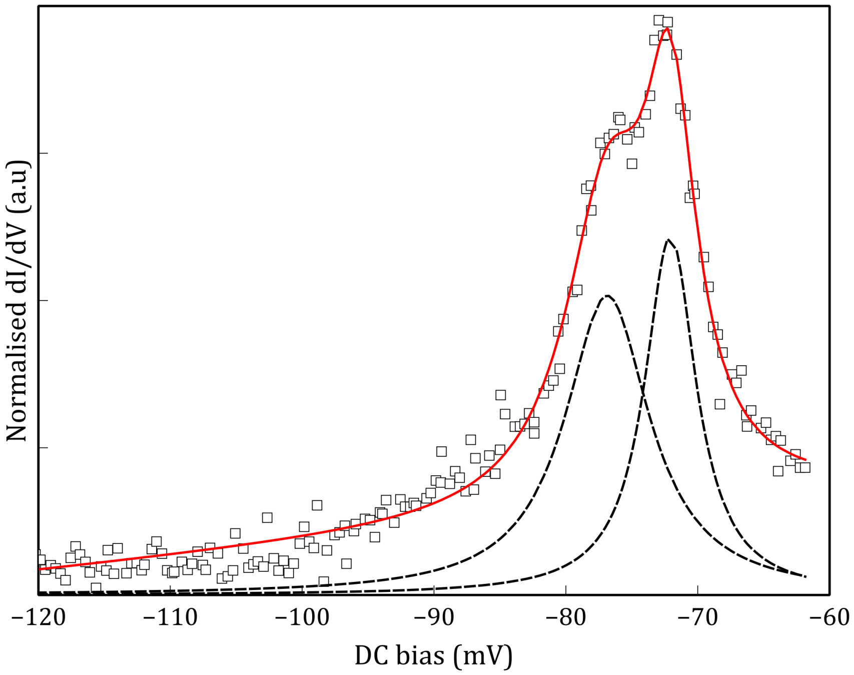

FIGURE 6.12: An example of the quality of fit achieved by fitting a two Lorentzian model to the 4 K differential conductance data on sample SF1055 at 5 T. Good agreement between the fit and the data is achieved here with Lorentzian widths $\Gamma_+ = 4 \pm 1$ meV and $\Gamma_- = 10 \pm 1$ meV.

levels with different broadening parameters is

$$g(E,B) = \frac{eB}{\pi\hbar}\frac{1}{\pi}\sum_{N_\pm=0}^{\infty}\frac{\frac{1}{2}\Gamma_+}{(E-E_{N_+})^2-\left(\frac{1}{2}\Gamma_+\right)^2}+\frac{\frac{1}{2}\Gamma_-}{(E-E_{N_-})^2-\left(\frac{1}{2}\Gamma_-\right)^2}, \tag{6.2}$$

where $\Gamma_\pm$ are the broadening parameters of the two spin states. The data is very well approximated by a model consisting of two Lorentzian broadened peaks on top of a constant background (necessary for non-zero amplitude of the differential conductance) similar to models used by Gornik *et. al.*, Smith *et. al.*, Ashoori *et. al.* and Templeton [73, 75, 77, 82]. As the area underneath each probability distribution must equal unity, any increase in the width of the lineshape must be compensated by a decrease in the peak amplitude. The amplitude of the Lorentzian curve describing each spin state scales with a common degeneracy, as such the only free fitting parameters in the model are the peak centres, peak width as well as the gradient and intercept of the linear background.

The results of estimating the broadening of the spin split Landau levels from fitting of the differential conductance data are shown in figure 6.14. The model consistently extracts two distinct broadening values for the two spin states. The high energy spin

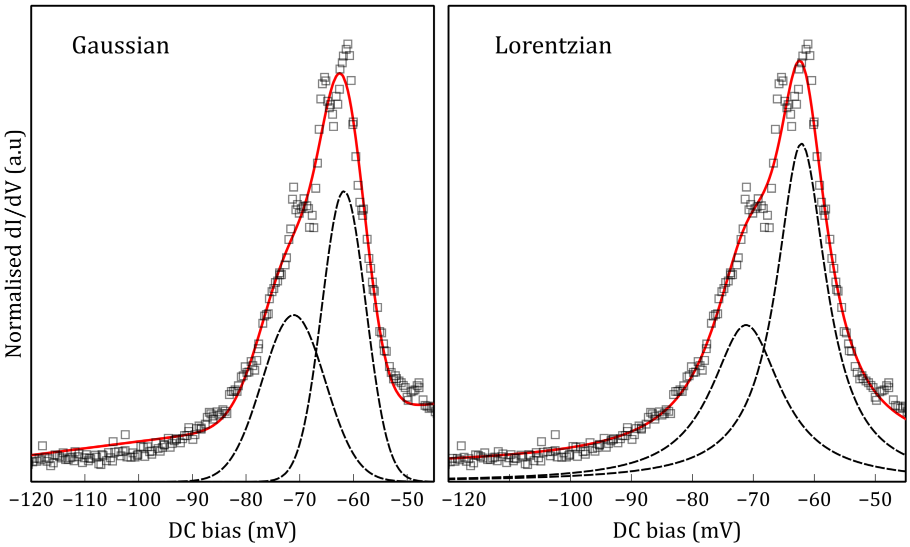

Figure 6.13: A comparison between the quality of fit extracted using Gaussian or Lorentzian broadening profiles for data at 7.23 T. Though both profiles reasonably approximate the trend of the differential conductance peak, the off-peak fit of the Lorentzian broadening is clearly superior to that of the Gaussian profile.

state Γ_+ exhibits a characteristic broadening of $\sim 4\,\mathrm{meV}$ in very good agreement with the values estimated from the low field Shubnikov-de Haas data in chapter 2 for the same material and displays no strong field dependence between 5 and 8 T. The low energy state Γ_- exhibits significantly larger broadening $\sim 10\,\mathrm{meV}$ at 5 T and increases by almost 50% over the same field region. The high and low energy state broadening parameters are compared to a fit of $\eta\sqrt{B}$, where η is just a scaling coefficient. These were found to be $\eta_+ = 1.2 \pm 0.2\,\mathrm{meVT}^{-\frac{1}{2}}$ and $\eta_- = 4.5 \pm 0.1\,\mathrm{meVT}^{-\frac{1}{2}}$, the state exhibiting large broadening being described well by the fitted curve. These values are significantly larger than those extracted by magnetocapacitance and magnetisation measurements for 2D GaAs/AlGaAs systems with nominally similar carrier densities [81, 154, 155], reflective of the considerable single particle broadening in these InSb heterostructures. Error bars for each data point were calculated by running the fitting routine on each data set multiple times with a random number of points removed from the set, the maximum and minimum values for the extracted parameters at each field were then taken as the limits of the error bars[*].

As discussed briefly in the previous chapter, predictions for the behaviour of Landau level broadening with respect to magnetic field show no consensus throughout the

---

[*] This technique is similar to the standard Jackknife variance estimation procedure used extensively throughout the astronomical community for the estimation of model confidence [156, 157]

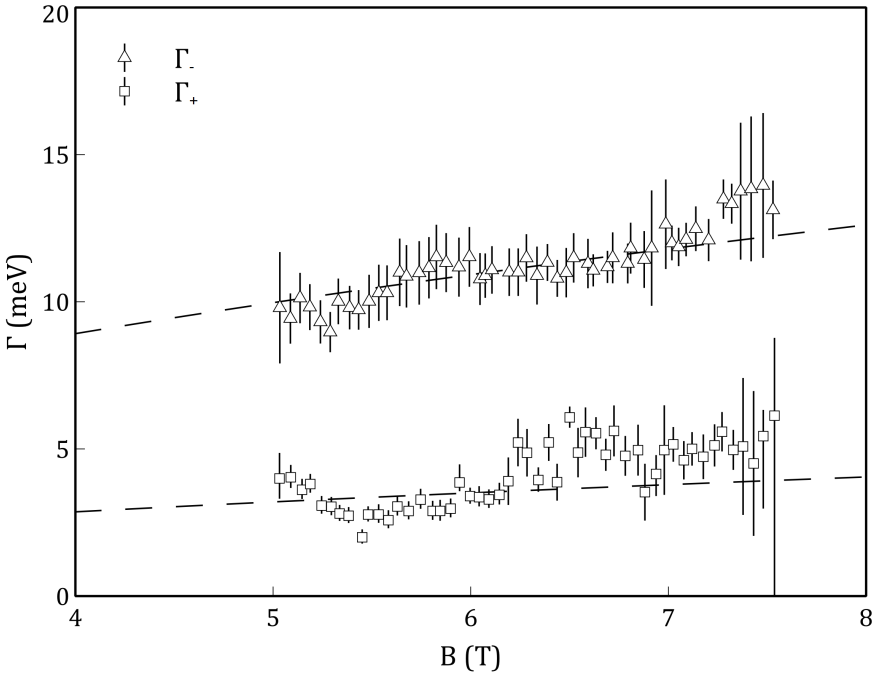

FIGURE 6.14: The broadening parameters for the high and low energy spin states Γ_+ and Γ_- extracted from a double Lorentzian fitting to 4 K data for sample SF1055. Two distinct broadening parameters are extracted from the data. The black dashed lines are $\eta\sqrt{B}$ fits to the data. The broadening of the low energy spin state shows strong agreement with the fit.

literature[158, 159]. Some authors present data which is best modelled using a Gaussian broadened lineshape [72–74, 76, 77, 160], while a small number of authors report data better modelled using a Lorentzian distribution [82, 158]. The magnetic field dependence of the broadening has been reported to be either $\propto \sqrt{B}$ [79, 81, 155, 160] or to be field independent [73, 75, 77, 82]. The differential conductance peaks shown here show significant tails consistent with a Lorentzian broadened distribution. Successful fitting to the peaks using a Gaussian profile fails to account for these, as shown in figure 6.13. The large difference in the broadening of the two spins states indicates that carriers in each state have significantly different quantum lifetimes and the presence of a considerable spin dependent scattering mechanism within the heterostructure.

6.6 Evidence for g-factor enhancement

Using the separation between the centres of the fitted Lorentzian peaks, it is possible to infer a magnitude for the effective g-factor of the material and the evolution of the state separation with magnetic field. Assuming the most significant contribution to the spin splitting at high field comes from the Zeeman contribution, the energy separation between the spin split levels should be well approximated by $\Delta E = g^{*}\mu_{B}B$. The extent of the spin splitting extracted from the model is shown in figure 6.15. The magnitude of the effective g-factor is similar to values extracted by comparing the field onset of combined and spin split resistance oscillations from Shubnikov-de Haas measurements. The extent of the separation between spin split levels is found to vary with the strength of the applied field, exhibiting an initial decrease at fields beyond 5 T before showing a consistent increase, corresponding to a variation in the effective g-factor of $23 < |g^{*}| < 36$. When compared to values of g^{*} extracted from tilted field measurements of similar 30 nm InSb quantum well heterostructures [87], good agreement is found with the values reported here. The error estimates for these values were made using the same technique for estimating the error in the peak broadening.

The phenomenon of g-factor enhancement is thought to be due to $e-e$ interactions when there is a spin polarised electron population, the larger the spin polarisation the greater the enhancement in the g-factor. An important point to note is that at the minimum field where data has been successfully extracted, structures with a carrier density of $n_{2D} = 3.3 \times 10^{15}\,\mathrm{m}^{-2}$ are close to having the second Landau level completely depopulated and consequently a minimal net spin population. The subsequent depopulation of the electrons from the higher energy spin state then starts to occur with increasing field, leading to an increase in the net spin population of the occupied Landau level, this coincides with the increasing value for the effective g-factor extracted here. Consequently the increase in the value for g^{*} extracted here provides strong evidence for the enhancement being due to the onset of net spin population.

6.7 Summary

The low temperature current-voltage characteristics of a high resistance contact on a high quality InSb quantum well heterostructure processed into a Hall bar geometry have been presented. These characteristics have been shown to be sensitive to the

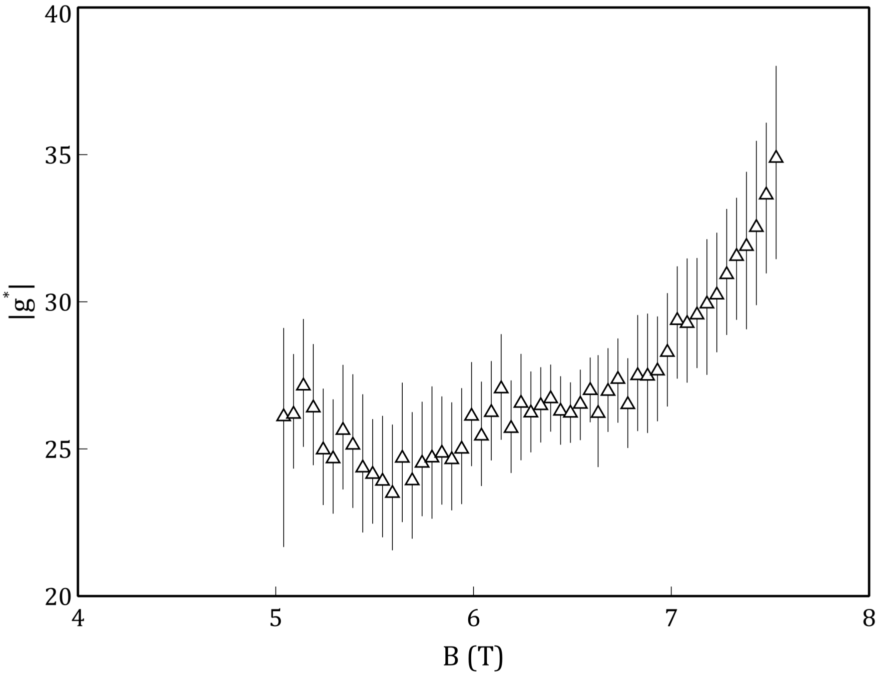

FIGURE 6.15: Values for the magnitude of the effective g-factor estimated from the separation between two Lorentzian peaks fit to the 4 K differential conductance data for sample SF1055. At high field a distinct increase in the separation is observed, suggesting an increase in $|g^*|$.

application of a perpendicular magnetic field, changing distinctly at high magnetic field. The differential conductance of these characteristics was presented and shows the onset of a distinct number of peaks at moderate field, likely due to the formation of Landau levels in the quantum well. The magnetic field evolution of these peaks confirms they are caused by Landau level formation by comparison with the magnetic field evolution of calculated Landau level energies and good agreement is achieved with a parabolic model with a band edge effective mass of $m^* = 0.014m_0$.

Examining the magnetic field evolution of the $N = 0$ Landau level at fields above 5 T has allowed an estimation of the broadening of the Landau levels and extraction of the material effective g-factor. A model consisting of two Lorentzian distributions on a linear background was fit to the data and estimations of the broadening was made using the width of the two Lorentzian peaks. Two distinct broadening parameters were extracted suggesting the presence of significant spin dependent broadening in these structures. The value of these broadening parameters was found to be well described by a $\sqrt{B}$ dependence, with coefficients $\eta_+ = 1.2 \pm 0.2\,\mathrm{meVT}^{-\frac{1}{2}}$ and $\eta_- = 4.5 \pm 0.1\,\mathrm{meVT}^{-\frac{1}{2}}$ for the high and low energy peaks respectively.

Use of the same model allowed an estimation for the spin splitting of the lowest Landau level as a function of magnetic field to be performed. The magnitude of the spin splitting was shown to be dependent upon the strength of the magnetic field, having a minimum value of $g^* = 24{\pm}2$ at $B = 5.6\,\mathrm{T}$ and rising steadily to a value of $g^* = 35{\pm}3$ at $B = 7.5\,\mathrm{T}$. These are in good agreement with values extracted using tilted field techniques in similar InSb quantum well systems [87].

Chapter 7

Conclusions and further work

In this thesis a number of electronic transport phenomena have been studied at low temperatures using high quality 30 nm InSb quantum well heterostructures, with the aim of extracting material parameters pertinent to electron transport and studying spin effects under magnetic field in this high g-factor material. The main areas of investigation discussed in the previous chapters are:

i) The resistive behaviour of both gated and ungated Hall bars under the application of moderate magnetic fields. These were investigated at temperatures ranging between 3 and 20 K. Using gated structures this behaviour was studied over a range of carrier densities between $1.5 - 3.5 \times 10^{15}\,\mathrm{m}^{-2}$.

ii) Using a Landau fan model to investigate the effects of different material and structural parameters on the observed oscillations in the density of states at the Fermi energy. This model was then used to extract material parameters from measured Shubnikov-de Haas oscillations.

iii) The low temperature measurement of I-V characteristics for an InSb Hall bar in a three terminal configuration across a highly resistive contact were analysed to extract information about the energetic distribution of states beneath the contact.

The main works described in (i), (ii) and (iii) have been thoroughly described in chapters 4 to 6. This chapter aims to summarise the pertinent findings of the work assembled in this thesis, drawing attention to their potential implications and applications. A brief proposal for future works is then described, with the aim of achieving a better understanding of the underlying physical principles or exploiting the findings described here.

7.1 Conclusions

The single particle quantum lifetime and the classical transport lifetime are well studied phenomena. Comparison between the two is a useful tool used in order to determine the scattering mechanisms present in a heterostructure at low temperatures where quantum phenomena are observable. Chapter 4 presents both the low and high field magneto-transport data for high quality InSb quantum wells processed into 6-contact Hall bars. The transport properties of both gated and ungated Hall bars were investigated to study the role of carrier density and temperature on the classical and quantum lifetimes, extending the work of Hayes *et al.* [34].

When comparisons between the transport properties of gated and ungated samples created from the same material were made, it was found that the presence of a dielectric layer and gate electrode had a significant impact on both lifetimes. The deposition of a surface gate was found to reduce the classical lifetime of carriers in the quantum well by approximately 50 % compared to lifetimes of structures with only the bare material, signifying the introduction of a significant scattering mechanism. The classical lifetime of carriers was found to be linearly proportional to the carrier density, consistent with increasing Thomas-Fermi screening at higher carrier densities. The gradient of the linear proportionality was observed to be different with the application of different gate dielectrics, suggesting the classical lifetime is highly dependent upon the properties of the dielectric deposited on the sample surface.

In comparison the quantum lifetime was found to only be slightly perturbed by the presence of the gate electrode and dielectric, showing a reduction from the ungated values by around 10 %. Similar to the classical lifetime the quantum lifetime was observed to be proportional to the carrier density in the quantum well, though the properties of the dielectric layer were found not to have a significant effect on the quantum lifetime with lifetimes for both materials being well described by the same linear fit. This similarity suggests that the scattering mechanism limiting the quantum lifetime is structural, potentially due to ionised impurities within the 2DEG, independent of the remote scattering potential from the dopant plane. Consequently, the ratio between the classical and quantum lifetimes shows a considerable reduction due to the lower classical lifetime, this reduction can be accounted for by the inclusion of a second scattering potential located at the sample surface. This suggests that the additional scattering mechanism is due to immobile ionised impurities at the dielectric surface interface. In order to model the reduction in transport ratio the surface defect density needed to be of the order $10^{17}\,\mathrm{m}^{-2}$, similar to dielectric defect densities reported in the literature for dielectrics on similar ternary alloys [69].

Investigations over a range of temperatures up to 20 K showed that the quantum lifetime has no strong temperature dependence, demonstrating that the quantum lifetime is not limited by thermally dependent scattering mechanisms such as $e - e$ interaction, or limited due to phonon scattering. The quantum lifetime was used to determine the single particle broadening parameter Γ for these structures, varying between 2 and 4 meV and was shown to be inversely proportional to the carrier density. Examination of the decay in oscillation amplitude as a function of temperature was used to determine a value for the effective mass of carriers in the structure and was found to be $m^* = 0.018 \pm 0.003\, m_0$, consistent with predictions from a 4-band $\boldsymbol{k.p}$ model.

Using these parameters, numerical simulations of the density of states as a function of magnetic field were performed and compared to Shubnikov-de Haas measurements performed on ungated Hall bar structures. Understanding the role different material parameters play on the oscillations observed in Shubnikov-de Haas oscillations is vital when attempting to extract information from analysis of the form of those oscillations. Small variations in particle broadening, carrier density, spin splitting or the incorporation of inhomogeneous broadening can have notable effects on the observed oscillation and the Fourier transform of such oscillations. The form of the Fourier transform holds considerable information about the measured oscillations.

The relatively large single particle broadening determined for these structures showed considerable differences between the oscillations modelled using Gaussian or Lorentzian distributions. Spin split oscillations due to Landau levels modelled by Lorentzian distributions were discernible at much lower fields than oscillations predicted by Gaussian Landau levels. Shubnikov-de Haas data for these structures reveal spin split oscillations at fields below 1 T. Gaussian broadened Landau levels required a significantly smaller broadening parameter than those extracted here to describe the data. Lorentzian broadened Landau levels with broadening parameters consistent with those extracted from quantum lifetime measurements show spin-split oscillations to much lower fields due the narrower peak width, suggesting that in these structures the Landau levels are best described by Lorentzian broadening. Scrutiny of the field positions for peaks in resistivity were found to be consistent with the modelled peak locations of a model with an effective g-factor of 30. This value is consistent with those extracted by other authors investigating similar structures.

A comparison has been made between the oscillations predicted by the Landau level distribution from a parabolic density of states to those of a non-parabolic model. The distribution of Landau levels predicted by the inclusion of a non-parabolic density of states was shown to introduce an apparent phase shift in the oscillations at low fields when compared to the Landau level distribution predicted by the parabolic approximation. The predicted oscillations using a non-parabolic distribution of Landau levels showed best agreement with the measured data, with peak locations corresponding well at low field. InSb is known to have a significant spin orbit interaction compared with other III-V materials. When a field independent spin splitting due to a Rashba interaction was included in the model the Landau levels were shown to cross at low fields introducing a beating pattern into the density of states oscillations. Similarities between data and the beat frequency extracted from the model yielded a Rashba parameter of $0.12 - 0.16\,\mathrm{eV\AA}$ for samples with carrier densities between $2.4 - 3.4 \times 10^{15}\,\mathrm{m}^{-2}$. These values are in very good agreement with values reported by different authors [36].

On gated samples the estimation of the strength of the Rashba interaction was not possible due to the absence of a beating pattern in the second differential of the Shubnikov-de Haas oscillations. It was shown that the suppression of beating oscillations can be attributed to large inhomogeneous broadening between the two spin states, which manifests as an asymmetric peak in the Fourier transform of the oscillations. The Fourier transform of resistivity data with obvious beating patterns yielded asymmetric peaks suggesting the presence of spin dependent broadening in these heterostructures.

The ability to create low resistance Ohmic contacts to a material is required for efficient injection of carriers into the active region of a structure and considerably minimises the effects of series resistance contributions to two or three terminal measurements. In this material system the processes used in order to make Ohmic contacts yield highly variable results with contacts of wildly different resistances being produced on the same device. Good Ohmic contact in these systems is thought to occur by contacting defects on the surface which pass current to the 2DEG, thus large area contacts contacting multiple defects are predicted to have the smallest contact resistances. In these high quality InSb quantum wells even large area contacts can make very poor contact to the 2DEG and are non-ideal as current injectors due to the greater amount of Joule-heating that occurs. However in a three-terminal measurement configuration this large contact resistance can be exploited to extract information about the energetic distribution of carriers underneath the contact.

Investigations of the low temperature I-V characteristics of a high resistance contact have been used as a form of electron spectroscopy. The magnetic field evolution of the energetic distribution of carriers was explored with a view to extracting material parameters such as the single-particle broadening and effective g-factor of structures. Scrutiny of the differential conductance data above 2 T revealed distinct peaks equally separated in energy. This energy separation was found to be proportional to the magnetic field strength consistent with the formation of Landau levels in a 2D system. The magnetic field evolution of peaks beyond a bias of $\sim -60\,\mathrm{mV}$ was shown to be well approximated by a Landau fan model using a band edge effective mass of $m^* = 0.014 \pm 0.001\, m_0$. At smaller bias values the peaks no longer show agreement with an appropriate value for the effective mass and are smeared out in bias. It was suggested that this smearing was due to the presence of a series resistance contribution to the measured voltage drop. Beyond a critical bias this scattering mechanism is removed and the measured voltage drop occurs solely across the contact. A suggested mechanism is from inter-subband scattering of electrons in the 2DEG. At sufficient bias the second subband becomes depopulated and the inter-subband scattering mechanism no longer occurs.

Through fitting of two Lorentzian peaks on a linear background to the differential conductance peak associated with the fundamental Landau level it was possible to extract values for the state broadening and effective g-factor of the material for that state. Modelling reveals two distinct broadening parameters for the high and low energy spin states consistent with the observation that there is spin dependent broadening present in these heterostructures. The difference in the broadening of the two states is considerable and is well described by a $\sqrt{B}$ dependence, in contrast to the constant broadening assumed in the density of states model in chapter 5. Estimates of the spin splitting from the separation between the centres of the two fitted peaks reveals an effective g-factor which varies from $g^* = 24 \pm 2$ at $B = 5.6\,\mathrm{T}$, to $g^* = 35 \pm 3$ at $B = 7.5\,\mathrm{T}$. This increase in the effective g-factor is likely due to the depopulation of the high energy spin states and the formation of a net spin population in the quantum well. The values extracted are consistent with studies of g-factor enhancement under the application of tilted magnetic fields [87].

7.2 Further work

The results obtained throughout the work described in this thesis would benefit from further investigation in certain areas to qualify and confirm many of the hypothesised causes behind these interesting observations.

i) The considerable degradation in the classical transport lifetime of these heterostructures once a gate dielectric has been deposited on the surface provides a profound drawback for further material development, where investigations into the effects of electrostatically gating high quality material should to be studied. The minimisation of surface traps, lowering the defect density at the dielectric-semiconductor interface while maintaining a low leakage dielectric is the topic of a further PhD thesis in itself, though improvements may be achieved by the growth of a thicker capping barrier to the quantum well (albeit with a corresponding reduction in gate modulation). If the mechanism limiting the classical lifetime is due to the remote scattering potential of the defect states in the dielectric a deeper quantum well may yield improved transport properties.

ii) All data presented in this thesis were for quantum well samples with a δ-dopant plane 25 nm above the quantum well. Increasing the size of the spacer layer between the dopant plane and the quantum well has already shown to improve the classical transport properties of these InSb heterostructures [24], though no data is presented for the effects on the quantum lifetime. Further studies could investigate the effects of spacer thickness on the quantum lifetime.

iii) The data presented in chapter 6 reveals inhomogeneous state broadening parameters which are magnetic field dependent, the modelling presented in chapter 5 only considers the effects of a constant broadening. Further modelling investigating the effects of enhanced field dependent broadening on the density of states oscillations would be interesting.

iv) As remarked in chapter 6, Hall bar geometries are not ideal for 3-terminal measurements due to the unavoidable series resistance contribution from the 2DEG to the contact. These measurements should be repeated on devices designed specifically for 3-terminal measurements with a remote voltage probe which lies over material that carries no current. A linear TLM pattern for example would be suited to such a measurement. The absence of the series resistance contribution will remove the bias smearing effects observed in the measurements presented in this thesis and allow for a further estimate of the effective mass of carriers in the quantum well.

Appendix A

The 2D density of states

The Schrödinger equation solutions to particle motion in an infinite 2D plane are take the form of the Bloch function

$$\psi(\boldsymbol{r}, \boldsymbol{k}) = u_{\boldsymbol{k}}(\boldsymbol{r}) \exp(i\boldsymbol{k}.\boldsymbol{r}) \tag{A.1}$$

where $\boldsymbol{r} = \begin{pmatrix} x \\ y \end{pmatrix}$, $\boldsymbol{k} = \begin{pmatrix} k_x \\ k_y \end{pmatrix}$, $u_{\boldsymbol{k}}(\boldsymbol{r})$ is the crystal periodic component of the Bloch function and $\exp(i\boldsymbol{k}.\boldsymbol{r}$ describes a plane wave. Imposing periodic boundary conditions such that the wave function has the same value at the boundary between two unit cells, discretises the components of $\boldsymbol{k}$ into

$$k_x = \frac{2\pi n_x}{L}, k_y = \frac{2\pi n_y}{L} \tag{A.2}$$

where n_x and n_y are integers and L is the lattice constant of the unit cell. The resultant k-vectors thus form a 2D grid of allowed states in k-space. Thus, each state in k-space is described by a square with sides $2\pi/L$ with a 2D “volume” given by

$$V = \frac{4\pi^2}{L^2} \tag{A.3}$$

An infinitesimal increment in k will thus enclose a number of states in a ring with an area $dA = 2\pi k dk$. The number of states in this ring, is simply the area of the ring

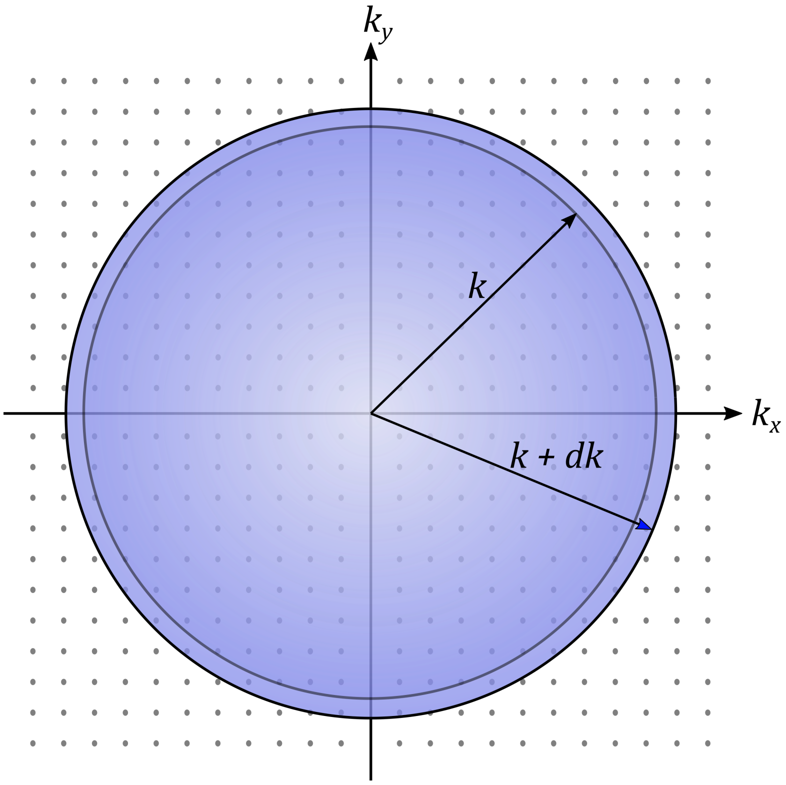

Figure A.1: A schematic representation of the array of allowed states in k-space. A given k-vector describes a circle enclosing a particular number of states.

divided by the area of each individual state, resulting with the k dependent expression for the density of states

$$g(k)\,dk = 2\frac{dA}{V} = \frac{L^2\,k}{\pi}\,dk \tag{A.4}$$

where a factor of two is included to account for the spin of particles.

The relationship between a particles energy and k-vector, in the parabolic approximation, is given by

$$k = \sqrt{\frac{2m^*E}{\hbar^2}} \tag{A.5}$$

differentiation with respect to energy gives an expression describing the change in k resulting from a small change in energy.

$$k\,dk = \frac{m^*}{\hbar^2}\,dE \tag{A.6}$$

Thus it is possible to express the density of states in a unit volume per unit energy

$$g(E)\,dE = \frac{m^*}{\pi\hbar^2}\,dE \tag{A.7}$$

The same sequence of operation may be performed using the non-parabolic energy dispersion relation 2.12

$$E(1+\lambda E) = \frac{\hbar^2 k^2}{2m^*} \tag{A.8}$$

where λ is the non-parabolicity factor. Differentiation of this yields

$$(1+2\lambda E)\,dE = \frac{\hbar^2 k}{m^*}\,dk \tag{A.9}$$

resulting in the modified non-parabolic density of states

$$g(E)\,dE = \frac{m^*}{\pi\hbar^2}\,(1+2\lambda E)\,dE \tag{A.10}$$

Bibliography

[1] John Bardeen. Semiconductor Research Leading to the Point Contact Transistor. In *Gt. Solid State Phys. 20th Century*, pages 234–260. WORLD SCIENTIFIC, New York, NY, apr 2003.

[2] Gordon E. Moore. Cramming more components onto integrated circuits, Reprinted from Electronics, volume 38, number 8, April 19, 1965, pp.114 ff. *IEEE Solid-State Circuits Newsl.*, 20(3):33–35, sep 2006.

[3] Martin Fuechsle, Jill A. Miwa, Suddhasatta Mahapatra, Hoon Ryu, Sunhee Lee, Oliver Warschkow, Lloyd C. L. Hollenberg, Gerhard Klimeck, and Michelle Y. Simmons. A single-atom transistor. *Nat. Nanotechnol.*, 7(4):242–246, apr 2012.

[4] Jesús A. del Alamo. Nanometre-scale electronics with IIIV compound semiconductors. *Nature*, 479(7373):317–323, nov 2011.

[5] Y. Q. Wu, M. Xu, P. D. Ye, Z. Cheng, J. Li, J.-S. Park, J. Hydrick, J. Bai, M. Carroll, J. G. Fiorenza, and A. Lochtefeld. Atomic-layer-deposited Al2O3/GaAs metal-oxide-semiconductor field-effect transistor on Si substrate using aspect ratio trapping technique. *Appl. Phys. Lett.*, 93(24):242106, dec 2008.

[6] T. D. Subash and T. Gnanasekaran. Indium antimonide based HEMT for RF applications. *J. Semicond.*, 35(11):113004, nov 2014.

[7] Xiaomeng Zhao, Yang Zhang, Min Guan, Lijie Cui, Baoqiang Wang, Zhanping Zhu, and Yiping Zeng. Effect of InSb/In 0.9 Al 0.1 Sb superlattice buffer layer on the structural and electronic properties of InSb films. *J. Cryst. Growth*, 470:1–7, jul 2017.

[8] S. Fujikawa, T. Taketsuru, D. Tsuji, T. Maeda, and H.I. Fujishiro. Improved electron transport properties of InSb quantum well structure using stepped buffer layer for strain reduction. *J. Cryst. Growth*, 425:64–69, sep 2015.

[9] M.Yu. Chernov, O.S. Komkov, D.D. Firsov, B.Ya. Meltser, A.N. Semenov, Ya.V. Terent'ev, P.N. Brunkov, A.A. Sitnikova, P.S. Kop'ev, S.V. Ivanov, and V.A. Solov'ev. InSb/InAs/InGa(Al)As/GaAs(0 0 1) metamorphic nanoheterostructures grown by MBE and emitting beyond 3 μm. *J. Cryst. Growth*, 477:97–99, nov 2017.

[10] Bo Wen Jia, Kian Hua Tan, Wan Khai Loke, Satrio Wicaksono, and Soon Fatt Yoon. Formation of periodic interfacial misfit dislocation array at the InSb/GaAs interface via surface anion exchange. *J. Appl. Phys.*, 120(3):035301, jul 2016.

[11] T. D. Mishima, M. Edirisooriya, N. Goel, and M. B. Santos. Dislocation filtering by AlxIn1xSbAlyIn1ySb interfaces for InSb-based devices grown on GaAs (001) substrates. *Appl. Phys. Lett.*, 88(19):191908, may 2006.

[12] Y. Shi, D. Gosselink, K. Gharavi, J. Baugh, and Z.R. R. Wasilewski. Optimization of metamorphic buffers for MBE growth of high quality AlInSb/InSb quantum structures: Suppression of hillock formation. *J. Cryst. Growth*, 477:7–11, nov 2017.

[13] Laura M. Roth and Benjamin Lax. g Factor of Electrons in Germanium. *Phys. Rev. Lett.*, 3(5):217–219, sep 1959.

[14] A A Konakov, A A Ezhevskii, A V Soukhorukov, D V Guseinov, S A Popkov, and V A Burdov. Lande factor of the conduction electrons in silicon: temperature dependence. *J. Phys. Conf. Ser.*, 324:012027, oct 2011.

[15] I. Vurgaftman, J. R. Meyer, and L. R. Ram-Mohan. Band parameters for IIIV compound semiconductors and their alloys. *J. Appl. Phys.*, 89(11):5815–5875, jun 2001.

[16] Madelung O, Rössler U, Schulz M, O Madelung, U Rössler, and M Schulz. *Landolt and BornsteinGroup III Condensed matter: Group IV Elements,(IVIV) and (IIIV) Compounds. Part bElectronic, Transport, Optical and Other Properties.* Springer, 2006.

[17] P. M. Tedrow and R. Meservey. Spin-Dependent Tunneling into Ferromagnetic Nickel. *Phys. Rev. Lett.*, 26(4):192–195, jan 1971.

[18] A. Fert, P. Grünberg, A. Barthélémy, F. Petroff, and W. Zinn. Layered magnetic structures: interlayer exchange coupling and giant magnetoresistance. *J. Magn. Magn. Mater.*, 140-144:1–8, feb 1995.

[19] David D. Awschalom and Michael E. Flatté. Challenges for semiconductor spintronics. *Nat. Phys.*, 3(3):153–159, mar 2007.

[20] J. Kikkawa and D. Awschalom. Resonant Spin Amplification in n-Type GaAs. *Phys. Rev. Lett.*, 80(19):4313–4316, 1998.

[21] B. Shojaei, P. J. J. O'Malley, J. Shabani, P. Roushan, B. D. Schultz, R. M. Lutchyn, C. Nayak, J. M. Martinis, and C. J. Palmstrøm. Demonstration of gate control of spin splitting in a high-mobility InAs/AlSb two-dimensional electron gas. *Phys. Rev. B*, 93(7):075302, feb 2016.

[22] Makoto Kohda, Shuji Nakamura, Yoshitaka Nishihara, Kensuke Kobayashi, Teruo Ono, Jun-ichiro Ohe, Yasuhiro Tokura, Taiki Mineno, and Junsaku Nitta. Spinorbit induced electronic spin separation in semiconductor nanostructures. *Nat. Commun.*, 3(1):1082, jan 2012.

[23] Fanming Qu, Jasper van Veen, Folkert K. de Vries, Arjan J. A. Beukman, Michael Wimmer, Wei Yi, Andrey A. Kiselev, Binh-Minh Nguyen, Marko Sokolich, Michael J. Manfra, Fabrizio Nichele, Charles M. Marcus, and Leo P. Kouwenhoven. Quantized Conductance and Large g -Factor Anisotropy in InSb Quantum Point Contacts. *Nano Lett.*, 16(12):7509–7513, dec 2016.

[24] J. M. S. Orr, A. M. Gilbertson, M Fearn, O. W. Croad, C. J. Storey, L. Buckle, M. T. Emeny, P. D. Buckle, and T. Ashley. Electronic transport in modulation-doped InSb quantum well heterostructures. *Phys. Rev. B*, 77(16):165334, apr 2008.

[25] NW Ashcroft and ND Mermin. *Solid State Physics.* Brooks Cole, 1976.

[26] Kittel. *Introduction to Solid State Physics.* John Wiley & Sons, Ltd, 8th editio edition, 1953.

[27] J. Singh. *Semiconductor Devices: An Introduction.* McGraw-Hill, 1 edition, 1993.

[28] Yoon-Suk Kim, Kerstin Hummer, and Georg Kresse. Accurate band structures and effective masses for InP, InAs, and InSb using hybrid functionals. *Phys. Rev. B*, 80(3):035203, jul 2009.

[29] Evan O. Kane. Band structure of indium antimonide. *J. Phys. Chem. Solids*, 1(4):249–261, jan 1957.

[30] R. Winkler. Rashba spin splitting in two-dimensional electron and hole systems. *Phys. Rev. B*, 62(7):4245–4248, aug 2000.

[31] Chris G. Van de Walle and J. Neugebauer. Universal alignment of hydrogen levels in semiconductors, insulators and solutions. *Nature*, 423(6940):626–628, jun 2003.

[32] A. T. Hatke, M. A. Zudov, L. N. Pfeiffer, and K. W. West. Temperature Dependence of Microwave Photoresistance in 2D Electron Systems. *Phys. Rev. Lett.*, 102(6):066804, feb 2009.

[33] N. Jiang, U. Lindemann, F. Giebeler, and G. Thummes. A 3He pulse tube cooler operating down to 1.3 K. *Cryogenics (Guildf).*, 44(11):809–816, nov 2004.

[34] D. G. Hayes, C. P. Allford, G. V. Smith, C. McIndo, L. A. Hanks, A. M. Gilbertson, L. F. Cohen, S. Zhang, E. M. Clarke, and P. D. Buckle. Electron transport lifetimes in InSb/Al1-xIn x Sb quantum well 2DEGs. *Semicond. Sci. Technol.*, 32(8):85002, jul 2017.

[35] Christopher J. McIndo, David G. Hayes, Andreas Papageorgiou, Laura A. Hanks, George V. Smith, Craig P. Allford, Shiyong Zhang, Edmund M. Clarke, and Philip D. Buckle. Determination of the transport lifetime limiting scattering rate in InSb/Al x In 1x Sb quantum wells using optical surface microscopy. *Phys. E Low-dimensional Syst. Nanostructures*, 91(April):169–172, jul 2017.

[36] A. M. Gilbertson, W. R. Branford, M. Fearn, L. Buckle, P. D. Buckle, T. Ashley, and L. F. Cohen. Zero-field spin splitting and spin-dependent broadening in high-mobility InSb/In1xAlxSb asymmetric quantum well heterostructures. *Phys. Rev. B*, 79(23):235333, jun 2009.

[37] A. M. Gilbertson, M. Fearn, A. Kormányos, D. E. Read, C. J. Lambert, M. T. Emeny, T. Ashley, S. A. Solin, and L. F. Cohen. Ballistic transport and boundary scattering in InSb/In1-xAl xSb mesoscopic devices. *Phys. Rev. B*, 83(7):1–10, 2011.

[38] J. Volger. Note on the Hall Potential Across an Inhomogeneous Conductor. *Phys. Rev.*, 79(6):1023–1024, sep 1950.

[39] P T Coleridge. Inter-subband scattering in a 2D electron gas. *Semicond. Sci. Technol.*, 5(9):961–966, sep 1990.

[40] R. Fletcher, E. Zaremba, M. D'Iorio, C. T. Foxon, and J. J. Harris. Persistent photoconductivity and two-band effects in GaAs/AlxGa1xAs heterojunctions. *Phys. Rev. B*, 41(15):10649–10666, may 1990.

[41] M Reed, W Kirk, and P Kobiela. Investigation of parallel conduction in GaAs/ AlxGa1-xAs modulation-doped structures in the quantum limit. *IEEE J. Quantum Electron.*, 22(9):1753–1759, sep 1986.

[42] T. Zhang, S. K. Clowes, M. Debnath, A. Bennett, C. Roberts, J. J. Harris, R. A. Stradling, L. F. Cohen, T. Lyford, and P. F. Fewster. High-mobility thin InSb films grown by molecular beam epitaxy. *Appl. Phys. Lett.*, 84(22):4463–4465, may 2004.

[43] Vijay K. Arora and Athar Naeem. Phonon-scattering-limited mobility in a quantum-well heterostructure. *Phys. Rev. B*, 31(6):3887–3892, mar 1985.

[44] J. H. (John H.) Davies. *The physics of low-dimensional semiconductors : an introduction.* Cambridge University Press, 1998.

[45] Ch. A. Lehner, T. Tschirky, T. Ihn, W. Dietsche, J. Keller, S. Fält, and W. Wegscheider. Limiting scattering processes in high-mobility InSb quantum wells grown on GaSb buffer systems. *Phys. Rev. Mater.*, 2(5):054601, may 2018.

[46] Kunio Tukioka. The Determination of the Deformation Potential Constant of the Conduction Band in InSb by the Electron Mobility in the Intrinsic Range. *Jpn. J. Appl. Phys.*, 30(Part 1, No. 2):212–217, feb 1991.

[47] O J Pooley, A M Gilbertson, P D Buckle, R S Hall, M T Emeny, M Fearn, M P Halsall, L F Cohen, and T Ashley. Quantum well mobility and the effect of gate dielectrics in remote doped InSb/Al x In 1 x Sb heterostructures. *Semicond. Sci. Technol.*, 25(12):125005, dec 2010.

[48] C J McIndo, D G Hayes, A Papageorgiou, L A Hanks, G V Smith, C P Allford, S Zhang, E M Clarke, and P D Buckle. Optical Microscopy as a probe of the rate limiting transport lifetime in InSb/Al 1-x In x Sb quantum wells. *J. Phys. Conf. Ser.*, 964:012005, feb 2018.

[49] D Yoshioka. *The quantum Hall effect.* Springer New York,, 2013.

[50] Th. Englert, D.C. Tsui, A.C. Gossard, and Ch. Uihlein. g-Factor enhancement in the 2D electron gas in GaAs/AlGaAs heterojunctions. *Surf. Sci.*, 113(1-3):295–300, jan 1982.

[51] J. J. Harris, J. M. Roberts, S. N. Holmes, and K. Woodbridge. Observation of oscillatory linewidth behavior in the magnetoluminescence of a modulation-doped InxGa1xAs quantum well. *Phys. Rev. B*, 53(8):4886–4890, feb 1996.

[52] Richard E Prange and Steven M Girvin. *The Quantum Hall effect, Graduate texts in contemporary physics.* Springer New York,, 2 edition, 1987.

[53] H. van Houten, J. G. Williamson, M. E. I. Broekaart, C. T. Foxon, and J. J. Harris. Magnetoresistance in a GaAs-AlxGa1xAs heterostructure with double subband occupancy. *Phys. Rev. B*, 37(5):2756–2758, feb 1988.

[54] A. M. Gilbertson, M Fearn, J. H. Jefferson, B. N. Murdin, P. D. Buckle, and L. F. Cohen. Zero-field spin splitting and spin lifetime in nInSb/In1xAlxSb asymmetric quantum well heterostructures. *Phys. Rev. B*, 77(16):165335, apr 2008.

[55] G. A. Khodaparast, R. E. Doezema, S. J. Chung, K. J. Goldammer, and M. B. Santos. Spectroscopy of Rashba spin splitting in InSb quantum wells. *Phys. Rev. B*, 70(15):155322, oct 2004.

[56] K. v. Klitzing, G. Dorda, and M. Pepper. New Method for High-Accuracy Determination of the Fine-Structure Constant Based on Quantized Hall Resistance. *Phys. Rev. Lett.*, 45(6):494–497, aug 1980.

[57] Tsuneya Ando and Yasutada Uemura. Theory of Oscillatory g Factor in an MOS Inversion Layer under Strong Magnetic Fields. *J. Phys. Soc. Japan*, 37(4):1044–1052, oct 1974.

[58] R. E. Prange. Quantized Hall resistance and the measurement of the fine-structure constant. *Phys. Rev. B*, 23(9):4802–4805, may 1981.

[59] R. B. Laughlin. Quantized Hall conductivity in two dimensions. *Phys. Rev. B*, 23(10):5632–5633, may 1981.

[60] M. J. Manfra, S. H. Simon, K. W. Baldwin, A. M. Sergent, K. W. West, R. J. Molnar, and J. Caissie. Quantum and transport lifetimes in a tunable low-density AlGaNGaN two-dimensional electron gas. *Appl. Phys. Lett.*, 85(22):5278–5280, nov 2004.

[61] PT T. Coleridge, R. Stoner, and R. Fletcher. Low-field transport coefficients in GaAs/Ga 1 x Al x As heterostructures. *Phys. Rev. B*, 39(2):1120–1124, jan 1989.

[62] P. T. Coleridge, P Zawadzki, and A. S. Sachrajda. Peak values of resistivity in high-mobility quantum-Hall-effect samples. *Phys. Rev. B*, 49(15):10798–10801, apr 1994.

[63] S. Q. Murphy, J. P. Eisenstein, L. N. Pfeiffer, and K. W. West. Lifetime of two-dimensional electrons measured by tunneling spectroscopy. *Phys. Rev. B*, 52(20):14825–14828, nov 1995.

[64] P. T. Coleridge. Small-angle scattering in two-dimensional electron gases. *Phys. Rev. B*, 44(8):3793–3801, aug 1991.

[65] Gabriele F. Giuliani and John J. Quinn. Lifetime of a quasiparticle in a two-dimensional electron gas. *Phys. Rev. B*, 26(8):4421–4428, oct 1982.

[66] J. Nuebler, V. Umansky, R. Morf, M. Heiblum, K. von Klitzing, and J. Smet. Density dependence of the ν=5/2 energy gap: Experiment and theory. *Phys. Rev. B*, 81(3):035316, jan 2010.

[67] Q. Qian, J. Nakamura, S. Fallahi, G. C. Gardner, J. D. Watson, S. Lüscher, J. A. Folk, G. A. Csáthy, and M. J. Manfra. Quantum lifetime in ultrahigh quality GaAs quantum wells: Relationship to Δ5/2 and impact of density fluctuations. *Phys. Rev. B*, 96(3):035309, jul 2017.

[68] N. Goel, P. Majhi, C. O. Chui, W. Tsai, D. Choi, and J. S. Harris. InGaAs metal-oxide-semiconductor capacitors with HfO2 gate dielectric grown by atomic-layer deposition. *Appl. Phys. Lett.*, 89(16):163517, oct 2006.

[69] R. Suzuki, N. Taoka, M. Yokoyama, S. Lee, S. H. Kim, T. Hoshii, T. Yasuda, W. Jevasuwan, T. Maeda, O. Ichikawa, N. Fukuhara, M. Hata, M. Takenaka, and S. Takagi. 1-nm-capacitance-equivalent-thickness HfO 2 /Al 2 O 3 /InGaAs metal-oxide-semiconductor structure with low interface trap density and low gate leakage current density. *Appl. Phys. Lett.*, 100(13):132906, mar 2012.

[70] Tsuneya Ando, Alan B. Fowler, and Frank Stern. Electronic properties of two-dimensional systems. *Rev. Mod. Phys.*, 54(2):437–672, apr 1982.

[71] R.P. Gammag and C. Villagonzalo. The interplay of Landau level broadening and temperature on two-dimensional electron systems. *Solid State Commun.*, 146(11-12):487–490, jun 2008.

[72] V. Mosser, D. Weiss, K.v. Klitzing, K. Ploog, and G. Weimann. Density of states of GaAs-AlGaAs-heterostructures deduced from temperature dependent magnetocapacitance measurements. *Solid State Commun.*, 58(1):5–7, apr 1986.

[73] E. Gornik, R. Lassnig, G. Strasser, H. L. Störmer, A. C. Gossard, and W. Wiegmann. Specific Heat of Two-Dimensional Electrons in GaAs-GaAlAs Multilayers. *Phys. Rev. Lett.*, 54(16):1820–1823, apr 1985.

[74] J. K. Wang, J. H. Campbell, D. C. Tsui, and A. Y. Cho. Heat capacity of the two-dimensional electron gas in GaAs/AlxGa1xAs multiple-quantum-well structures. *Phys. Rev. B*, 38(9):6174–6184, sep 1988.

[75] I. M. Templeton. A highsensitivity torsional magnetometer for twodimensional electron systems. *J. Appl. Phys.*, 64(7):3570–3573, oct 1988.

[76] T.T.J.M. Berendschot, H.A.J.M. Reinen, and H.J.A. Bluyssen. Density of states of a two dimensional electron gas in a high magnetic field studied with photoluminescence. *Solid State Commun.*, 63(10):873–876, sep 1987.

[77] T. P. Smith, B. B. Goldberg, P. J. Stiles, and M. Heiblum. Direct measurement of the density of states of a two-dimensional electron gas. *Phys. Rev. B*, 32(4):2696–2699, aug 1985.

[78] S. Takaoka, K. Oto, H. Kurimoto, K. Murase, K. Gamo, and S. Nishi. Magnetocapacitance and the edge state of a two-dimensional electron system in the quantum Hall regime. *Phys. Rev. Lett.*, 72(19):3080–3083, may 1994.

[79] J. P. Eisenstein, H. L. Stormer, V. Narayanamurti, A. Y. Cho, A. C. Gossard, and C. W. Tu. Density of States and de Haasvan Alphen Effect in Two-Dimensional Electron Systems. *Phys. Rev. Lett.*, 55(8):875–878, aug 1985.

[80] M.S. Skolnick, K.J. Nash, S.J. Bass, P.E. Simmonds, and M.J. Kane. Photoluminescence study of the density-of-states between Landau levels in the quantum hall effect system. *Solid State Commun.*, 67(6):637–641, aug 1988.

[81] Hou-zhi Zheng, Aimin Song, Fu-hua Yang, and Yue-xia Li. Density of states of the two-dimensional electron gas studied by magnetocapacitances of biased double-barrier structures. *Phys. Rev. B*, 49(3):1802–1808, jan 1994.

[82] R.C. Ashoori and R.H. Silsbee. The Landau level density of states as a function of Fermi energy in the two dimensional electron gas. *Solid State Commun.*, 81(10):821–825, mar 1992.

[83] S. Askenazy, P.R. Wallace, R.A. Stradling, J. Galibert, and P. Perrier. Simple calculation of the Landau levels of narrow-gap semiconductors in the Kane model. *Phys. Lett. A*, 106(4):184–186, dec 1984.

[84] L. Onsager. Interpretation of the de Haas-van Alphen effect. *London, Edinburgh, Dublin Philos. Mag. J. Sci.*, 43(344):1006–1008, sep 1952.

[85] Loren Pfeiffer, K. W. West, H. L. Stormer, and K. W. Baldwin. Electron mobilities exceeding 10 7 cm 2 /V s in modulationdoped GaAs. *Appl. Phys. Lett.*, 55(18):1888–1890, oct 1989.

[86] J. Luo, H. Munekata, F. F. Fang, and P. J. Stiles. Effects of inversion asymmetry on electron energy band structures in GaSb/InAs/GaSb quantum wells. *Phys. Rev. B*, 41(11):7685–7693, apr 1990.

[87] B. Nedniyom, R. J. Nicholas, M. T. Emeny, L. Buckle, A. M. Gilbertson, P. D. Buckle, and T. Ashley. Giant enhanced g-factors in an InSb two-dimensional gas. *Phys. Rev. B*, 80(12):125328, sep 2009.

[88] T. P. Smith and F. F. Fang. G factor of electrons in an InAs quantum well. *Phys. Rev. B*, 35(14):7729–7731, 1987.

[89] M. J. Yang, R. J. Wagner, B. V. Shanabrook, J. R. Waterman, and W. J. Moore. Spin-resolved cyclotron resonance in InAs quantum wells: A study of the energy-dependent g factor. *Phys. Rev. B*, 47(11):6807–6810, mar 1993.

[90] V. Sa-yakanit, N. Choosiri, and Henry R. Glyde. Density of states between Landau levels in a two-dimensional electron gas. *Phys. Rev. B*, 38(2):1340–1343, jul 1988.

[91] M. E. Raikh and T. V. Shahbazyan. High Landau levels in a smooth random potential for two-dimensional electrons. *Phys. Rev. B*, 47(3):1522–1531, jan 1993.

[92] G Dresselhaus. Spin-orbit coupling effects in zinc blende structures. *Phys. Rev.*, 1955.

[93] Roland Winkler. *Spin–Orbit Coupling Effects in Two-Dimensional Electron and Hole Systems*, volume 191 of *Springer Tracts in Modern Physics*. Springer Berlin Heidelberg, Berlin, Heidelberg, 2003.

[94] G. Lommer, F. Malcher, and U. Rossler. Spin splitting in semiconductor heterostructures for B0. *Phys. Rev. Lett.*, 60(8):728–731, feb 1988.

[95] Martin Gmitra and Jaroslav Fabian. First-principles studies of orbital and spin-orbit properties of GaAs, GaSb, InAs, and InSb zinc-blende and wurtzite semiconductors. *Phys. Rev. B*, 94(16):165202, oct 2016.

[96] Tiago Campos, Paulo E. Faria Junior, Martin Gmitra, Guilherme M. Sipahi, and Jaroslav Fabian. Spin-orbit coupling effects in zinc-blende InSb and wurtzite InAs nanowires: Realistic calculations with multiband k · p method. *Phys. Rev. B*, 97(24):245402, jun 2018.

[97] M. Cardona, N. E. Christensen, and G. Fasol. Relativistic band structure and spin-orbit splitting of zinc-blende-type semiconductors. *Phys. Rev. B*, 38(3):1806–1827, jul 1988.

[98] R. Eppenga and M. F. H. Schuurmans. Effect of bulk inversion asymmetry on [001], [110], and [111] GaAs/AlAs quantum wells. *Phys. Rev. B*, 37(18):10923–10926, jun 1988.

[99] P. Pfeffer and W. Zawadzki. Spin splitting of conduction subbands in III-V heterostructures due to inversion asymmetry. *Phys. Rev. B*, 59(8):R5312–R5315, feb 1999.

[100] P. Pfeffer and W. Zawadzki. Bychkov-Rashba spin splitting and its dependence on magnetic field in InSb/In0.91Al0.09Sb asymmetric quantum wells. *Phys. Rev. B*, 68(3):1–7, 2003.

[101] Wei Yi, Andrey a. Kiselev, Jacob Thorp, Ramsey Noah, Binh-Minh Nguyen, Steven Bui, Rajesh D. Rajavel, Tahir Hussain, Mark F. Gyure, Philip Kratz, Qi Qian, Michael J. Manfra, Vlad S. Pribiag, Leo P. Kouwenhoven, Charles M. Marcus, and Marko Sokolich. Gate-tunable high mobility remote-doped InSb/In 1x Al x Sb quantum well heterostructures. *Appl. Phys. Lett.*, 106(14):142103, apr 2015.

[102] T. Masuda, K. Sekine, K. Nagase, K. S. Wickramasinghe, T. D. Mishima, M. B. Santos, and Y. Hirayama. Transport characteristics of InSb trench-type in-plane gate quantum point contact. *Appl. Phys. Lett.*, 112(19):192103, may 2018.

[103] VI Dyakonov, MI and Perel. Spin relaxation of conduction electrons in noncentrosymmetric semiconductors. *Sov. Phys. Solid State, Ussr*, 13(12):3023–3026, 1972.

[104] G. Engels, J. Lange, Th. Schäpers, and H. Lüth. Experimental and theoretical approach to spin splitting in modulation-doped InxGa1xAs/InP quantum wells for B0. *Phys. Rev. B*, 55(4):R1958–R1961, jan 1997.

[105] Hiroshi Akera, Hidekatsu Suzuura, and Yoshiyuki Egami. Gate-voltage-induced switching of the Rashba spin-orbit interaction in a composition-adjusted quantum well. *Phys. Rev. B*, 95(4):045301, jan 2017.

[106] J. B. Miller, D. M. Zumbühl, C. M. Marcus, Y. B. Lyanda-Geller, D. Goldhaber-Gordon, K. Campman, and A. C. Gossard. Gate-Controlled Spin-Orbit Quantum Interference Effects in Lateral Transport. *Phys. Rev. Lett.*, 90(7):076807, feb 2003.

[107] Dirk Grundler. Large Rashba Splitting in InAs Quantum Wells due to Electron Wave Function Penetration into the Barrier Layers. *Phys. Rev. Lett.*, 84(26):6074–6077, jun 2000.

[108] Supriyo Datta and Biswajit Das. Electronic analog of the electro-optic modulator. *Appl. Phys. Lett.*, 56(7):665, feb 1990.

[109] S Brosig, K Ensslin, R. J. Warburton, C Nguyen, B Brar, M. Thomas, and H. Kroemer. Zero-field spin splitting in InAs-AlSb quantum wells revisited. *Phys. Rev. B*, 60(20):R13989–R13992, nov 1999.

[110] Takaaki Koga, Junsaku Nitta, Tatsushi Akazaki, and Hideaki Takayanagi. Rashba Spin-Orbit Coupling Probed by the Weak Antilocalization Analysis in InAlAs/InGaAs/InAlAs Quantum Wells as a Function of Quantum Well Asymmetry. *Phys. Rev. Lett.*, 89(4):046801, jul 2002.

[111] Junsaku Nitta, Tatsushi Akazaki, Hideaki Takayanagi, and Takatomo Enoki. Gate Control of Spin-Orbit Interaction in an Inverted In0.53Ga0.47As/In0.52Al0.48As Heterostructure. *Phys. Rev. Lett.*, 78(7):1335–1338, feb 1997.

[112] J. Luo, H. Munekata, F. F. Fang, and P. J. Stiles. Observation of the zero-field spin splitting of the ground electron subband in gasb-inas-gasb quantum wells. *Phys. Rev. B*, 38(14):10142–10145, 1988.

[113] K. P. Kalinin, S. S. Krishtopenko, K. V. Maremyanin, K. E. Spirin, V. I. Gavrilenko, A. A. Biryukov, N. V. Baidus, and B. N. Zvonkov. Rashba spin splitting and cyclotron resonance in strained InGaAs/InP heterostructures with a two-dimensional electron gas. *Semiconductors*, 47(11):1485–1491, nov 2013.

[114] V. Ya. Aleshkin, V. I. Gavrilenko, A. V. Ikonnikov, S. S. Krishtopenko, Yu. G. Sadofyev, and K. E. Spirin. Exchange enhancement of the g factor in InAs/AlSb heterostructures. *Semiconductors*, 42(7):828–833, jul 2008.

[115] S. S. Krishtopenko, K. P. Kalinin, V. I. Gavrilenko, Yu. G. Sadofyev, and M. Goiran. Rashba spin splitting and exchange enhancement of the g factor in InAs/AlSb heterostructures with a two-dimensional electron gas. *Semiconductors*, 46(9):1163–1170, sep 2012.

[116] Can-Ming Hu, Junsaku Nitta, Tatsushi Akazaki, Hideaki Takayanagi, Jiro Osaka, P. Pfeffer, and W. Zawadzki. Zero-field spin splitting in an inverted In0.53Ga0.47A s/I n0.52Al0.48As heterostructure: Band nonparabolicity influence and the subband dependence. *Phys. Rev. B*, 60(11):7736–7739, sep 1999.

[117] J Kunc, B. A. Piot, D. K. Maude, M Potemski, R. Grill, C. Betthausen, D. Weiss, V. Kolkovsky, G. Karczewski, and T. Wojtowicz. Magnetoresistance quantum oscillations in a magnetic two-dimensional electron gas. *Phys. Rev. B*, 92(8):085304, aug 2015.

[118] X. Z. Liu, Y. G. Xu, G. Yu, L. M. Wei, T. Lin, S. L. Guo, J. H. Chu, W. Z. Zhou, Y. G. Zhang, and David J. Lockwood. The effective g-factor in In 0.53 Ga 0.47 As/In 0.52 Al 0.48 As quantum well investigated by magnetotransport measurement. *J. Appl. Phys.*, 113(3):033704, jan 2013.

[119] B. Das, D. C. Miller, S. Datta, R. Reifenberger, W. P. Hong, P. K. Bhattacharya, J. Singh, and M. Jaffe. Evidence for spin splitting in InxGa1-xAs/In0.52Al0.48As heterostructures as B0. *Phys. Rev. B*, 39(2):1411–1414, 1989.

[120] T. H. Sander, S. N. Holmes, J. J. Harris, D. K. Maude, and J. C. Portal. Determination of the phase of magneto-intersubband scattering oscillations in heterojunctions and quantum wells. *Phys. Rev. B*, 58(20):13856–13862, nov 1998.

[121] H.L. Störmer, A.C. Gossard, and W. Wiegmann. Observation of intersubband scattering in a 2-dimensional electron system. *Solid State Commun.*, 41(10):707–709, mar 1982.

[122] M. E. Raikh and T. V. Shahbazyan. Magnetointersubband oscillations of conductivity in a two-dimensional electronic system. *Phys. Rev. B*, 49(8):5531–5540, feb 1994.

[123] D. R. Leadley, R. Fletcher, R. J. Nicholas, F. Tao, C. T. Foxon, and J. J. Harris. Intersubband resonant scattering in GaAs-Ga1xAlxAs heterojunctions. *Phys. Rev. B*, 46(19):12439–12447, nov 1992.

[124] Th. Schäpers, J Knobbe, and V. A. Guzenko. Effect of Rashba spin-orbit coupling on magnetotransport in InGaAsInP quantum wire structures. *Phys. Rev. B*, 69(23):235323, jun 2004.

[125] J. Tersoff. Schottky barriers and semiconductor band structures. *Phys. Rev. B*, 32(10):6968–6971, nov 1985.

[126] S. Datta, T. Ashley, J. Brask, L. Buckle, M. Doczy, M. Emeny, D. Hayes, K. Hilton, R. Jefferies, T. Martin, T.J. Phillips, D. Wallis, P. Wilding, and R. Chau. 85nm gate length enhancement and depletion mode InSb quantum well transistors for ultra high speed and very low power digital logic applications. In *IEEE Int. Devices Meet. 2005. IEDM Tech. Dig.*, pages 763–766. IEEE, 2005.

[127] T. Ashley, A.R. Barnes, L. Buckle, S. Datta, A.B. Dean, M.T. Emeny, M. Fearn, D.G. Haves, K.P. HiIton, R. Jefferies, T. Martin, K.J. Nash, T.J. Phillips, W.H.A. Tang, P.J. Wilding, and R. Chau. Novel insb-based quantum well transistors for ultra-high speed, low power logic applications. In *Proceedings. 7th Int. Conf. Solid-State Integr. Circuits Technol. 2004.*, volume 3, pages 2253–2256. IEEE, 2004.

[128] T. Ashley, L. Buckle, S. Datta, M.T. Emeny, D.G. Hayes, K.P. Hilton, R. Jefferies, T. Martin, T.J. Phillips, D.J. Wallis, P.J. Wilding, and R. Chau. Heterogeneous InSb quantum well transistors on silicon for ultra-high speed, low power logic applications. *Electron. Lett.*, 43(14):777, 2007.

[129] E. Merzbacher. *Quantum Mechanics.* Wiley, 1998.

[130] P. Chiaradia, M. Fanfoni, P. Nataletti, P. De Padova, L. J. Brillson, M. L. Slade, R. E. Viturro, D. Kilday, and G. Margaritondo. Fermi-level pinning and intrinsic surface states in cleaved GaP. *Phys. Rev. B*, 39(8):5128–5131, mar 1989.

[131] V. Mourik, K. Zuo, S. M. Frolov, S. R. Plissard, E. P. A. M. Bakkers, and L. P. Kouwenhoven. Signatures of Majorana Fermions in Hybrid Superconductor-Semiconductor Nanowire Devices. *Science (80-.).*, 336(6084):1003–1007, may 2012.

[132] Ryuichi Masutomi, Masayuki Hio, Toshimitsu Mochizuki, and Tohru Okamoto. Quantum Hall effect at cleaved InSb surfaces and low-temperature annealing effect. *Appl. Phys. Lett.*, 90(20):202104, may 2007.

[133] M. Morgenstern, J. Klijn, Chr. Meyer, M. Getzlaff, R. Adelung, R. A. Römer, K. Rossnagel, L. Kipp, M. Skibowski, and R. Wiesendanger. Direct Comparison between Potential Landscape and Local Density of States in a Disordered Two-Dimensional Electron System. *Phys. Rev. Lett.*, 89(13):136806, sep 2002.

[134] M. Morgenstern, J. Klijn, Chr. Meyer, and R. Wiesendanger. Real-Space Observation of Drift States in a Two-Dimensional Electron System at High Magnetic Fields. *Phys. Rev. Lett.*, 90(5):056804, feb 2003.

[135] Shuma Abe, Takeshi Inaoka, and Masayuki Hasegawa. Evolution of electron states at a narrow-gap semiconductor surface in an accumulation-layer formation process. *Phys. Rev. B*, 66(20):205309, nov 2002.

[136] R. Dombrowski, Chr. Steinebach, Chr. Wittneven, M. Morgenstern, and R. Wiesendanger. Tip-induced band bending by scanning tunneling spectroscopy of the states of the tip-induced quantum dot on InAs(110). *Phys. Rev. B*, 59(12):8043–8048, mar 1999.

[137] S. Ilani, J. Martin, E. Teitelbaum, J. H. Smet, D. Mahalu, V. Umansky, and A. Yacoby. The microscopic nature of localization in the quantum Hall effect. *Nature*, 427(6972):328–332, jan 2004.

[138] S. H. Tessmer, P. I. Glicofridis, R. C. Ashoori, L. S. Levitov, and M. R. Melloch. Subsurface charge accumulation imaging of a quantum Hall liquid. *Nature*, 392(6671):51–54, mar 1998.

[139] K. Hashimoto, C. Sohrmann, J. Wiebe, T. Inaoka, F. Meier, Y. Hirayama, R. A. Römer, R. Wiesendanger, and M. Morgenstern. Quantum Hall Transition in Real Space: From Localized to Extended States. *Phys. Rev. Lett.*, 101(25):256802, dec 2008.

[140] P. C. Main, A. S. G. Thornton, R. J. A. Hill, S. T. Stoddart, T. Ihn, L. Eaves, K. A. Benedict, and M. Henini. Landau-Level Spectroscopy of a Two-Dimensional Electron System by Tunneling through a Quantum Dot. *Phys. Rev. Lett.*, 84(4):729–732, jan 2000.

[141] R. C. Ashoori, J. A. Lebens, N. P. Bigelow, and R. H. Silsbee. Equilibrium tunneling from the two-dimensional electron gas in GaAs: Evidence for a magnetic-field-induced energy gap. *Phys. Rev. Lett.*, 64(6):681–684, feb 1990.

[142] K. M. Brown, N. Turner, J. T. Nicholls, E. H. Linfield, M. Pepper, D. A. Ritchie, and G. A. C. Jones. Tunneling between two-dimensional electron gases in a strong magnetic field. *Phys. Rev. B*, 50(20):15465–15468, nov 1994.

[143] J. P. Eisenstein, L. N. Pfeiffer, and K. W. West. Evidence for an Interlayer Exciton in Tunneling between Two-Dimensional Electron Systems. *Phys. Rev. Lett.*, 74(8):1419–1422, feb 1995.

[144] K.M. Brown, J.T. Nicholls, B. Tieke, S.A.J. Wiegers, P.J.M. van Bentum, E.H. Linfield, M. Pepper, D.A. Ritchie, and G.A.C. Jones. Tunnelling between two-dimensional electron gases up to 25 T. *Phys. B Condens. Matter*, 211(1-4):430–432, may 1995.

[145] N. Turner, J. T. Nicholls, E. H. Linfield, K. M. Brown, G. A. C. Jones, and D. A. Ritchie. Tunneling between parallel two-dimensional electron gases. *Phys. Rev. B*, 54(15):10614–10624, oct 1996.

[146] M Russ, A Lorke, D Reuter, and P Schafmeister. Self-assembled quantum dots as probes for Landau-level spectroscopy. *Phys. E Low-dimensional Syst. Nanostructures*, 22(1-3):506–509, apr 2004.

[147] Y. Yoon, L. Tiemann, S. Schmult, W. Dietsche, K. von Klitzing, and W. Wegscheider. Interlayer Tunneling in Counterflow Experiments on the Excitonic Condensate in Quantum Hall Bilayers. *Phys. Rev. Lett.*, 104(11):116802, mar 2010.

[148] J. P. Pekola, K. P. Hirvi, J. P. Kauppinen, and M. A. Paalanen. Thermometry by arrays of tunnel junctions. *Phys. Rev. Lett.*, 73(21):2903–2906, nov 1994.

[149] M. T. Deng, C. L. Yu, G. Y. Huang, M. Larsson, P. Caroff, and H. Q. Xu. Anomalous Zero-Bias Conductance Peak in a NbInSb NanowireNb Hybrid Device. *Nano Lett.*, 12(12):6414–6419, dec 2012.

[150] H. O. H. Churchill, V. Fatemi, K. Grove-Rasmussen, M. T. Deng, P. Caroff, H. Q. Xu, and C. M. Marcus. Superconductor-nanowire devices from tunneling to the multichannel regime: Zero-bias oscillations and magnetoconductance crossover. *Phys. Rev. B*, 87(24):241401, jun 2013.

[151] Falko Pientka, Graham Kells, Alessandro Romito, Piet W. Brouwer, and Felix von Oppen. Enhanced Zero-Bias Majorana Peak in the Differential Tunneling Conductance of Disordered Multisubband Quantum-Wire/Superconductor Junctions. *Phys. Rev. Lett.*, 109(22):227006, nov 2012.

[152] Anindya Das, Yuval Ronen, Yonatan Most, Yuval Oreg, Moty Heiblum, and Hadas Shtrikman. Zero-bias peaks and splitting in an AlInAs nanowire topological superconductor as a signature of Majorana fermions. *Nat. Phys.*, 8(12):887–895, dec 2012.

[153] Sébastien R. Plissard, Dorris R. Slapak, Marcel A. Verheijen, Moïra Hocevar, George W. G. Immink, Ilse van Weperen, Stevan Nadj-Perge, Sergey M. Frolov, Leo P. Kouwenhoven, and Erik P. A. M. Bakkers. From InSb Nanowires to Nanocubes: Looking for the Sweet Spot. *Nano Lett.*, 12(4):1794–1798, apr 2012.

[154] A Usher, M Zhu, AJ Matthews, A Potts, M Elliott, W.G Herrenden-Harker, D.A Ritchie, and M.Y Simmons. Equilibrium magnetization measurements of two-dimensional electron systems. *Phys. E Low-dimensional Syst. Nanostructures*, 22(1-3):741–744, apr 2004.

[155] M. A. Wilde, M. P. Schwarz, Ch. Heyn, D. Heitmann, D. Grundler, D. Reuter, and A. D. Wieck. Experimental evidence of the ideal de Haasvan Alphen effect in a two-dimensional system. *Phys. Rev. B*, 73(12):125325, mar 2006.

[156] R A Beeston, A H Wright, S Maddox, H L Gomez, L Dunne, S P Driver, A Robotham, C J R Clark, K Vinsen, T T Takeuchi, G Popping, N Bourne, M N Bremer, S Phillipps, A J Moffett, M Baes, J Bland-Hawthorn, S Brough, P De Vis, S A Eales, B W Holwerda, J Loveday, J Liske, M W L Smith, D J B Smith, E Valiante, C Vlahakis, and L Wang. GAMA/H-ATLAS: the local dust mass function and cosmic density as a function of galaxy type a benchmark for models of galaxy evolution. *Mon. Not. R. Astron. Soc.*, 479(1):1077–1099, 2018.

[157] Masato Shirasaki, Masahiro Takada, Hironao Miyatake, Ryuichi Takahashi, Takashi Hamana, Takahiro Nishimichi, and Ryoma Murata. Robust covariance estimation of galaxygalaxy weak lensing: validation and limitation of jackknife covariance. *Mon. Not. R. Astron. Soc.*, 470(3):3476–3496, sep 2017.

[158] A Potts, R Shepherd, W G Herrenden-Harker, M Elliott, C L Jones, A Usher, G A C Jones, D A Ritchie, E H Linfield, and M Grimshaw. Magnetization studies of Landau level broadening in two-dimensional electron systems. *J. Phys. Condens. Matter*, 8(28):5189–5207, jul 1996.

[159] A Usher and M Elliott. Magnetometry of low-dimensional electron and hole systems. *J. Phys. Condens. Matter*, 21(10):103202, mar 2009.

[160] M. A. Wilde, B. Rupprecht, F. Herzog, A. Ibrahim, and D. Grundler. Spin-orbit interaction in the magnetization of two-dimensional electron systems. *Phys. status solidi*, 251(9):1710–1724, sep 2014.